Cryogenic electron tomography studies on cellular autophagy membranes

Inaugural dissertation

for the attainment of the title of doctor
in the Faculty of Mathematics and Natural Sciences
at the Heinrich Heine University Düsseldorf

presented by

Claire Ortmann de Percin Northumberland
from Aachen, Germany

Düsseldorf, May 2024

from the institute for Biology
at the Heinrich Heine University Düsseldorf

Published with permission of the
Faculty of Mathematics and Natural Sciences at
Heinrich Heine University Düsseldorf

Supervisor: Prof. Dr. Carsten Sachse
Co-supervisor: Prof. Dr. Gunnar Schröder

Date of the oral examination: 02.07.2024

Eidesstattliche Erklärung (PO §5 section 1b; §6 section 5):

Ich versichere an Eides Statt, dass die Dissertation von mir selbständig und ohne unzulässige fremde Hilfe unter Beachtung der „Grundsätze zur Sicherung guter wissenschaftlicher Praxis an der Heinrich-Heine-Universität Düsseldorf“ erstellt worden ist.

Acknowledgements

First, I would like to thank my supervisor Prof. Dr. Carsten Sachse for his continuous support throughout my PhD, for giving me the opportunity to gain so much hands-on experience on the different microscopes and creating such a collaborative working environment. I count myself extremely fortunate to have benefitted from these learning opportunities, and your generosity of sending me to conferences and courses whenever possible, even during the pandemic.

I would also like to thank Prof. Dr. Gunnar Schröder for serving as my mentor as well as Prof. Dr. Claudine Kraft, Dr. Mariya Licheva and Dr. Akif Ciftci for their help with yeast handling, protocols, strains, plasmids, and fruitful discussions. Most importantly I am grateful to you for showing me that open-minded and friendly collaboration is possible in today's scientific community.

Thank you to Dr. Sabrina Berkamp for training me on this microscopic workflow and advising me in its optimisation for my research question. Your counsel in critical moments of my project has been invaluable. I would also like to thank Dr. Daniel Mann, for continuous moral, scientific, and computational support. You were always happy to help and collaborate whenever possible.

Thank you to the facility staff, Dr. Thomas Heidler, Pia Sundermeyer, Dr. Saba Shahzad, and Dr. Julio Ortiz. Aside from training me and maintaining the microscopes, they have lent an ear when needed and offered support in this challenging microscopy workflow.

Thank you to everyone in our institute, especially Dr. Benedikt Junglas, Ilona Ritter, Dr. Siavash Mostafavi, Lisa Jungbluth, Kevin Boga, David Kartte, and Philipp Schönnenbeck who have contributed to this work in one form or another. No matter whether that was by providing reagents, maintaining equipment, training, advice, moral support, or protocols.

Thank you to Dr. Alastair T. Gardiner and Dr. Wei-Chun Kao who have fundamentally shaped the way I see Science. They taught me the balance of caution, appreciation for detail and courage in scientific research.

Finally, I would like to thank my family, especially my parents and my brothers for lifelong encouragement and support. Danke für die hilfreichen Gespräche und alle Möglichkeiten die mir durch euch offenstehen. Merci pour votre soutien, votre amour et toutes les chances qui me sont ouverte grâce à vous.

Summary

During autophagy, a double membrane enwraps cellular cargo to deliver it to the lysosome. The aim of this PhD work was to characterise autophagic membranes, also called phagophores, during their elongation and to investigate how two autophagy proteins, the scramblase Atg9 and the lipid transported Atg2, contribute to phagophore biogenesis. To address this research question, I used cryogenic correlative light and electron microscopy (cryoCLEM). In this cryoCLEM workflow, I vitrified *Saccharomyces cerevisiae* cells and generated ultra-thin lamellae by FIB-milling. Regions of interest on these cellular lamellae were identified using cryogenic fluorescence microscopy prior to acquiring tomographic data on these sites of interest. For this approach, I identified a suitable fluorescent label for Atg9 and chose a deletion mutation, Δsnf7, to stall the progression of phagophores to fully formed autophagosomes in order to accumulate the structures of interest. In order to understand how the function of Atg9 and the interaction of Atg9 and Atg2 affect phagophore morphology, two known mutants, Atg9-basic and Atg2-PM4 were chosen to be studied with cryoCLEM. Atg9-basic is a triple mutant with reduced phosphatidylinositol-3-phosphate translocation activity while Atg2-PM4 is a variant with a mutation disrupting the interaction between Atg2 and Atg9. I segmented the phagophoric membranes to quantify morphological differences across the different cell types. Tomographic data from the Atg9-basic mutant show no detectable differences in phagophore morphology compared to wild-type phagophores. The tomographic data from the Atg2-PM4 mutant show that more than half of the phagophores imaged, had significantly enlarged rims. The in situ tomograms revealed potential modes of phagophore membrane extensions such as vesicle fusion and lipid transfer. The insights gained in this thesis work, contextualise previously reported interaction studies of Atg9 with Atg2 and contribute to our overall understanding of autophagosome biogenesis in *Saccharomyces cerevisiae*.

Abbreviations

TEM	Transmission electron microscopy
(cryo)EM	(Cryogenic) electron microscopy
(cryo)ET	(Cryogenic) electron tomography
CLEM	Correlative light and electron microscopy
FIB	Focussed ion beam
SEM	Scanning electron microscpy
(cryo)FM	(Cryogenic) Fluorescence microscopy
CTF	Contrast transfer function
WBP	Weighted back projection
Sc	*Saccharomyces cerevisiae*
WT	Wild-type
ER	Endoplasmic reticulum
ERES	ER exit site
TGN	Trans-Golgi network
LD	Lipid droplet
MLB	Multilamellar body
IM	Isolation membrane
PAS	phagophore assembly site or pre-autophagosomal site
Atg9	Autophagy-related protein 9
Atg2	Autophagy-related protein 2
Snf7	Vacuolar sorting protein Snf7
PI3P	Phosphatidylinositol-3-phosphate
ESCRT	Endosomal sorting complexes required for transport
EGFP	Enhanced green fluorescent protein
BFP	Blue fluorescent protein

Contents

List of Figures

List of Tables

1 Introduction

1.1 Transmission electron microscopy

Transmission electron microscopy (TEM) is a technique in which a sample is imaged using electrons. In many regards TEM is comparable to light microscopy as electrons can be focussed by electromagnetic lenses, and electrons have wave-like properties (Reimer and Hawkes, 2013). The advantage of electrons is that they have significantly shorter wavelengths than visible light and therefore significantly higher resolution can be achieved with electrons. For instance, at 200 keV the electron wavelength is 2.5 picometers, although the effective resolution limit is at 40 picometer for practical reasons, compared to rougly 200 nanometers in light microscopy (Reimer and Hawkes, 2013). While the currently highest resolution achieved in biological cryogenic TEM is 1.19 Å, resolutions of 2.0 to 4.0 Å are more common (Maki-Yonekura et al., 2023; Yip et al., 2020). Among the disadvantages is the poor penetration depth of electrons in samples, meaning samples have to be extremely thin (below approximately 500 nm for an electron beam at 200 keV) (Reimer and Hawkes, 2013; Kudryashev et al., 2012).

There are a number of central differences in comparison to light microscopy that affect how TEM is carried out and how the microscopes are conceived. First, TEM needs to be carried out under high vacuum to avoid that the electrons are diffracted and decelerated by air in the column (Dykstra, 1992). Another difference is that electrons have to be focussed using electromagnetic lenses, which are essentially coils onto which a current is applied to create a magnetic field (Reimer and Hawkes, 2013). Furthermore, images have to be detected using a photographic film, fluorescent screen or direct electron detector (McMullan et al., 2014). The development of complementary metal oxide semiconductor based direct electron detectors with higher detective quantum efficiency (DQE) significantly improved the signal-to-noise ratio (SNR) at higher spatial frequencies (Henderson,

2015). The DQE is a measure of SNR across different spatial frequencies (Cheng, 2015).

1.1.1 Set-up of a transmission electron microscope

Electrons are emitted at a set energy (usually 80 to 300 keV) from the electron gun. Traditional electron sources include tungsten filaments and lanthanum hexaboride crystals, but the current gold standard for biological cryoEM is a cold field emission gun (FEG) (Reimer and Hawkes, 2013). Using an electric field, electrons are extracted from the FEG resulting in 500-fold higher brightness and better spatial and temporal coherence compared to tungsten filaments (Henderson, 2015). Subsequently, the electron beam is focussed on the sample by a condenser lens system, consisting of two or three condenser lenses, depending on the microscope. Once electrons have passed through and interacted with the sample, the objective lens re-focusses the scattered electrons and magnifies the image (Fig. 1.1). The objective aperture at the back focal plane of the objective lens captures electrons scattered at a high angle, thereby increasing the image contrast (Raimondi and Grinzato, 2021). The intermediate lenses and the projection lens are responsible for further magnifying the image. Usually, TEM manufacturers calibrate the lens currents for pre-set magnifications (e.g., 500x, 24,000x, or 100,000x) (Reimer and Hawkes, 2013). Inelastically scattered electrons have reduced energy (see section 1.1.2) and are removed by an energy filter, which is a prism that selectively bends the electron beam based on the energy of the electrons and a slit of a selected width (Koning et al., 2018). Finally the electrons forming the image hit a detector, nowadays usually a direct electron detector as mentioned in section 1.1 (Henderson, 2015; Dykstra, 1992).

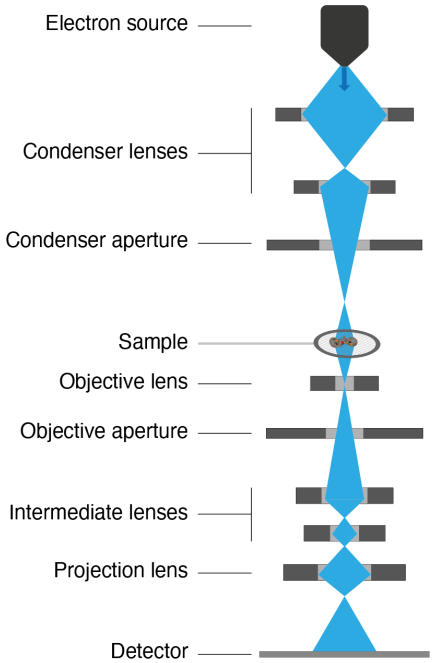

Figure 1.1: Simplified illustration of the beam path of a transmission electron microscope.

1.1.2 Image formation and CTF correction

When electrons pass through the sample, they interact with the atoms in the sample which is what leads to image formation. Unless the electron passes through the sample without interacting with any particles, electrons can either be elastically or inelastically scattered. Elastically scattered electrons do not lose energy but change their trajectory at a high angle. Electrons that are scattered inelastically lose energy by depositing it in the sample which causes radiation damage and structural changes. This includes the excitation of valence electrons which causes the breaking of covalent bonds and production of radicals that cause further damage in the sample. When exposed to an electron beam for extended periods of time or to a high dose of electrons, deformation or bubbling of the sample can occur. Unfortunately, the damaging interactions occur at a 3:1 ratio to the non-damaging ones (Baker and Rubinstein, 2010; Grubb, 1974).

There are two kinds of contrast, amplitude and phase contrast. Amplitude contrast arises from electrons that interact with the sample and do not reach the detector due to scattering. Phase contrast is the dominant form of contrast in biological cryogenic TEM since biological samples are composed of comparatively light atoms (mostly C, O, N, H, and P). Phase contrast is most easily understood when thinking of electrons as waves rather than particles. The scattered electrons experience a phase shift which creates interference of these electrons with each other (Dubochet et al., 1988).

In order to improve contrast, images are acquired at a defocus, because it increases the phase shift between scattered and unscattered waves at low spatial frequencies. However, the increase in contrast causes optical imperfections to alter the image, which can be seen in the power spectra of an electron micrograph as Thon rings (Fig. 1.2, bottom half of circle). The power spectrum in biological TEM is a representation of the absolute-squared Fourier transform of a micrograph in analogy to a genuine diffraction pattern, with spatial frequency increasing towards the boundaries of the circle. The modulation of the image is described by the contrast transfer function (CTF) of the microscope (Dubochet et al., 1988; Frank, 1996):

$$CTF(r) = \sin(\tfrac{\pi}{2} C_S \lambda^3 r^4 + \pi f \lambda r^2) \qquad [1]$$

where C_S is the spherical aberration arising from the lens imperfections, λ is the wavelength of the electrons, f is the applied defocus and r is the spatial frequency. The main variable that affects the CTF is the defocus, which can be computationally estimated from the power spectrum. An example CTF fit is shown in Figure 1.2 as a radially averaged power spectrum graph (magenta line, top right quarter of the circle).

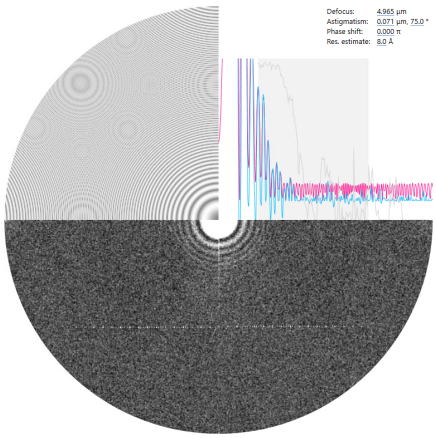

Figure 1.2: Example CTF fit of a tilt frame generated in WARP (Tegunov and Cramer, 2019). The top left quadrant shows the estimated CTF fit, the bottom half shows the power spectrum of the micrograph, and the top right quadrant shows the radial average of both in magenta and blue, respectively.

The micrograph (image) itself is the inverse Fourier transform (*F'*) of the product of the CTF with the Fourier transform (*F*) of the sample (Eq. 2).

$$Image = F'[F(Sample) \times CTF] \qquad [2]$$

$$Sample = F'[\frac{F(image)}{CTF}] \qquad [3]$$

In order to correct the image for the CTF, the Fourier transform of the image is divided by the CTF (Eq. 3). However, it was found that at low SNRs it is more effective to multiply the image by the CTF (Downing and Glaeser, 2008). Experimental CTFs oscillate between 1 and -1, crossing zero several times and progressively diminishing towards higher spatial frequencies (Mindell and Grigorieff, 2003). Since divisions by zero are not possible, the frequency regions where the CTF is zero are excluded. Additionally, the Fourier components in regions were the CTF is negative are multiplied by -1, to have positive contributions

across all spatial frequencies. Since this is essentially a phase shift of 180°, this is referred to as phase flipping (Downing and Glaeser, 2008). At the spatial frequencies where the CTF is zero, there is a loss of information. However, when changing the defocus, the zero crossing points will be at different spatial frequencies. Consequently, by collecting images at different defocus values, the spatial frequency coverage is more complete.

Beam-induced motion of the specimen is detrimental to high-resolution structural information because it causes image blurring. Owing to improved detector technology, micrographs can now be acquired as movies composed of several frames collected over 50 to 100 milliseconds. Consequently, the electron dose deposited on a given region of the sample is distributed over several frames. This concept is referred to as dose fractionation. Movies can be motion corrected by aligning individual frames, as well as aligning smaller subregions of the frames when beam induced motion is unequal across each frame (Brilot et al., 2012; Agard et al., 2014).

1.1.3 Preparation of cryogenic biological samples

In order to withstand the high vacuum in the microscope column, to be natively preserved, and to reduce radiation damage, biological samples are cryogenically fixated (Stark et al., 1996; Nogales and Scheres, 2015). There are two methods to achieve this, high-pressure freezing and rapid plunge freezing. Both methods have in common that they need to achieve vitrification, meaning the water molecules in the sample do not crystallise but instead form amorphous ice. This is important to allow for the sample to be electron transparent (Koning et al., 2018). Additionally, the formation of crystalline ice in biological samples is damaging to relevant features as crystallisation causes expansion of the water, thereby disrupting membranes, protein complexes and other structures (Dobro et al., 2010). Vitrification also allows the sample to be preserved in a frozen-hydrated state in near-native conditions which eliminates artifacts due to dehydration (Dobro et al., 2010;

Agard et al., 2014).

The first technique to vitrify samples is high-pressure freezing, whereby high pressure of more than 2000 bar is applied to the sample while cooling it down. Intracellular or extracellular cryoprotectants may also be added to the samples to prevent the formation of ice crystals (McDonald et al., 2007). The second method, known as plunge freezing is based on freezing a sample extremely rapidly (13k to 15k K per second), most commonly by rapidly immersing a sample into liquid ethane (or an ethane/propane mixture) (Dubochet et al., 1988). Liquid ethane or a liquid ethane/propane mixture is utilised because its thermal conductivity is roughly 300 to 400 times faster than that of liquid nitrogen due to the absence of the Leidenfrost effect. For this method, the sample has to be sufficiently thin to allow for the heat to be extracted rapidly before ice crystals form (Dobro et al., 2010). To achieve this, the sample is applied onto the support film (carbon/gold/SiO_2) on the grid and excess liquid is blotted away (Dubochet et al., 1988). This is only possible if the sample is a form of suspension or solution, such as protein solutions or small cells (Fig. 1.3). Thick samples (>10 µm, large cells or tissue sections) are not suitable for plunge freezing and have to be prepared in a high-pressure freezer (Koning et al., 2018).

When plunge-freezing protein solutions or cell lysate, film-thicknesses of less than 100 nm can easily be achieved by blotting (Dobro et al., 2010; Nogales and Scheres, 2015). However, when studying whole cells or tissues (regardless of the vitrification method), the samples need to be below roughly 500 nm to be electron transparent (depending on the energy of the electrons). Otherwise, the samples must to be thinned afterwards either by focussed ion beam (FIB) milling, cryo-ultramicrotomes or diamond knives (Koning et al., 2018). Since this work focusses on the thinning by FIB milling, other thinning methods will not be discussed in more detail.

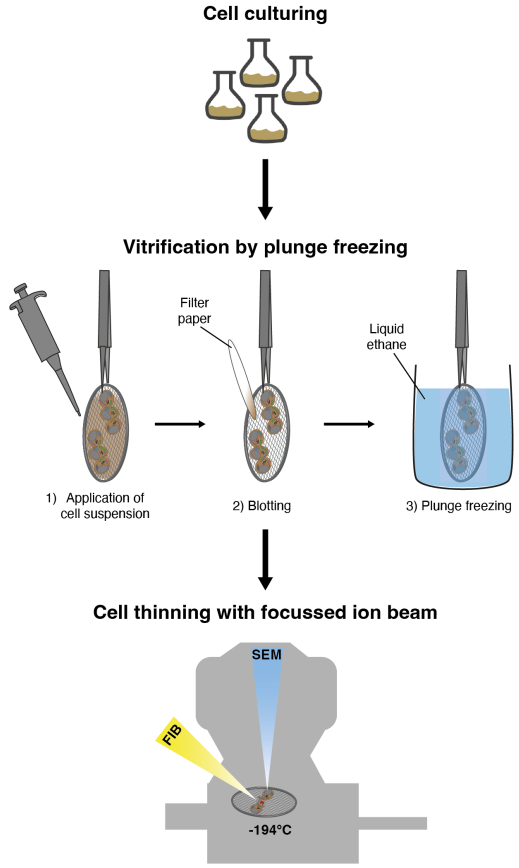

Figure 1.3: Sample preparation workflow for yeast lamellae, beginning with culturing of the cells, vitrifying the cells on cryoEM grids by plunge freezing and finally thinning the yeast cells by focussed ion beam (FIB) milling.

Once cells are vitrified on an EM grid, they can be transferred to a FIB-SEM in order to thin the cells into small slabs, called lamellae (Rigort and Plitzko, 2015). Depending on the size of the cells, one cell can yield one large lamella (usually mammalian cells) or a lamella can be composed of several cells clustered together with surrounding media in the case of bacterial cells and yeast (Koning et al., 2018).

1.1.3.1 FIB milling

The FIB-SEM is a dual beam microscope, the scanning electron beam (SEM) can be used for imaging while the focussed ion beam (FIB) can be used both for imaging as well as removing unwanted material. The ablation process is referred to as FIB milling. The ion species I used in this work for FIB milling, Gallium, is common for cryogenic biological samples, while plasma based on Helium or Xenon is also increasingly used (Rigort and Plitzko, 2015; Koning et al., 2018). To produce a biological lamella of cells, the ion beam is focussed on regions above and below the region of interest (ROI) and the cellular material is ablated by the FIB. This procedure is carried out in steps, milling progressively closer to the ROI with progressively lower beam currents to minimise damage to the ROI by the beam (Fig. 1.4A). Prior to milling, the grid is coated with a protective organo-platinum layer referred to as gas injection system (GIS) layer to prevent the borders of the lamella from being removed too quickly and ripping. The milling progress can be monitored using the SEM (Rigort and Plitzko, 2015). There are two main strategies to produce lamellae for biological cryo electron tomography; either the lamella is milled in such a way that cellular material holds it in place on two sides or the lamella is cut and removed with a gripper or needle from the grid to be placed on another grid (Mahamid et al., 2015; Rigort and Plitzko, 2015). The first approach is schematically represented in Figure 1.4A. When using this approach it is preferable to mill at the most shallow angles (relative to the surface of the grid) possible before other regions of the grid obstruct the beam path in order to maximise the length of a lamella (Fig. 1.4B). Consequently, only a restricted area around the centre of the grid is suitable for cell positioning to produce lamellae. Additionally, the clip rings (metallic ring holding the grid for adaptability of the microscope grid holder) have a special cut-out to accommodate for more shallow milling angles (Wagner et al., 2020). The second approach is called lift-out and is usually chosen

for geometrical reasons, especially when the sample is very thick (usually high-pressure frozen), and the ROI is oriented in an otherwise inaccessible way within the vitrified slab. Performing lift-out is challenging as the throughput is low and the lamellae can easily get damaged or be completely lost during the numerous transfer steps (Mahamid et al., 2015).

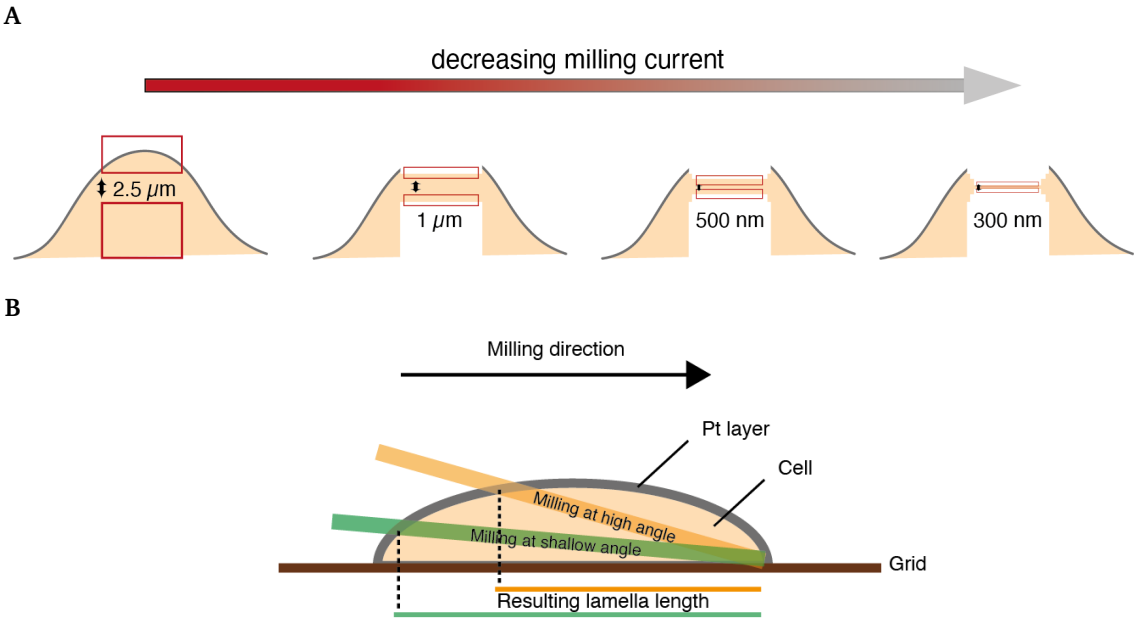

Figure 1.4: Schematic representations of lamella milling. **A**) The placement of milling patterns in relation to ion beam current, viewing cells from the perspective of the beam. **B**) Side view of a cell, illustrating the influence of the milling angle on the lamella length. Figure was conceptionally inspired by Wagner et al. (2020).

1.1.4 Cryo-electron tomography

There are two major measurement approaches in biological cryoEM, single particle analysis (SPA) and cryo-electron tomography (CET). Both of these techniques can be used to collect data with the aim of reconstructing a three-dimensional volume using the Fourier slice theorem. According to this theorem, a slice of the 3D Fourier transform of an object is equivalent to the 2D projection of the object in a particular orientation (Nogales and Scheres, 2015; Sigworth, 2016). Consequently, with enough 2D projections, the object can be reconstructed using Fourier synthesis (Crowther et al., 1970). Where SPA and CET differ is how the 2D projections are obtained. In SPA, the sample consists of many quasi-identical molecules (or particles) randomly oriented in the vitreous ice. With a single micrograph, many particle orientations can be captured (Agard et al., 2014). Thus, by collecting thousands of micrographs, usually a sufficient range of random particle orientations are covered to reconstruct the molecule to high resolution (Nogales and Scheres, 2015).

In cryo-electron tomography (cryoET), there is a single region of interest that is imaged multiple times tilted at different angles (Fig. 1.5) (Koning et al., 2018). In an extension of tomography, called subtomogram averaging (STA), quasi-identical sub volumes are averaged to obtain a higher resolution structure (Wan and Briggs, 2016). Since the sample is held on an EM grid, tilting is restricted before the sample becomes too thick and the metal of the grid edge obstructs the field of view. This effect can be attenuated slightly by positioning the lamella perpendicular to the tilt axis so that the free areas, at the front and end of the lamellae, come into view when tilting instead of the carbon film (Rigort and Plitzko, 2015). Thus, the maximum tilt span is restricted from approximately ± 60°-70°. Consequently, the coverage of 2D projections from different angles is limited in comparison to SPA. The limited viewing angles result in what is known as the missing wedge, a

lack of information in a wedge shape in Fourier space (Koning et al., 2018; Lučić et al., 2013).

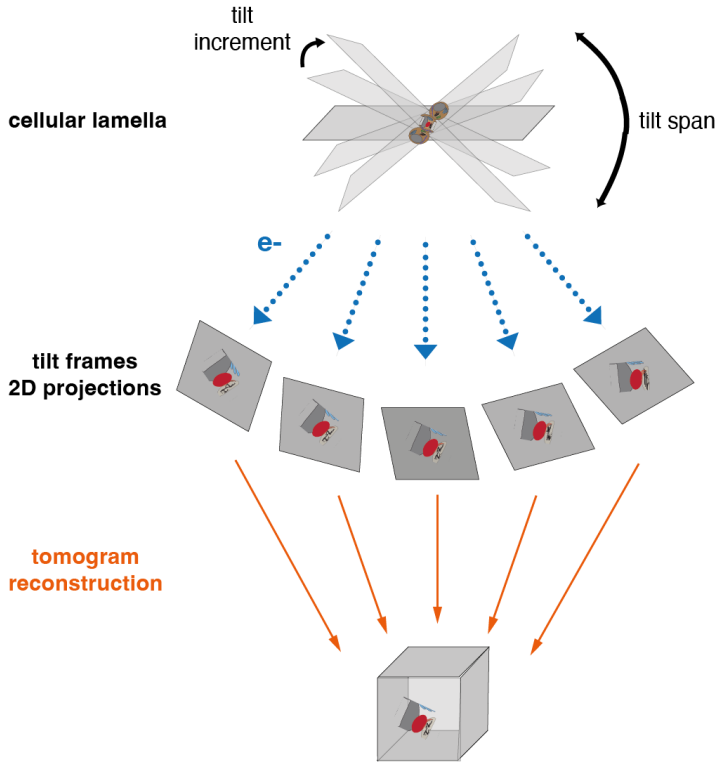

Figure 1.5: Illustration of cellular cryogenic electron tomography, with a cellular lamella being imaged at different tilt angles and the resulting 2D projections being used to reconstruct the imaged volume as a tomogram.

The missing wedge causes an elongation of features in real space in the direction of the electron beam as well as other distortions. In cellular tomograms this means membranes perpendicular to the electron beam are not visible and the display of complete and closed membranes in segmentations is impossible (Lučić et al., 2013).

Another factor that is important in the coverage of 2D projections is the tilt increment, meaning the increment between each tilt frame (Fig. 1.5). Taken together these factors affect the resolution of the reconstruction as stipulated by the Crowther criterion (Eq. 4).

$$m = \pi \frac{D}{d} \qquad [4]$$

where m is the number of views required to reconstruct a particle of diameter D to a resolution of d (=1/R), R being the spatial frequency (Crowther et al., 1970). How to choose the tilt increment and tilt span depends on the resolution that is aimed for, the desired information completeness, and the time available for the measurements. As explained in section 1.1.2, the number of electrons deposited on the sample (referred to as dose) is limited due to radiation damage, which will attenuate the high resolution information first. Therefore, the tilt span and tilt increment have to be chosen weighing information completeness against resolution (i. e. dose) and speed of data collection. Commonly used tilt increments are 2 to 3° and the tilt span can range from ±40° to ±70° (Wan and Briggs, 2016). The total dose is usually limited to about 100 electrons per Å^2 with up to 2 electrons per Å^2 per tilt (Koning et al., 2018).

However, the apparent sample thickness increases with increasing tilt by $\frac{1}{\cos\theta}$, where θ is the tilt angle (Koning et al., 2018). At high tilt angles and sample thicknesses, there is an increased likelihood of multiple scattering events of electrons with atoms in the sample (König et al., 2014). As a consequence, the dose per tilt frame can be increased proportionally (Mastronarde, 2003). Equally, to address this issue among others, Hagen et al. (2017) devised a tilt scheme, referred to as dose-symmetric tilt scheme, whereby tilt frames are collected alternatingly on both sides of 0° such that the high resolution information is retained optimally (Fig. 1.6, right). This method is based on the fact that the high-resolution information beyond 5 Åis lost after roughly the first 20 to 30 electrons per Å^2 accumulated dose (Fromm et al., 2015). As a result, the maximum tilt range and

a higher total electron dose can be applied because higher tilts can easily be discarded without losing high resolution signal. Furthermore, the sample may bend, distort, or move while exposing it to electrons which means the sample imaged initially is not the same as later in the tilt series. When using a bidirectional tilt scheme, such beam-induced alterations result in stark differences in the sample between adjacent tilts close to 0° (Fig. 1.6, center). In the dose-symmetric tilt scheme these changes occur gradually with increasing tilt which makes the tilt series more smooth and therefore the alignment of tilt frames less error prone (Hagen et al., 2017). Taken together the advantages of the dose-symmetric tilt scheme have made it the gold-standard in acquisition of cryo-electron tomograms over more traditional approaches such as the continuous/unidirectional tilt scheme and the bidirectional tilt scheme (Fig. 1.6) (Koning et al., 2018).

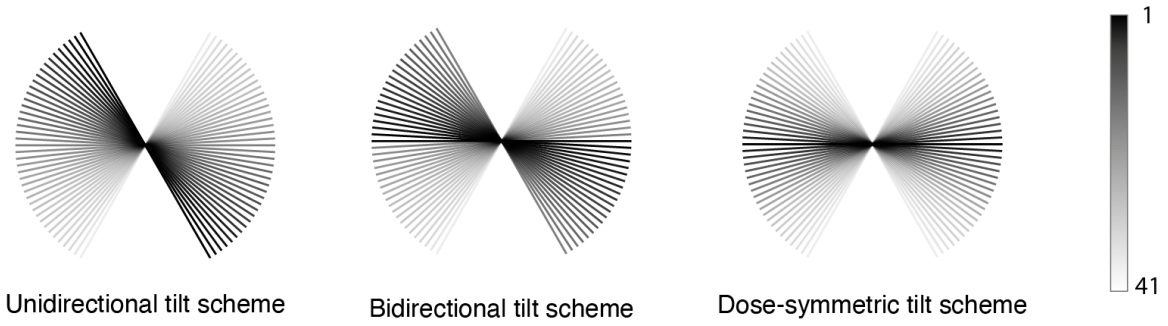

Figure 1.6: Illustration of different tilt schemes. Gray scale shows the order in which the tilt frames are recorded, with the darkest shade being the first tilt acquired and the lightest shade the last tilt frame acquired. This illustration was conceptually inspired by Hagen et al. (2017).

1.1.4.1 Processing and reconstruction of tomograms

As previously explained, micrographs are pre-processed, namely by CTF estimation, phase flipping, and motion correction (section 1.1.2) and removing of extreme data values usually caused by x-rays (Koning et al., 2018). It is worth mentioning that in cryoET, as opposed to SPA, the defocus determination is more challenging due to the much lower

SNR leading to poor Thon ring signal which is caused by the lower dose per micrograph (Wan and Briggs, 2016). In the case of subtomogram averaging, local defocus determination and CTF correction may be required because the defocus can vary significantly in thick samples and thus lead to individual sub-volumes having different defocus values depending on where they are located within the sample (Wan and Briggs, 2016). After pre-processing, the tilt series needs to be aligned for the following parameters: X-Y shifts due to imperfections of the microscope goniometer, image rotation and magnification due to slight non-eucentricity (goniometer imperfections), which leads to the sample being at slightly different height and thus being magnified slightly differently at different tilt increments, and tilt angle which can be slightly different from the set tilt angle (goniometer imperfections) (Pyle and Zanetti, 2021). For an initial coarse alignment, tilt images are cross correlated (Koning et al., 2018). There are different ways the finer tilt series alignment can be carried out. If possible, one can add gold beads (5-20 nm diameter) to the sample before vitrification. These beads are easily be identified due to their extremely high contrast and can thus be tracked throughout the tilt series by automated-picking algorithms (Nickell et al., 2005; Wan and Briggs, 2016), which is also known as bead-tracking alignment. Another method, so-called patch-tracking approach, uses the cross-correlation of regions of the micrograph (patches) across the tilt series (Noble and Stagg, 2015) for alignment. In many cases, patch-tracking is less accurate than bead-tracking, but it is a viable alternative for samples to which gold beads cannot be added (Wan and Briggs, 2016).

For the reconstruction of a tomogram, there are several different approaches. The most commonly used reconstruction method that I also used in this work is weighted back projection (WBP). To understand this method, simple back projection needs to be explained first. Simple back projection is based on the previously mentioned Fourier slice theorem. The tilt images are back projected into a real-space volume (Radermacher, 1992). Thus,

simple back projection algorithms are a real-space version of Fourier synthesis (Koning et al., 2018). WBP is a version of back projection in which the images are weighted prior to back projection in order to balance overrepresented spatial frequencies (Radermacher, 1988). Back projection approaches usually yield tomograms with reduced contrast and are thus sometimes not as readily interpretable as tomograms from iterative reconstruction methods. However, WBP is considered the gold-standard reconstruction method especially to achieve sub-nanometer resolutions in STA (Wan and Briggs, 2016).

Once the reconstructed tomogram has been obtained, further processing can be done such as STA, template matching or segmentation. Since segmentation was performed in this thesis to allow further analysis of tomographic data, only segmentation will be further discussed. Segmentation assignment of pixels or voxels corresponding to meaningful objects within the tomographic volume (Frangakis and Hegerl, 2006). Segmentation can be done interactively or with computer algorithms. Many of these algorithms are now based on neural networks which are trained with manually curated segmentation data (Isensee et al., 2021). In this work, MemBrain v2 was used for automated segmentation followed by manual curation of regions where the pre-trained model was not performing sufficiently well (Lamm et al., 2024).

1.2 Cryogenic Fluorescence Microscopy

Fluorescence microscopy where samples are kept at cryogenic temperatures was developed about 15 years ago with the development of so-called cryo-stages (Schwartz et al., 2007; Sartori et al., 2007; Van Driel et al., 2009). There are several advantages to conducting fluorescence microscopy at cryogenic temperatures. Most importantly, cryogenic fluorescence microscopy (cryoFM) allows to image cells in fixed but near-native conditions (see section 1.1.3) without having to use chemical fixation agents that often introduce artifacts to the cellular environment (Kaufmann et al., 2014). In many cases, cryoFM is chosen as a method in the context of cryogenic correlative light and electron microscopy (see section 1.3) where the sample has to stay in a frozen-hydrated state to maintain the structural integrity of the structures of interest across several imaging modalities (Kaufmann et al., 2014). The following chapter will introduce cryoFM before bringing it into context with cryogenic correlative light and electron microscopy.

1.2.1 Sample cooling during cryogenic fluorescence microscopy

Three different approaches were developed to cool the sample while imaging. The first one by Schwartz et al. (2007) was designed for un upright microscope, where the sample is clamped on a silver plate which is cooled by cold gaseous nitrogen from an external reservoir. Another approach by Sartori et al. (2007) uses an inverted microscope and has glass slides on both sides of the grid, i.e., between the sample and the long-distance objective and above the grid. The sample is held in a temperature-conductive metal cartridge that is cooled by two liquid nitrogen containing reservoirs. The third approach by Van Driel et al. (2009) was a modification of a commercially available microscope stage, also intended for an upright microscope. The sample rests on a metal block that is cooled by liquid nitrogen passing through cooling lines in the block. Initially in this design the

sample was also covered by a glass slide, but this was eventually removed, which allowed to use an objective with closer working distance. In this study, I utilised an updated version of the latter cryostage design. All three cryostage designs differ on how sample cooling is ensured, but they share the same imaging limitations that will be explained below.

1.2.2 Limitations and altered photophysical behaviour under cryogenic conditions

With the currently available cryostages, samples are held in nitrogen vapour phase or air. Consequently, only dry lenses with comparatively long working distances can be used. Therefore, objectives are limited in numerical aperture (NA) to below 0.8, which effectively means the cone of collected light (i.e. sensitivity and resolving power) is more limited compared to room temperature imaging where immersion oil and shorter working distances can be used (Kaufmann et al., 2014; Dahlberg and Moerner, 2021). With the advent of cryoFM, the changes in photophysical behaviour of fluorophores under cryogenic conditions could be studied. One of the observed changes is the reduction or even complete absence of photobleaching of for instance green fluorescent protein (GFP), red fluorescent protein (RFP) and other fluorophores (Schwartz et al., 2007; Tuijtel et al., 2017; Weisenburger et al., 2014). Reduced photobleaching can be explained by lower accessibility and freedom of movement of molecular oxygen that is the main acceptor during photo oxidation (Dahlberg and Moerner, 2021).

Another phenomenon that is a consequence of vitrification caused by the rigid positioning of fluorescent labels in vitreous ice is anisotropy in excitation and emission. Anisotropy can lead to dipole emission patterns that result in a shift of detected fluorescence relative to the emission under room-temperature conditions when they are isotropic (Dahlberg and Moerner, 2021). A narrowing of absorption and emission spectra at low temperatures has also been reported in the context of single molecule spectroscopy (Moerner and Orrit, 1999).

Furthermore, it was found that photoswitching under cryogenic temperatures is challenging or impossible for some fluorophores as many switching mechanisms depend on large conformational changes or thermal energy both of which are more limited under cryogenic conditions (Dahlberg and Moerner, 2021; Faro et al., 2010). The photoswitching efficiency in vitrified samples for different photoswitchable tags is yet to be determined systematically.

Moreover, the SNR has been found to be reduced in cryoFM. As previously mentioned, under cryogenic conditions fewer reactive oxygen species are available due to restricted diffusion. These reactive oxygen species also serve as a quenching pathway for photoexcited triplet states, meaning such triplet states will be longer-lived (milliseconds instead of microseconds) (Dahlberg and Moerner, 2021; Moerner and Orrit, 1999). Consequently, substantial fractions of fluorophores may be in triplet states, effectively causing a reduction in brightness as high as 10-fold compared to room-temperature FM (Kaufmann et al., 2014). As a result, cryoFM has a substantially reduced SNR (König et al., 2014). Several kinds of biomolecules were found to be mainly responsible for inherent autofluorescence; molecules containing aromatic rings such as aromatic amino acids, reduced pyridine nucleotides (NADH), lipid pigments, flavins (FAD/FADH), porphyrins (e.g. hematoporphyrin), and chlorophyll (Carter et al., 2018). A systematic study of autofluorescence in vitrified human cells was carried out by Carter et al. (2018) when the sources of autofluorescence were investigated by cryoET after being identified in cryoFM. They found many autofluorescent structures to be multilamellar bodies or membrane-enclosed crystalline structures. Such systematic studies have not been conducted in yeast.

Taken together the altered photophysical behaviour of samples under cryogenic conditions needs to be taken into consideration when designing a cryoFM experiment.

1.2.3 Devitrification

Keeping the sample continuously vitrified is important for a cryogenic correlative light and electron microscopy workflow. Therefore, additionally to keeping the cryoEM grid cold, illumination used for excitation has to be limited to prevent local devitrification (Metskas and Briggs, 2019; Dahlberg and Moerner, 2021). A number of considerations were put forward to reduce the likelihood of devitrification during cryoFM by (Last et al., 2023). Support film material and thickness of a cryoEM grid, grid and support film geometry, as well as integrity of the support film were discussed as factors that influence the maximum illumination power density that can be applied to a vitrified sample. For instance, gold, SiO_2 or formvar were found to be better than amorphous carbon support film. Gold and copper grid material was concluded to be equivalent. A previous study reduced devitrification of the sample by addition of ethylene glycol and poly-(saccharose-co-epichlorhydrin) as well as by pulsing the light exposure (Chang et al., 2014). Additionally, ice thickness, the integrity of the support film, excitation wavelength and the general composition of the sample were suggested to play a role in how much illumination power density a sample can withstand before devitrification (Dahlberg and Moerner, 2021; Last et al., 2023). In summary, the excess energy deposited in the sample that is not used for excitation of molecules needs to be dissipated. Since so many factors influence how efficient this dissipation can be, more systematic studies are required to understand and ultimately arrive at an optimised support choice and illumination strategy.

1.3 Correlative light and electron microscopy (CLEM)

Fluorescence microscopy (FM) can detect a specific fluorescent tag or dye but does not directly reveal specific morphological or structural information of the cellular context in which the signal was detected (Schorb and Briggs, 2014). Additionally, the resolution of light microscopy is limited to about 200 nm (Kaufmann et al., 2014). In contrast, *in situ* electron microscopy can provide high resolution structural and morphological information of a cellular environment, but without the molecular specificity for a structure of interest. CLEM (Correlative Light and Electron Microscopy) combines the advantages of these two techniques, namely the high resolution of electron microscopy and the specific detection of a labelled material in fluorescence microscopy. CLEM can be carried out in many different configurations, for instance with live cell imaging before fixing and embedding the cells in resin and carrying out heavy-metal staining EM (Hodgson et al., 2014). As this work focusses on a version of CLEM in which both microscopy forms are carried out with the sample under cryogenic conditions (cryoCLEM), the following section will be restricted to explanations of the specificities of this particular version of CLEM.

1.3.1 cryogenic CLEM

In contrast to other forms of *in situ* electron microscopy, cryoCLEM has the advantage that the sample is kept in a frozen-hydrated form after vitrification which is near-native conditions (Koning et al., 2018). Consequently, as with the cryoEM samples described in section 1.1.3 the samples need to be kept below -140°C throughout this correlated set-up to prevent the formation of crystalline ice (Schorb and Briggs, 2014). For this reason, ways of keeping EM grids below -140°C while conducting fluorescence microscopy have been developed and were discussed in section 1.2.

In the form of cryoCLEM where both microscopy forms are conducted at cryogenic temperatures, the fluorescence data can be used to either aim that the ROI remains in the final lamella or to find the ROI in the final lamella for TEM data collection (Zhu et al., 2021; Schorb and Briggs, 2014). The former is referred to as targeted milling which requires the correlation of 3D fluorescence data with a 2D FIB image, using software such as 3DCT (Arnold et al., 2016) or corRelator (Yang et al., 2021). Based on this information, the FIB-SEM microscope operator or an automated software has to decide on the milling patterns which will result in removing cellular material from around the ROI. The second approach of targeting the ROI for TEM data acquisition requires only a 2D-to-2D correlation of a FM image of the lamella and an overview of the lamella in the TEM. Once correlated, for instance in SerialEM (Mastronarde, 2003) it is possible to precisely navigate to the ROIs and collect cryoTEM data on those (Koning et al., 2018). The correlation accuracy is important in both correlation approaches. Both approaches can also be carried out on the same sample, first to obtain a lamella from targeted milling and subsequently to confirm the presence of the ROI in the lamella or to guide the TEM data collection (Koning et al., 2018; Wagner et al., 2020).

Depending on which approach is chosen, the cryoFM measurement needs to be carried out before the preparation of lamellae in the FIB-SEM or after. The order of imaging steps in the workflow also affects the cryogenic sample transfer steps and the ice crystal contamination considerations. Ice crystal contamination can be detrimental to detecting cells or lamella in FIB, SEM and TEM (see section 1.1 and 1.1.3). Thus the level of contamination influences the successful production of a lamella or it can inhibit measurement of tomograms on correlated lamellae.

1.3.2 Spatial correlation between light and electron microscopy

A critical step in the CLEM work is to determine the spatial relationship between two sets of data from different imaging modalities to each other. For this operation it is required to find landmarks or registration points that are equivalent in both FM and TEM data. Registration points can be features of the grid, for instance broken grid squares or they can be fiducials in the sample (Schorb and Briggs, 2014). Fiducials can be fluorescently labelled cellular structures (e. g. dyed lipid droplets or mitochondria) or fluorescently labelled polystyrene microspheres, added to the cells before plunge freezing (Schorb and Briggs, 2014; Carter et al., 2018). With one registration point the only operation that is possible to carry out is translating one data set relative to another. With two registration points translation and rotation are possible, while with three to four registration points translation, rotation, and scaling can be carried out with one data set relative to another. Finally, with five or more registration points a full linear transformation including translating, rotating, scaling, stretching and potential inversion is possible (Mastronarde, 2003).

For an accurate correlation it is important to consider in advance which kinds of features will be available (intracellular or extra cellular) and which steps need to be taken during sample preparation (dyeing cells, supplementation of fluorescently labelled polystyrene microspheres or use of finder grids with macroscopic markings). These considerations can help to maximise the number of available registration points and hence the possible correlation accuracy.

1.4 Autophagy - cellular self-eating

Autophagy is a highly conserved homeostatic pathway which delivers cytoplasmic material into the lysosomal system for degradation and recycling of molecular components (González-Polo et al., 2016). This cytoplasmic material can include long-lived proteins, damaged organelles and even intracellular pathogens (Levine and Deretic, 2007). Autophagy (*auto* gk. for 'self', *phagein* gk. for 'to eat') is a complementary process to the ubiquitin-proteasome pathway, which targets short-lived proteins (Webber and Tooze, 2010). This process was first observed in the 1950s in a variety of mammalian cells, mostly by electron microscopy, before being systematically and genetically dissected starting from 1993 in *Saccharomyces cerevisiae* (Tsukada and Ohsumi, 1993; Ohsumi, 2014). For his discoveries of autophagic mechanisms, Yoshinori Ohsumi was awarded the Nobel Prize in Physiology or Medicine in 2016 (Tooze and Dikic, 2016).

There are three main types of autophagy distinguished based on their mechanism of degradation: macroautophagy, microautophagy, and chaperone-mediated autophagy (CMA) (Klionsky et al., 2007). Macroautophagy has been described as a non-specific sequestration of cellular components in the cytoplasm to the autophagosome. The autophagosome is a double membrane compartment and develops from what is called the pre-autophagosomal site or the phagophore assembly site (PAS) at which a number of proteins assemble to facilitate the enclosure of the cargo (Mizushima et al., 2011; Hollenstein and Kraft, 2020). In contrast, microautophagy is the process of targeted isolation of cargo by invagination of vacuolar or lysosomal membrane (Klionsky et al., 2007). Macro- and microautophagy may occur simultaneously in order to regulate the lysosomal membrane size, as macroautophagy causes growth of the lysosome and microautophagy causes shrinkage of the lysosome (González-Polo et al., 2016). Chaperone-mediated autophagy (CMA) is a process by which soluble proteins are taken to the lysosome by chaperones such as heat shock

cognate protein 70 and delivered into the lysosome with the help of lysosomal- associated membrane protein 2 (Klionsky et al., 2007). CMA is exclusive to mammalian cells (Massey et al., 2006).

While autophagy is a protective mechanism of the cell relevant for lifespan extension, cell development, innate and adaptive immunity, tumour genesis suppression and triggering cell death (Bursch, 2001; Levine and Deretic, 2007; Webber and Tooze, 2010; Li et al., 2020b), it has also been linked to numerous diseases such as cancer, aging, neurodegenerative, cardiovascular and inflammatory diseases, as well as muscle atrophy and obesity (González-Polo et al., 2016). Furthermore, autophagy has even been described as having both a tumour suppressive and a tumour promotive role (Singh et al., 2018). The diversity of these diseases highlights the central position of autophagy in cellular homeostasis and by elucidating its mechanism in molecular detail it will be possible to understand and search for targeted treatments for the afore-mentioned diseases.

1.4.1 Autophagosome biogenesis

Using *Saccharomyces cerevisiae* (hereafter referred to as yeast) genetic screens it was possible to identify more than 30 proteins that compose the autophagy machinery and carry the acronym Atg, denoting AuTophaGy-related genes or proteins (when referring to the yeast proteins the A is capitalised, when referring to the gene the acronym is not capitalised) (Suzuki et al., 2001; Webber and Tooze, 2010; Xie and Klionsky, 2007). Among these proteins is a subset that was found to be relevant across many subtypes of autophagy and is known as the core machinery (Xie and Klionsky, 2007; Suzuki and Ohsumi, 2010). This machinery can be divided into six evolutionarily conserved groups that form complexes in the course of autophagosome biogenesis (Suzuki and Ohsumi, 2010; Noda, 2023).

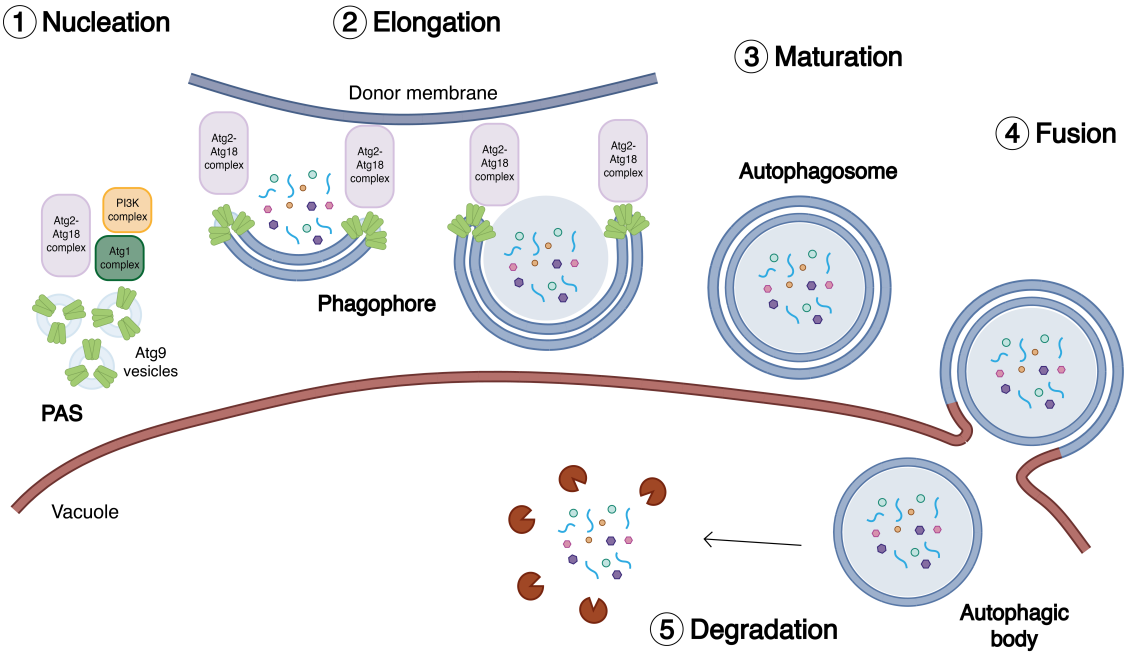

Figure 1.7: The five stages of autophagy and the role of Atg9 and the Atg2-Atg18 complex therein.

Macroautophagy (hereafter referred to as autophagy) proceeds in five stages; nucleation, elongation, maturation, fusion and degradation (depicted in Fig. 1.7). Firstly, nucleation can be triggered by nutrient deprivation, lack of auxotrophic amino acids or by an augmented energy requirement. During starvation for instance nucleation is induced by inhibition of the target of rapamycin complex 1 (TORC1) which causes a lack of phosphorylation of Atg13 (Kamada et al., 2000). This phosphorylation state leads to the assembly of the Atg1 complex at the PAS. Dephosphorylated Atg13 binds the scaffold protein Atg17 (or Atg11 in the case of selective autophagy) and Atg1 which gets more active through the interaction with Atg13 (Suzuki and Ohsumi, 2010; Hollenstein and Kraft, 2020). It has been suggested that Atg1 complexes form phase separated droplets mediated by Atg13, but it is unclear whether this form of phase separation is sustained throughout autophagy (Fujioka et al., 2020).

Next, Atg9 vesicles get recruited to the PAS to initiate the formation of an isolation mem-

brane (IM) (Noda et al., 2000; Yamamoto et al., 2012). The vesicles provide a so-called membrane seed as well as a platform for subsequent autophagy protein recruitment (Yamamoto et al., 2012; Sawa-Makarska et al., 2020). Subsequently, the phosphatidylinositol 3-kinase (PI3K) complex is recruited, generating phosphatidylinositol-3-phosphate (PI3P). The presence of PI3P in the membrane leads the Atg2-Atg18 complex to localise to the PAS (Hollenstein and Kraft, 2020). The second step in autophagy, elongation, is facilitated largely by the Atg2-Atg18 complex that mediates the lipid transfer from a donor membrane to the IM until it fully engulfs the cargo (Osawa et al., 2019; Dabrowski et al., 2023). While the endoplasmic reticulum (ER) has been accepted as a major lipid source for IM elongation, other organelles such as mitochondria have also been proposed (Reggiori et al., 2005; Dabrowski et al., 2023). Independently from the Atg2-Atg18 complex but dependent on PI3P presence in the IM, the Atg12-Atg5-Atg16 ubiquitin-like conjugation machinery is recruited (Hollenstein and Kraft, 2020; Noda, 2023). The Atg12 ubiquitin-like protein is conjugated to Atg5 by the E1-like protein Atg7 and E2-like protein Atg10 (Mizushima et al., 1998; Noda, 2023). This Atg12-Atg5 conjugate will then interact with Atg16 that is the E3-like protein mediating the conjugation of the ubiquitin-like protein Atg8 with phosphatidylethanolamine (PE) in the isolation membrane (Hollenstein and Kraft, 2020; Noda, 2023). This anchors Atg8 to the phagophore membrane, which is a central requirement for autophagosome biogenesis. Lipidated Atg8 has been shown to perturb the isolation membrane by increasing the outer membrane area relative to the inner membrane area, which is essential for efficient autophagosome formation (Maruyama et al., 2021).

During maturation, the phagophore will seal into a fully closed autophagosome with its characteristic double membrane. This process is mediated by the Rab-GTPase Vps21 and the ESCRT III machinery, specifically Snf7 (Zhou et al., 2019). After completion of autophagosome formation and before the autophagosome fuses with the lysosome (or

vacuole in plants and yeast), core autophagy components are recycled back to a peripheral location to function in the next autophagy process again (Xie and Klionsky, 2007). Whether and for how long the different Atg proteins reside on the autophagosomal membrane is species dependent (Mizushima et al., 2011). The fusion stage of autophagy is mediated by the Rab-GTPase Ypt7 and vacuolar SNAREs such as Ykt6 and Vam3 (Darsow et al., 1997; Kirisako et al., 1999; Bas et al., 2018). Once fused, the now single-membrane bounded autophagic body will be degraded and the cargo components recycled in the lysosome (González-Polo et al., 2016). In yeast, the full autophagic process from initiation to degradation, is estimated to take seven to nine minutes, while the formation of an autophagosome is suggested to require four to five minutes (Shibutani and Yoshimori, 2014).

1.5 Atg9 - the central transmembrane protein of autophagy

Atg9 is the only multi-spanning transmembrane protein among the core autophagy machinery and has a reported molecular weight of 125 kDa (Noda et al., 2000). Atg9 biogenesis occurs at the trans-Golgi network (TGN) and is likely to involve Atg27 and Atg23 (Mari et al., 2010; Reggiori et al., 2004; Young et al., 2006; Yen et al., 2007; Backues et al., 2015). In the absence of Atg27, Atg9 mislocalises and is degraded in the vacuole (Ungermann and Reggiori, 2018). Both in mammalian and in yeast cells, Atg9 was found to be stored in vesicles that are located in the cytoplasm and recruited to the PAS during nucleation (Yamamoto et al., 2012; Suzuki et al., 2015; Imai et al., 2016). The so-called Atg9 vesicles contain 24 to 32 Atg9 molecules per vesicle and are 30-60 nm in size, as determined by Yamamoto et al. (2012) using dynamic light scattering, single particle tracking and electron microscopy. These Atg9 vesicles are thought to form a membrane 'seed' from which the IM expands (Suzuki et al., 2013; Sawa-Makarska et al., 2020). During IM elongation Atg9 localises at the phagophore rims (Fig. 1.7) (Gómez-Sánchez et al., 2018; Sawa-Makarska

et al., 2020; Matoba et al., 2020). In addition to Atg9 vesicles there are four main other Atg9 localisations; the TGN, endosomes or endosome-like structures, mitochondria and the plasma membrane, albeit these have been found to be organism dependent (Reggiori et al., 2004; Reggiori and Klionsky, 2006; Reggiori et al., 2005; Ungermann and Reggiori, 2018). Since the early 2000s it has been known that Atg9 is essential for autophagy, despite its exact function remaining elusive (Noda et al., 2000; Lang et al., 2000; Suzuki et al., 2013). However, when both the human and fission yeast (*Schizosaccharomyces pombe*) atomic structures were solved to 2.9 Å-3.4 Å resolution, it became apparent that Atg9 is a lipid scramblase (Maeda et al., 2020; Matoba et al., 2020; Guardia et al., 2020). This finding was supported by *in vitro* biochemical assays showing the transport of lipids, most notably PI3P from outer to inner leaflets of liposomes (Maeda et al., 2020; Matoba et al., 2020). These structures confirmed prior data pointing to essential self-interaction of Atg9 in a trimer (He et al., 2008; Papinski et al., 2014; Lai et al., 2019). Atg9 was shown to be a domain-swapped homotrimer sharing two transmembrane helices with a neighbouring protomer (Maeda et al., 2020; Matoba et al., 2020).

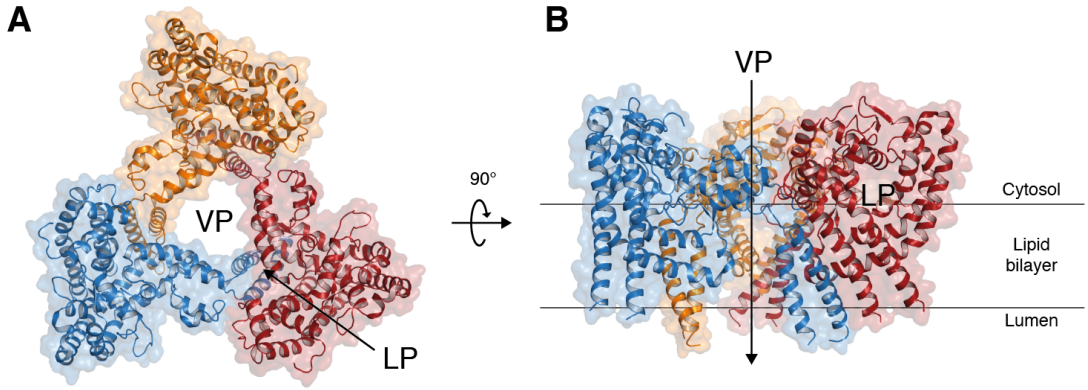

Figure 1.8: Cartoon representation of the atomic model of fission yeast Atg9 (PDB: 7D0I), elucidated by Matoba et al. (2020). The two kinds of pores, vertical pore (VP) and lateral pore (LP) are indicated by arrows both in **A**) the top view and **B**) the side view of the Atg9 trimer.

Based on the sequence, it was predicted that Atg9 has six to eight transmembrane helices. However, the experimentally determined structure of Atg9 revealed only four transmembrane helices (Noda et al., 2000; Maeda et al., 2020). Two other α-helices are located in the cytosolic leaflet of the membrane, parallel to the membrane plane (Maeda et al., 2020) (Fig. 1.8). The two large soluble domains on the cytosolic side of the membrane have been shown to interact with several autophagy proteins, including Atg1, Atg13, Atg17, Atg11 and Atg2 (Papinski et al., 2014; Suzuki et al., 2015; Sekito et al., 2009; He et al., 2006; Gómez-Sánchez et al., 2018). The Atg9 trimer has two kinds of pores, one central pore per trimer called the vertical pore (VP) and one lateral pore (LP) in each protomer (Fig. 1.8). These pores were shown to be important for the enzymatic function of Atg9 through mutational studies (Matoba et al., 2020). A low resolution (32 Å) cryoEM map showed that the C- terminal region of human ATG2A interacts directly with the C-terminal region of human ATG9A (van Vliet et al., 2022). Furthermore, a not yet peer-reviewed structural study of human ATG2A and ATG9A to 7 Å resolution suggested that the lipid transfer cavity of ATG2A was located near the entry to the lateral pore of an ATG9A protomer (Wang et al., 2023). These findings underpin the current phagophore elongation model, whereby Atg2 funnels lipids directly to Atg9 which distributes these across the membrane leaflets therefore maintaining lipid profile asymmetry (further elaborated in section 1.7).

1.6 Atg2 - the lipid supply machinery for phagophores

Atg2 is a large protein composed of 1,592 amino acids and a calculated molecular weight of 178 kDa. Since most of the autophagy machinery localises at the PAS even in the absence of Atg2, it was hypothesised that Atg2 was involved in a later stage of the autophagosome biogenesis process (Suzuki et al., 2007). Both Atg9 and Atg18 were shown to interact with the C-terminal region of Atg2 (Gómez-Sánchez et al., 2018; Kotani et al., 2018). The interaction between Atg2 and Atg18 has been shown to be essential for autophagy (Obara et al., 2008; Kobayashi et al., 2012; Rieter et al., 2013), but the targeting of Atg2 to the PAS, more specifically to the phagophore rims, is dependent on Atg9 and PI3P (Gómez-Sánchez et al., 2018). However, the exact role of Atg2 was not clear until the first studies found a localisation of the human homologue ATG2A at lipid droplets and seemingly a regulatory function of lipid droplet size (Velikkakath et al., 2012; Pfisterer et al., 2014). Additionally, Atg2 was shown to localise to the contact site between the phagophore and the endoplasmic reticulum exit site (ERES), from which transmembrane proteins and COPII vesicles arise (Graef et al., 2013). In 2017, Atg2 was first suggested to be required for the recruitment of lipids to the IM (Hirata et al., 2017). In the same year the first low resolution structural information was published, revealing the architecture of the human homologue complex of ATG2B-WDR45 and ATG2A-WIPI4 (Fig. 1.9B), respectively (Zheng et al., 2017; Chowdhury et al., 2018). These structures showed that ATG2 is an elongated rod of about 20 nm. Additionally, one of these studies visualised the bridge-like vesicle tethering of the ATG2A-WIPI4 complex from PI3P-free vesicles to PI3P containing vesicles by negative-staining EM (Chowdhury et al., 2018). Also in yeast, it was shown that Atg2 had two membrane binding regions, one at the N-terminus and the other at the C-terminus, responsible for binding the ER and IM, respectively (Kotani et al., 2018).

Higher resolution structural information helped in understanding of Atg2 function. A crys-

tal structure of an N-terminal fragment of *Schizosaccharomyces pombe* Atg2 showed that at the core there is a hydrophobic cavity which accommodates the acyl chains of phosphatidylethanolamine without specificity for the head group (Osawa et al., 2019). *In vitro* studies also showed that Atg2 transfers lipids without head-group specificity (Osawa et al., 2019). Both human ATG2A and ATG2B were also shown to have lipid transfer activity which suggest the evolutionary conservation of this function (Valverde et al., 2019; Maeda et al., 2019; Osawa et al., 2020). Low resolution cryoEM data of full-length human ATG2A shows an approx. 16 nm long groove, along the long axis of the Atg2 rod (Valverde et al., 2019). A not yet peer-reviewed structural study of human ATG2A and WIPI4 to 3.2 Å resolution confirmed the presence of the hydrophobic groove (Wang et al., 2023). Mutation of a range of hydrophobic residues to hydrophilic ones within this grove was shown to inhibit lipid transfer activity (Valverde et al., 2019). Taken together, these data led to the current model of phagophore elongation, whereby Atg2 mediates the lipid transfer by bridging the donor membrane, often ER, to the IM.

Homologues of Atg2 share a similar architecture and based on this two protein families were proposed, the bridge-like lipid transfer protein (BLTP) superfamily and the repeating β-groove (RBG) protein family (Braschi et al., 2022; Neuman et al., 2022). Some of these protein family members, such as Vps13 and Csf1 have been shown to also have a lipid transport activity (Li et al., 2020a; Toulmay et al., 2022). Vps13 was even shown to act as a lipid transporter in autophagy, complementary to Atg2 (Dabrowski et al., 2023). To illustrate the key features, the AlphaFold model of yeast Atg2 along with the negative-staining EM map of human ATG2A-WIPI4 are shown in Figure 1.9 (Wang et al., 2023). The β-sheets characteristic of the RBG protein family are highlighted in orange. The involvement of BLTP superfamily or RBG family members, other than Atg2, in autophagy requires further studies to fully understand how the lipid supply to the phagophore is mediated and regulated.

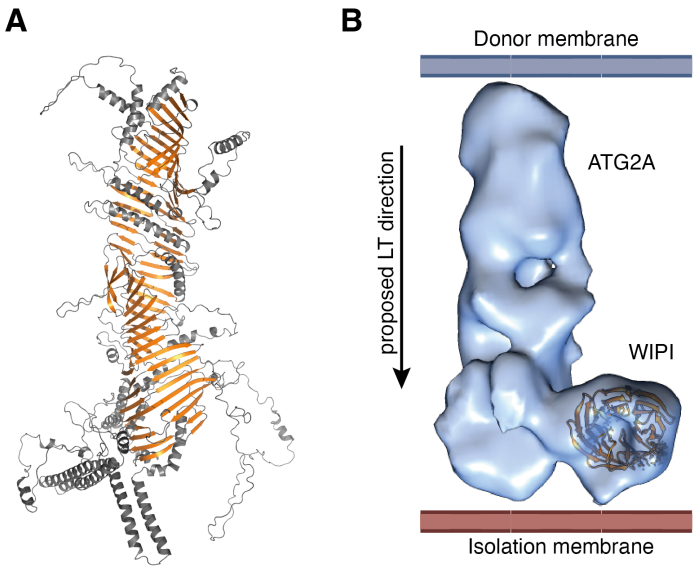

Figure 1.9: A) Cartoon representation of the alphafold model of yeast Atg2 (Uniprot code: P53855). The characteristic β-sheets are coloured in orange. **B**) Negative-staining EM map of ATG2A-WIPI4 fitted with the atomic model of WIPI3 (PDB: 6IYY). In both panels the proteins are oriented with the N-terminal region at the top and the C-terminal region at the bottom, which means the lipid transfer (LT) direction is downwards.

1.7 Unidirectional lipid transport from ER to phagophore

A long-established observation that pointed towards a specific lipid source or delivery mechanism in autophagy was that the IM contains very few proteins compared to other cellular membranes (Cheng et al., 2014). Since Atg9 is the only transmembrane protein known to be in the IM, it was initially hypothesised that the phagophoric membrane was exclusively supplied with lipids by Atg9 vesicles (Yamamoto et al., 2012). It is now known that Atg2 mainly mediates the lipid supply to the phagophore (Osawa et al., 2022). While there are clear indications as to what the immediate functions of both Atg9 and Atg2 are in the process of phagophore elongation, it is still unclear how this is being regulated and what role the interplay between the two proteins has in the wider context of phagophore

morphology.

More specifically, it is unknown how the unidirectional lipid transport (LT) from the ER to the phagophore is driven. On the ER side two human lipid scramblases, TMEM41B and VMP1, were found to interact with ATG2A (Ghanbarpour et al., 2021). When deleting TMEM41B and VMP1, autophagic flux is halted (Morita et al., 2018). One hypothesis that could explain unidirectionality of LT is that these scramblases could potentially increase the local concentration of specific lipids in the outer leafler of the ER which would create a gradient driving lipid transport to the IM. Such energetically costly processes usually require some form of free energy, the source of which has not been discovered yet. None of the involved proteins, Atg2, Atg9 or the human ER scramblases VMP1 or TMEM41B require ATP for their activity(Osawa et al., 2022; Li et al., 2021; Valverde et al., 2019; Matoba et al., 2020). Another hypothesis for where the energy for unidirectional LT could be coming from is the long chain fatty acyl-CoA synthetase 1 (Faa1) at the IM (Osawa et al., 2022). Faa1 has been shown to localise to phagophores and to generate acyl-CoA using ATP. The acyl-CoA is channelled to the ER for *de novo* phospholipid synthesis to then be fed into the growing isolation membrane (Schütter et al., 2020). This *de novo* phospholipid synthesis is thought to transiently increase the chemical potential of phospholipids on the ER cytosolic leaflet. This chemical potential could be the driving force for unidirectional lipid transfer to the phagophore where the lipid imbalance across the leaflets is reduced by the activity of Atg9 (Osawa et al., 2022).

This thesis will address the wider role of Atg9 and Atg2 in phagophore morphology beyond their immediate functions of lipid scrambling and lipid transport, respectively. To do so, I have chosen two mutants, one with three point mutations in the lateral pore of scAtg9 (Atg9-basic) and the other with alanine substitutions near the C-terminus of scAtg2 (Atg2-PM4). Both mutants were previously extensively characterised using a variety of methods, which allowed me to focus on the higher-resolution structural characterisation of their

cellular environment during phagophore elongation (Matoba et al., 2020; Gómez-Sánchez et al., 2018).

The above mentioned Atg2-PM4 mutant has alanine substitutions from position 1264 to position 1268 corresponding to the last strand of the predicted β-sheet at the C-terminal region (Fig. 1.10A, blue β-strand) (Gómez-Sánchez et al., 2018). The mutant protein, as well as Atg9 in the presence of the mutant Atg2, were shown to correctly localise to the PAS while the PAS was shown to correctly localise to the vacuole and the ER (Gómez-Sánchez et al., 2018; Hollenstein et al., 2019). However, it was demonstrated with conventional fluorescence microscopy that Atg2-PM4 is distributed across the IM as opposed to localising with Atg9 to the phagophore rims (Gómez-Sánchez et al., 2018). Furthermore, it was biochemically shown that the interaction between Atg9 and Atg2 is disrupted due to the alanine substitutions (Gómez-Sánchez et al., 2018). The ability to tether the ER to the IM was analysed by immunoelectron tomography. These data revealed that Atg2-PM4 had enhanced association of the ER with Ape1 oligomers which is a well established cargo of selective autophagy in yeast (Gómez-Sánchez et al., 2018; Yamasaki et al., 2020). I chose this mutant because it seemed well suited to understand the interplay between Atg9 and Atg2 since the interaction is disrupted while both proteins are functional.

The mutant protein Atg9-basic has the point mutations R560A, Q576A, and R723A, all of which are located in the basic rear region of the lateral pore of the Atg9 protomer (Fig. 1.10B, blue residues on the right side of the panel) (Matoba et al., 2020). It has been shown that this triple mutation causes a reduction in both the number and size of autophagosomes (Matoba et al., 2020) while it still localise to the PAS. Additionally, Matoba et al. (2020) showed that the isolation membrane in a giant Ape mutant was significantly shorter compared to the wild-type. The giant Ape mutant arises from overexpression of Ape1 and leads to the formation of larger Ape1 oligomers that are engulfed by larger phagophores (Suzuki et al., 2013; Gómez-Sánchez et al., 2018). The giant Ape phenotype

can easily be identified with various forms of microscopy and is thus an established assay to study autophagosome formation (Suzuki et al., 2013; Yamasaki et al., 2020). Furthermore, Atg9-basic showed a significant reduction in transferring PI3P from the outer leaflet to the inner leaflet of liposomes (Matoba et al., 2020). I chose this mutant for my study in order to understand in a more nuanced way the wider effect of Atg9 lipid scramblase function in the context of phagophore elongation.

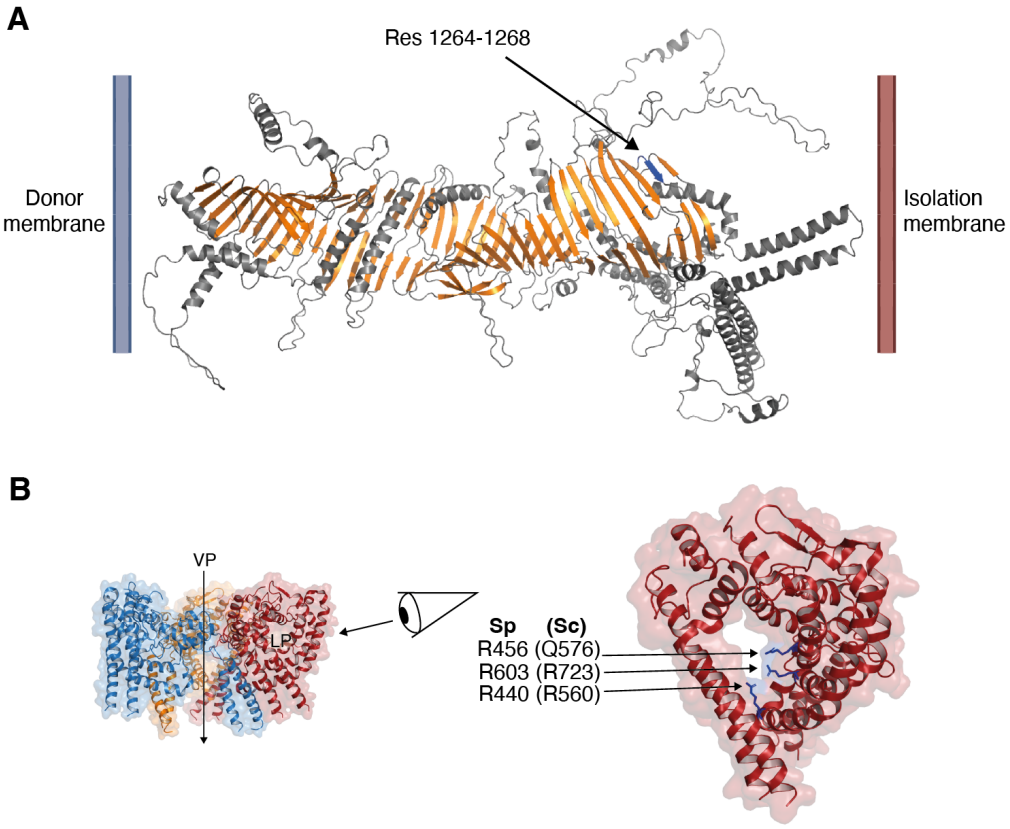

Figure 1.10: Illustration of the mutations in Atg9 and Atg2 used in this thesis. **A**) Cartoon representation of the alphafold model of yeast Atg2 (Uniprot code: P53855) with characteristic β-sheets in orange and the stretch of mutated residues in blue. **B**) Depiction of the atomic model of fission yeast Atg9 (PDB: 7D0I, elucidated by (Matoba et al., 2020)). On the left, an overview of the trimer is shown with the vertical pore (VP) and lateral pore (LP) as well as the direction from which the monomer shown on the right is depicted. The Atg9 monomer on the right has the residues that were mutated highlighted in blue. Both *S. pombe* (Sp) and the *S. cerevisiae* (Sc) residues are listed.

2 Aims

The overall objective of this work was to characterise the biogenesis of autophagic membranes in *S. cerevisiae* with a focus on morphology of phagophores during the elongation step using cryoCLEM and *in situ* cryoET. In order to understand the function of Atg9 and Atg2 in the wider context of phagophore morphology, I set out to pursue the following aims. First, I had to establish a fluorescence tagging strategy for my proteins of interest, Atg9 and Atg2. Second, given the fast progression of autophagy I needed to identify a phenotype to accumulate phagophores in intermediate stages of autophagosome biogenesis using cryo-confocal microscopy.

Third, I aimed to better understand how the Atg9 scramblase function affects phagophore morphology *in situ*. Fourth, I aimed to better understand the role of the Atg9-Atg2 interaction within the process of phagophore elongation. In order to understand how the Atg9 scramblase function as well as the Atg9-Atg2 interaction affect phagophore morphology in molecular detail, I aimed at employing the entire *in situ* cryo-tomography work including quantitative image analysis by membrane segmentation and membrane shape quantification of the generated phenotypes.

3 Results

3.1 Establishing a fluorescent experimental set-up to study scAtg9 and scAtg2 *in situ* under cryogenic conditions

Fluorescence microscopy is a standard technique in the field of cellular and molecular biology. However, using this technique with samples kept at cryogenic temperatures has been a more recent development (Schwartz et al., 2007; Sartori et al., 2007). As outlined in section 1.2 fluorophores behave slightly differently under cryogenic conditions; namely a lack of detectable photobleaching, a shift or narrowing of absorption and emission spectra, altered photo-switching behaviour, prolonged triplet states which lead to reduced brightness and consequently a reduced signal-to-noise ratio (Moerner and Orrit, 1999; König et al., 2014; Metskas and Briggs, 2019). The following section outlines the experiments conducted in order to set up and optimise a suitable system to visualise Atg9 and Atg2 in *S. cerevisiae* (in the following sections referred to as yeast) under cryogenic conditions.

TABLE 3.1: **Fluorophores and channels screened for suitability in this yeast cryoCLEM study as well as laser lines and detection ranges available in the microscopic set-up.**

Available excitation laser (nm)	Detection range (nm)	Tag name	Excitation peak (nm)	Emission peak (nm)	Reference
405	450-514	mTagBFP2	399	454	Subach et al. (2011a)
488	495-556	EGFP	488	507	Cormack et al. (1996)
		mNeon	506	517	Shaner et al. (2013)
488	510-566	EYFP	513	527	Ormö et al. (1996)
561	572-650	mScarlet	569	594	Bindels et al. (2017)
		PSmOrange (far-red)	636	662	Subach et al. (2011b)

3.1.1 Testing different Tags under cryogenic conditions *in situ*

When tagging two proteins in the same sample, one needs to minimise the overlap of emission from one fluorophore with the excitation of the other to avoid so-called bleed-through fluorescence. Based on the known fluorescence spectra the following tag pairs would be appropriate; mTagBFP2 with mScarlet (Fig. 3.1A) or EGFP with PSmOrange (switched to far-red) (Fig. 3.1A). As concluded from the channel screen (section 3.1.2) the blue and red region of the spectrum would be the more suitable choice for tags. As both proteins of interest are very low in abundance in the cell, the following triple tags were tested; 3xmTagBFP2, 3xEGFP, 3xmScarlet, 3xPSmOrange (far-red). The tags mTagBFP2 and PSmOrange are less common fluorescent protein variants but mTagBFP2 was readily available and tested for expression in yeast by a collaborator (see Table A.2) as well as matching well with the excitation laser available in our cryo-confocal set-up. PSmOrange is a photoswitchable variant that undergoes a covalent modification upon exposure to a pulse of blue light (489 nm) (Pletnev et al., 2014). After photoswitching, PSmOrange is fluorescent in the far-red region of the spectrum (Subach et al., 2011b), which is the varient of the protein useful in this experimental set-up. Photoswitching is often not efficiently possible under cryogenic conditions and depends on the exact tag and its switching mechanism. However, since photoswitching of PSmOrange is irreversible, the switch can be carried out before vitrification of the cells. Therefore, PSmOrange is a functional candidate in this channel screen.

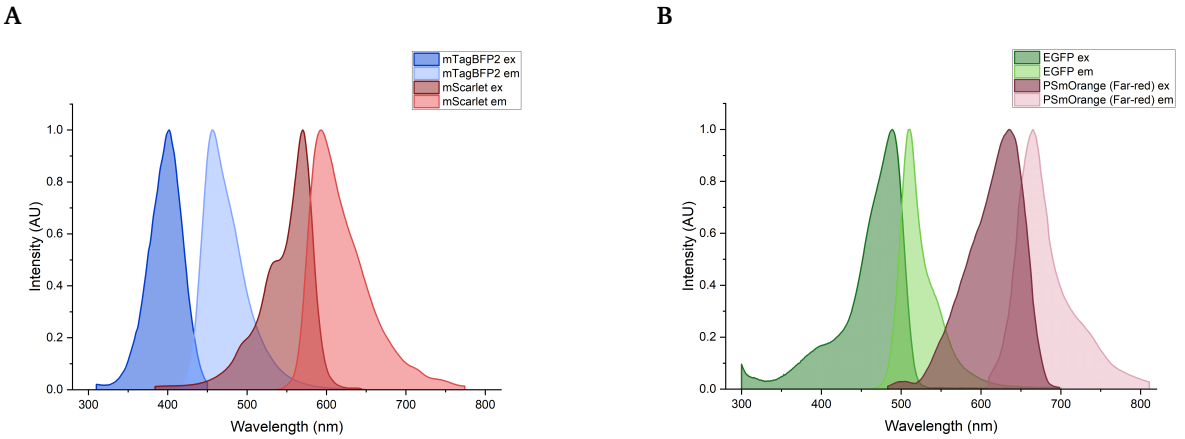

Figure 3.1: Spectra of tested fluorophores grouped in suitable pairs. **A**) Emission and excitation curves mTagBFP2 and mScarlet. **B**) Emission and excitation curves EGFP and PSmOrange. Spectra were obtained from FPbase (Lambert, 2019) and plotted in Origin(Pro) 2023.

3.1.1.1 Atg9 tags

In order to determine the most suitable fluorescent tag for Atg9 four different tags were tested, 3xEGFP, 3xmScarlet, 3xmTagBFP2 and 3xPSmOrange . Constructs with triple tagged Atg9 under the control of its native promoter were generated based on the parent plasmid termed pCK785 generously provided by Prof. Dr. Claudine Kraft (Table A.2). This plasmid carries a triple EGFP tag and the native promoter of Atg9. The triple EGFP tag was replaced with the other tags. Linkers between Atg9 and the fluorescent proteins from this construct were designed to be the same in the 3xmScarlet, 3xmTagBFP2 and 3xPSmOrange constructs. A comprehensive list of constructs can be found in Table A.2.

Initial tests of the constructs were done in cells that only had an atg9 knock out (referred to as yCK414, Tab. A.1). There are no significant peaks that could be attributed to the triple tagged EGFP in comparison with the WT images (Fig. 3.2). Surface plots showing the intensity plotted across the area of a representative cell (marked in microscopy images by yellow ellipse)

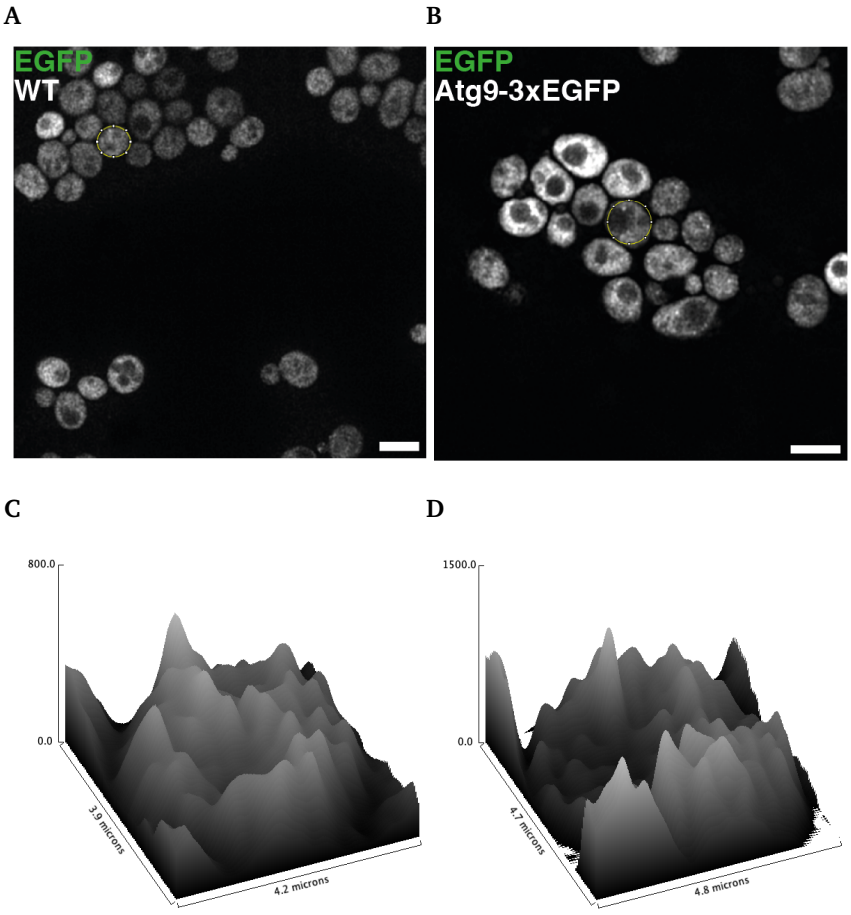

Figure 3.2: Confocal microscopy images of **A**) WT yeast and **B**) yCK414 pCK785 (BY4741 Δ atg9 Atg9-3xEGFP). Each image represents a single slice from the centre of the cell cluster. Intensity values could not be scaled to the same range as the Atg9-3xEGFP sample was imaged with 4.5 % and the WT with 5 % laser power and the focal depth differed with 370 nm for WT and 420 nm for Atg9-3xEGFP. **C**) and **D**) Surface plots of a representative cell each marked by a yellow ellipse in panels **A**) and **B**) respectively. Scale bars 5 µm.

illustrate the typical peaks seen in the WT control and the yCK414 Atg9-3xEGFP sample and how they relate in intensity to the cellular background (Fig. 3.2C and Fig. 3.2D respectively). Similarly, for the triple mTagBFP2 (Fig. 3.3), the triple mScarlet (Fig. 3.4) and the triple PSmOrange (Figure 3.5) tag on Atg9, no fluorescent peaks could be identified.

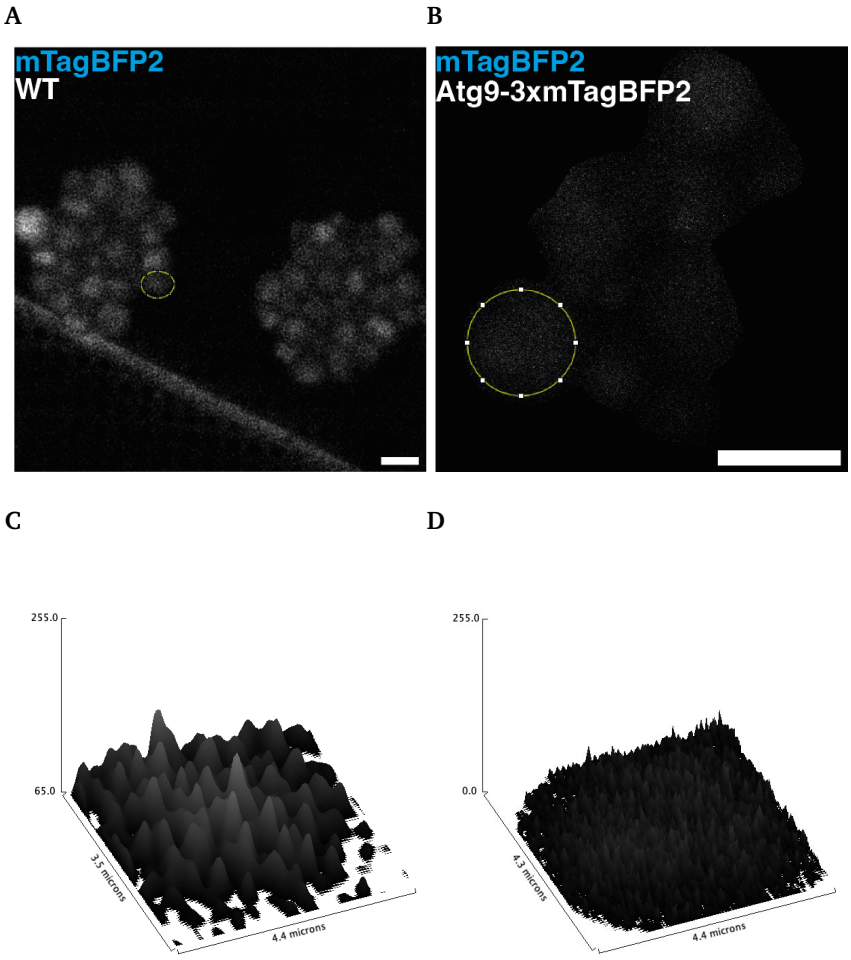

Figure 3.3: Confocal microscopy images of **A**) WT yeast and **B**) yCK414 transformed with pCO112 (BY4741 Δatg9, Atg9-3xmTagBFP2 on plasmid). Each image shows a single slice from a representative cell (focal depth 250 nm for WT and 550 nm for mTagBFP2 sample). **C**) and **D**) Surface plots of a representative cell each marked by a yellow ellipse in panels **A**) and **B**), respectively. Scale bars 5 µm.

In Figures 3.3B, 3.5A, and 3.5B) cells are not readily recognisable, regions were identified by imaging in the EGFP or the fiducial channel (not shown) as these show the cytosol or are excluded from the cellular volume, respectively. For best comparison, acquisition parameters were kept consistent (except z-thickness when not possible) across the different samples and a representative slice of each z-stack is shown.

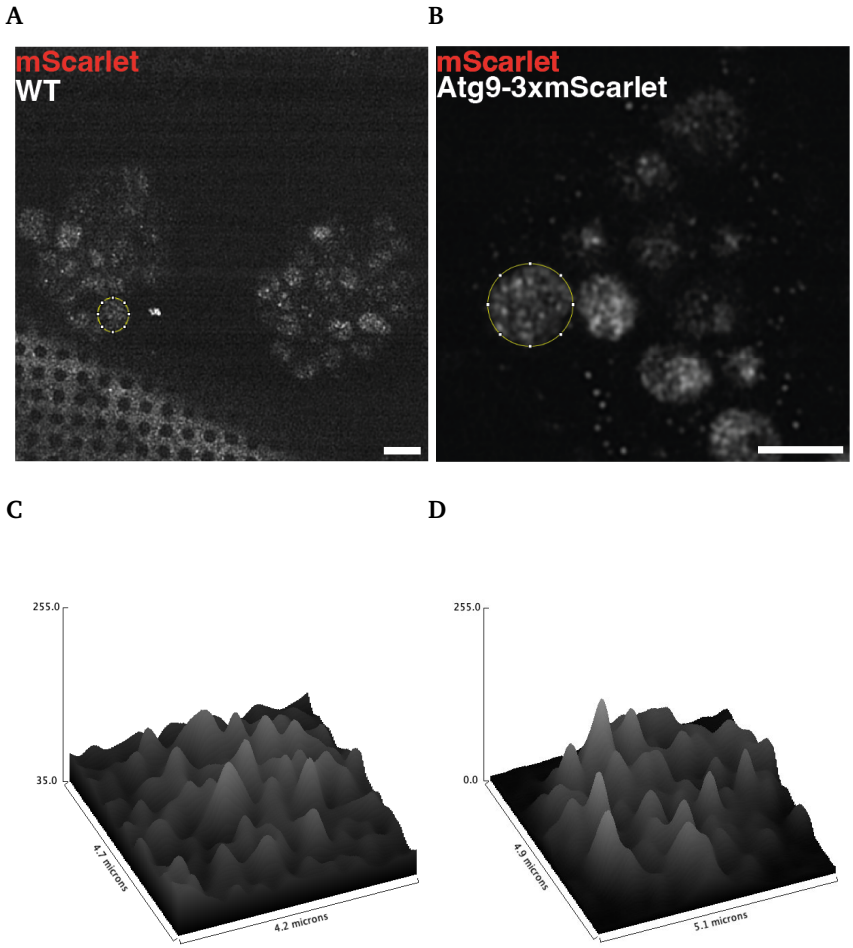

Figure 3.4: Confocal microscopy images of **A**) WT yeast and **B**) yCK414 transformed with pCO111 (BY4741 Δatg9, Atg9-3xmScarlet on plasmid). Each image shows a single slice from a representative cell (focal depth 250 nm for WT and 220 nm for yCK414 Atg9-3xmScarlet). **C**) and **D**) Surface plots of a representative cell each marked by a yellow ellipse in panels **A**) and **B**), respectively. Scale bars 5 μm.

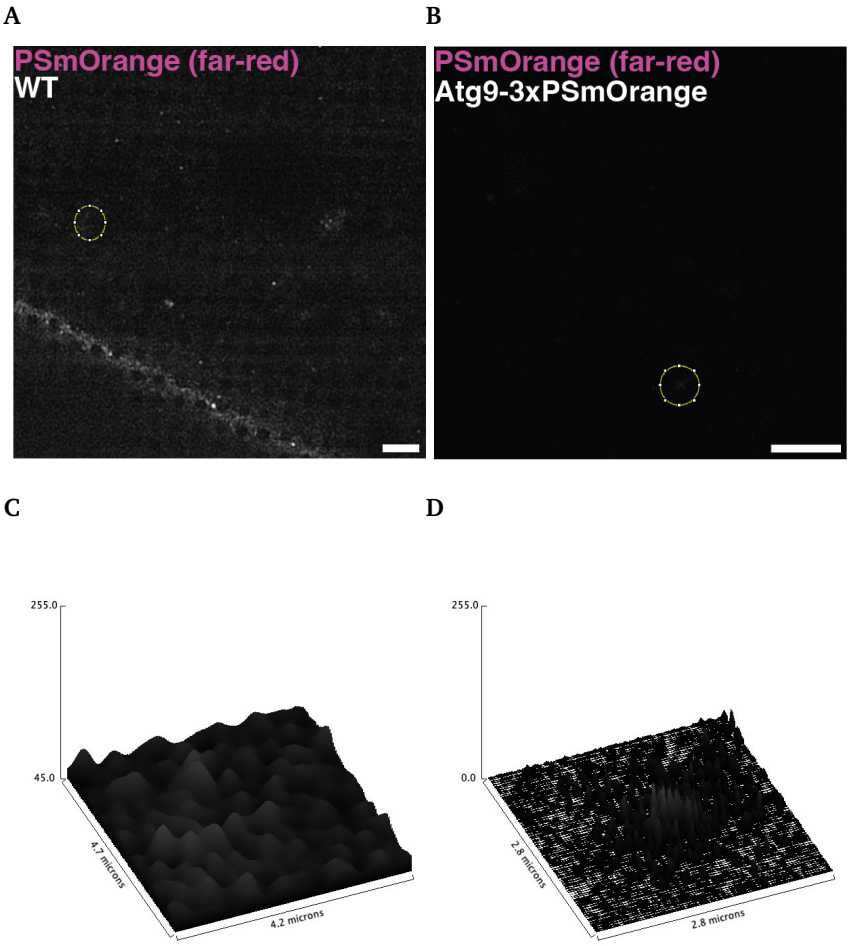

Figure 3.5: Confocal microscopy images of **A**) WT yeast and **B**) yCK414 transformed with pCO110 (BY4741 Δatg9, Atg9-3xPSmOrange on plasmid). Each image shows a single slice from a representative cell (focal depth 250 nm for WT and 530 nm for yCK414 Atg9-3xPSmOrange). **C**) and **D**) Surface plots of a representative cell each marked by a yellow ellipse in panels **A**) and **B**), respectively. Scale bars 5 μm.

In light of the inability to detect Atg9 unambiguously without an accumulating mutation (see section 3.2) the same constructs were tested in a Δatg2 Δatg9 background (yDP13, Table A.1). In the absence of Atg2, Atg9 will accumulate at the PAS (Reggiori et al., 2004; Gómez-Sánchez et al., 2018). Likewise for the yDP13 samples, individual representative z-stack slices as well as surface plots of single representative cells were used to compare the different tags (Fig. 3.6). While the EGFP sample has high overall intensity, a single relevant peak could not be identified. Similarly, the PSmOrange sample showed very broad and low intensity without any clear peaks relative to the background. In contrast, the mScarlet and the mTagBFP2 sample had distinguishable peaks relative to the background signal. Since the cellular background signal in the mTagBFP2 sample appeared more homogeneous compared to the red and far-red spectral region, making it easier to distinguish peaks, I decided to use the Atg9 construct with 3xmTagBFP2 tag. Consequently, the Atg9 construct with 3xmTagBFP2 tag was used in all subsequent experiments as the difference between background and peak was most easily distinguishable.

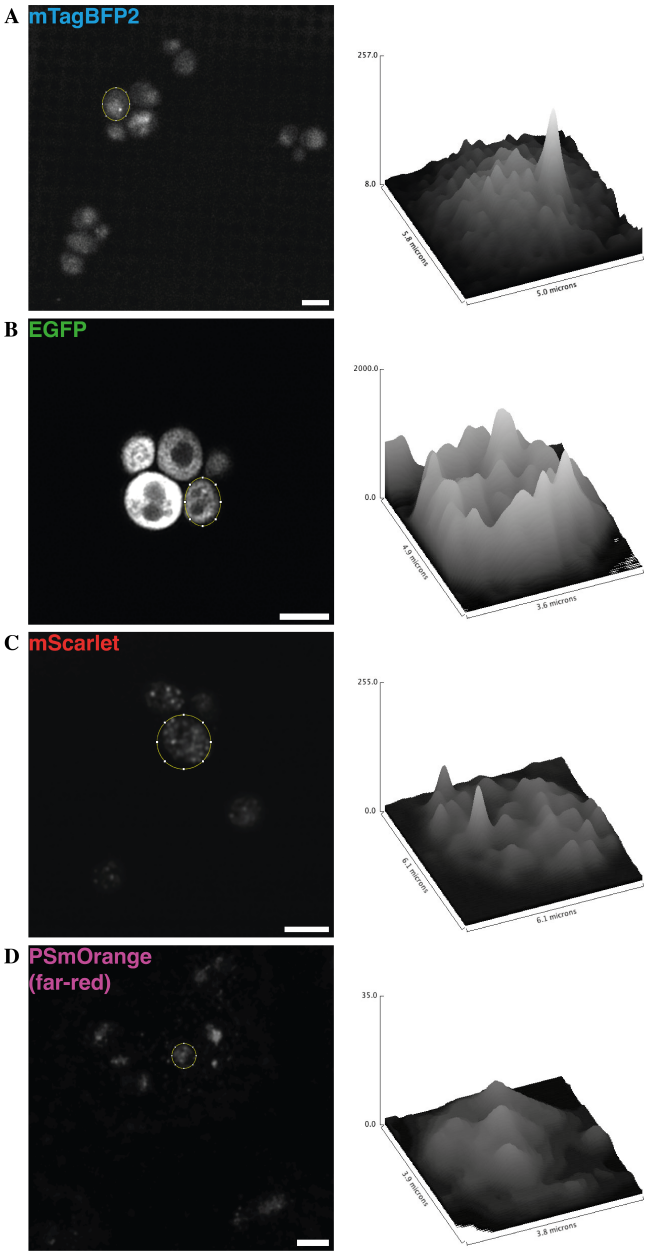

Figure 3.6: Confocal microscopy images of yDP13 (BY4741 Δatg2 Δatg9) transformed with **A**) pCO112 (Atg9-3xmTagBFP2), **B**) pCK785 (Atg9-3xEGFP), **C**) pCO111 (Atg9-3xmScarlet), **D**) pCO110 (Atg9-3xPSmOrange). Images on the left show single slices from z-stacks with a representative region of a cell (focal depth 220 - 250 nm). On the right are shown corresponding surface plots of a representative cell, marked by yellow ellipses from microscopy image next to it. Scale bars 5 μm.

3.1.1.2 Atg2

In order to identify the most suitable fluorescent tag for Atg2 compatible with the chosen Atg9 tag mTagBFP2, two tags were tested; 3xmScarlet and PSmOrange. Constructs with triple tagged Atg2 under control of its native promoter were generated based on the plasmid pDP70 generated by our collaborator Prof. Dr. Claudine Kraft (Table A.2). This plasmid already carried a triple mCherry tag and the native Atg2 promoter. The 3xmCherry tag was replaced with 3xmScarlet and 3xPSmOrange tags. Similarly as with Atg9, a preliminary test showed that the detection of Atg2 without an accumulating mutation (see section 3.2) was not possible (Fig. 3.7). A cell can only be identified in the absence of signal of interest, in this case by fiducials depositing around the cell (yellow circle in Fig. 3.7A).

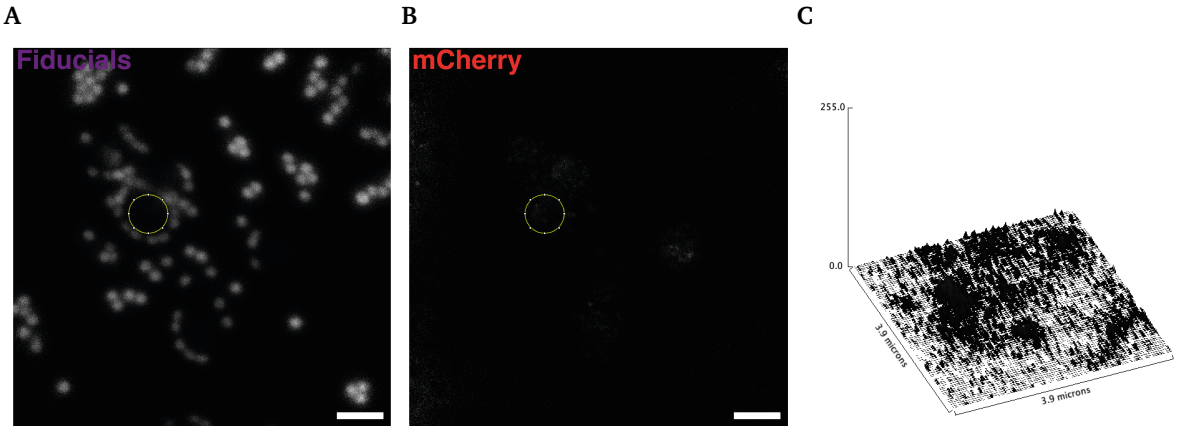

Figure 3.7: A) Confocal microscopy image of yCK761 pDP70 (BY4741 Δatg2, Atg2-3xmCherry on plasmid) in fiducial channel (Carboxylate-modified microspheres, ex. 625 nm/ em. 645 nm). Image shows a single slice from a z-stack with representative region of a cell (focal depth 590 nm). **B**) The same region of the sample in mCherry channel. **C**) Surface plot in mCherry channel of a representative cell marked by yellow ellipses in panels **A**) and **B**). Scale bars 5 µm.

Therefore, the Atg2 triple tag constructs were tested in a Δatg1 Atg9-3xEGFP background (ySB4, Table A.1), which is still carrying the native atg2 gene. In the absence of Atg1, the early PAS cannot fully form (Suzuki et al., 2001). This means Atg9 will localise at the PAS but retrograde cycling of Atg9 is disabled (Suzuki et al., 2001; Reggiori et al., 2004; Suzuki et al., 2007). Atg2 will also localise to the PAS and be trapped there together with Atg9 (Gómez-Sánchez et al., 2018). Since the decision over the tag for Atg9 had been made already, only two options remained as tags for Atg2; 3xmScarlet and 3xPSmOrange. Following the single punctum in the EGFP channel showing Atg9, we can assume that Atg2 will co-localise (Fig. 3.8). However, there is no marked difference in intensity between the non-transformed control and the samples carrying the Atg2-3xmScarlet construct. Moreover, the PSmOrange construct did not show any punctae either, as visualised in the confocal microscopy image and the surface plot (Fig. 3.9). While there is a mixed population of tagged and untagged protein in the cell, the majority of both species is expected localise to the halted PAS. Therefore, the lack of signal with both tags was attributed to the overall low native copy number of Atg2. This in line with our collaborators' observation that the detection of Atg2 is challenging in conventional live cell imaging as well (personal communication, Mariya Licheva). Since both constructs looked equivalent in fluorescence microscopy and PSmOrange requires an extra photoswitching step before vitrification I decided to conduct subsequent experiments with the Atg2-3xmScarlet construct.

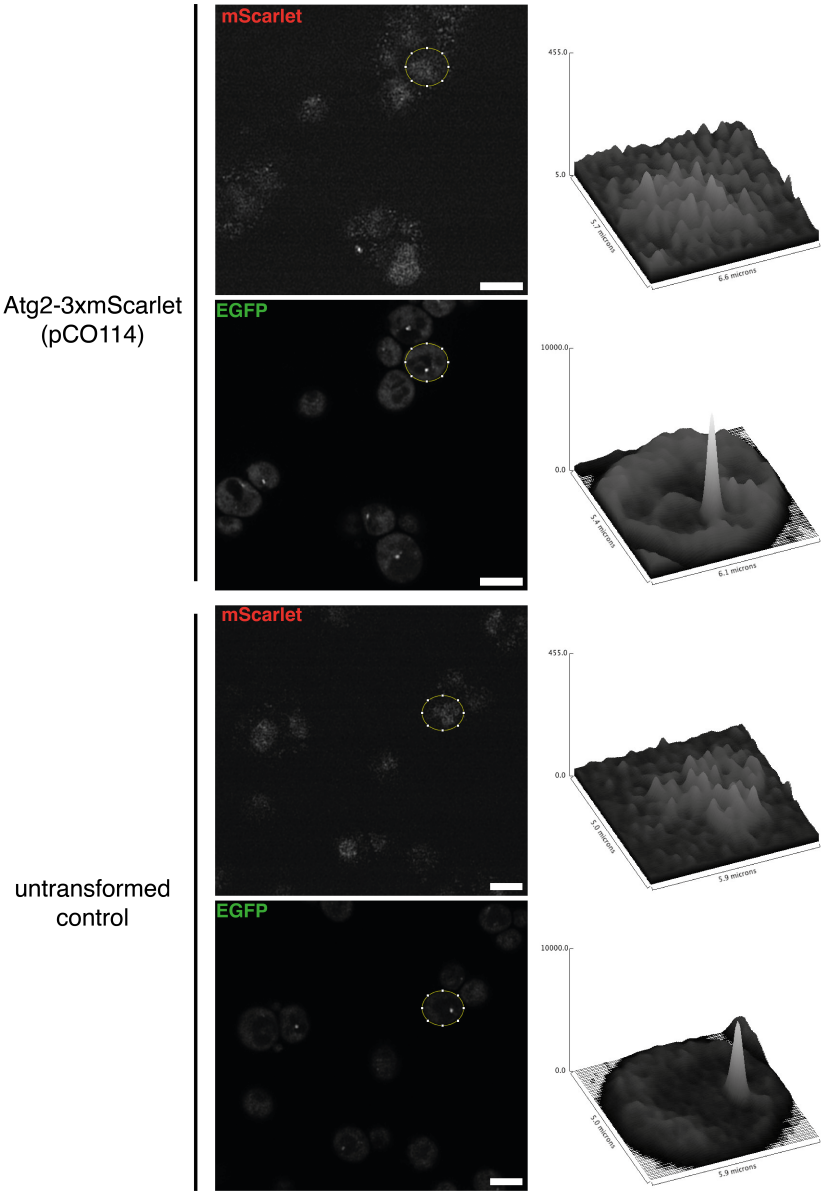

Figure 3.8: Confocal microscopy image of ySB4 untransformed (bottom) and ySB4 transformed with pCO114 (BY4741 Δatg1, Atg9-3xEGFP, Atg2-3xmScarlet on plasmid, top) in the mScarlet channel in the EGFP channel. Each image shows a single slice from a z-stack with a representative region of cells (focal depth 250 nm for ySB4 pCO114 and 220 nm for ySB4 untransformed). On the right of each microscopy image are shown surface plots of a representative cell (marked by yellow ellipse in respective microscopy image). Scale bars 5 µm.

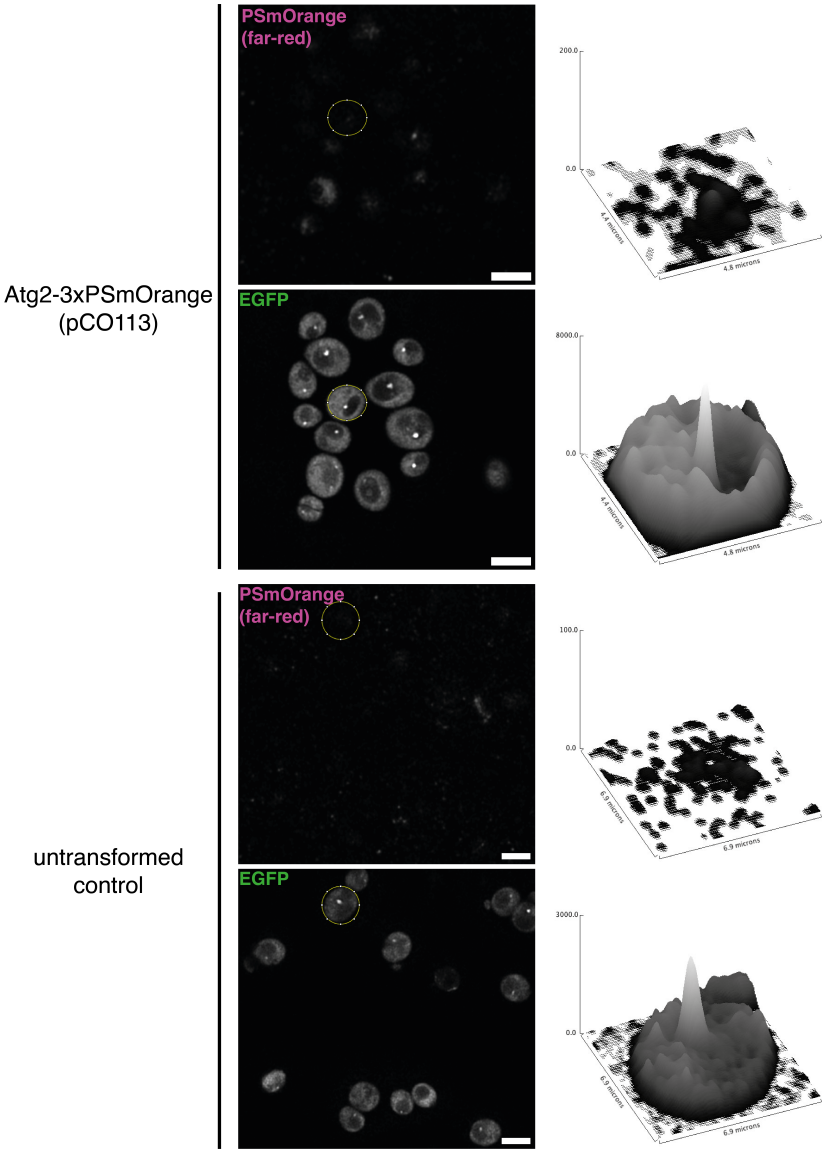

Figure 3.9: Confocal microscopy images of ySB4 untransformed (bottom) and ySB4 transformed with pCO113 (BY4741 Δatg1, Atg9-3xEGFP, Atg2-3xPSmOrange on plasmid, top) in the PSmOrange channel and in the EGFP channel. Each image shows a single slice from a z-stack with a representative region of cells (focal depth 250 nm for both). On the right of each microscopy image are shown surface plots of a representative cell (marked by yellow ellipse in respective microscopy image). Scale bars 5 μm.

3.1.2 Autofluorescence in *Saccharomyces cerevisiae* under cryogenic conditions

As previously shown by Carter et al. (2018), autofluorescence in cryogenic fluorescence microscopy (cryoFM) appears to vary between cell types and across different wavelengths. Autofluorescence originates from an abundance of biomolecules with conjugated bond systems in cells and is a problem when imaging fluorescent proteins due to the relatively low brightness exhibited by these probes (see section 1.2.2). Therefore the autofluorescence in vitrified wild-type yeast lacking fluorescent probes was assessed across four different channels according to availability of laser lines in the microscope and possible tags tested prior by collaborators for fusion protein stability (see table 3.1). Images from the four channels were acquired under the same conditions, as far as technically possible, meaning excitation laser strength, scanning mode and z-thickness were kept constant. In Figure 3.10, individual slices of z-stacks from vitrified wild-type cells in the different channels are shown. The autofluorescence signal in green (Fig. 3.10A) stands out as the brightest peaking at 2389 (arbitrary units, AU). Interestingly, large central regions of the cell, most likely the nucleus or the vacuole exclude this signal. While in the mCherry channel (Fig. 3.10B) punctae are visible with a maximum of 129 AU, they are overall approximately 18-fold lower in intensity, than in the EGFP channel and appear to originate at least in part from the media surrounding the cells. In both the BFP and YFP channels the signal is so low, that it could not be seen when scaled the same as EGFP and mCherry. Therefore, the intensity ranges of panels 3.10C and 3.10D are scaled differently from panels 3.10A and 3.10B. While there is still no signal visible in the BFP channel, the signal in the YFP channel appears quite similar to the one in the EFGP channel. Based on this data, EGFP and YFP exhibit a high autofluorescence in vitrified yeast cells and, therefore, fluorescent tags like BFP and mCherry are preferred due to the x-fold lower autofluorescence signal.

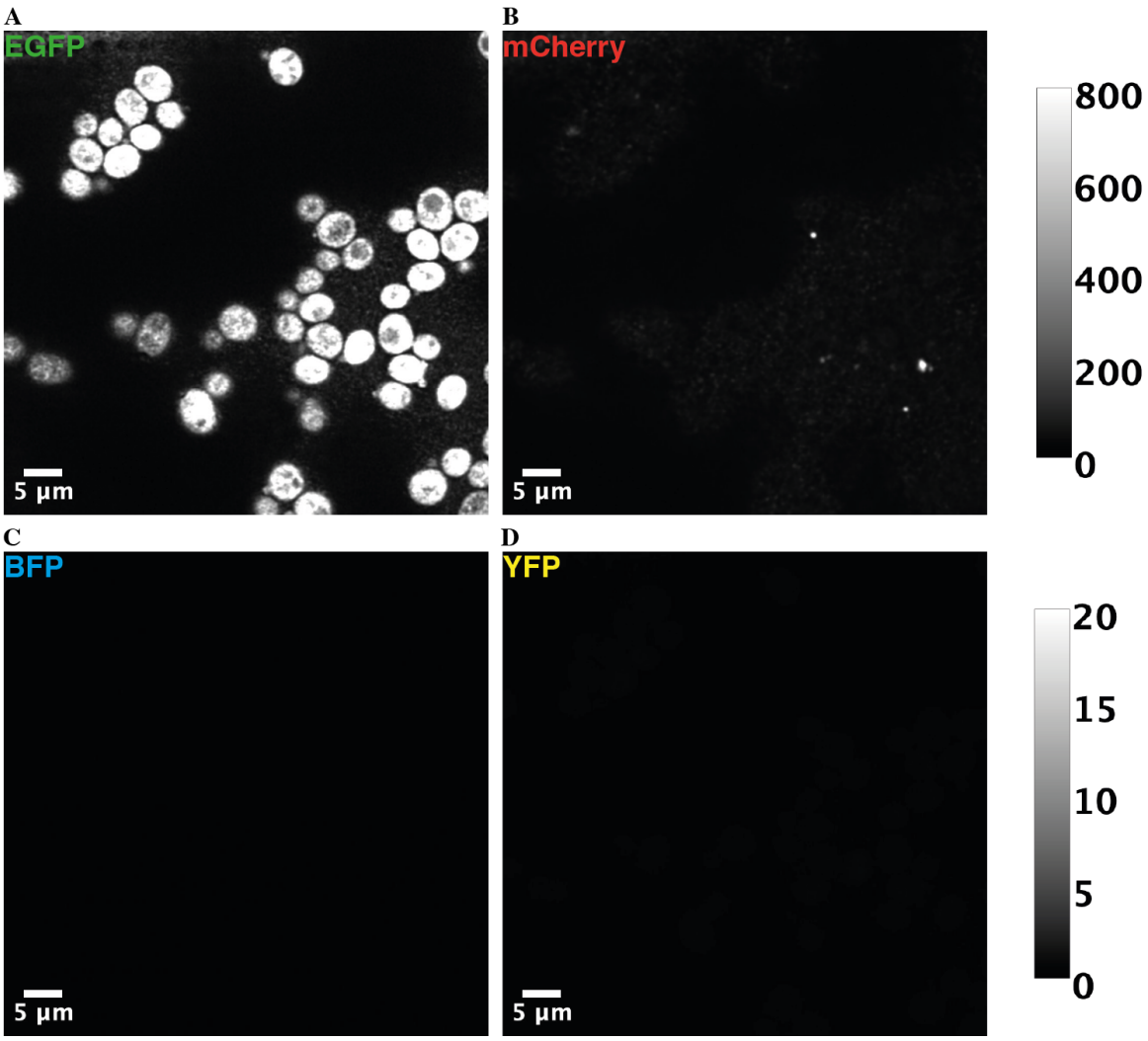

Figure 3.10: Confocal microscopy images of BY4741 (WT) yeast in four different channels; **A**) EGFP, **B**) mCherry/mScarlet, **C**) BFP, **D**) YFP. Each image represents a single slice from the centre of the cell (focal depth 370 nm). Panel **A**) and **A**) were scaled to the same intensity range (0 to 800). Panel **C**) and **D**) were scaled to a smaller intensity range (0 to 20) due to low overall intensity.

Autophagy is a response to cellular stress which also causes the accumulation of structures that were described to be a source of autofluorescence by Carter et al. (2018). As this work set out to investigate autophagy in a native setting, potential changes in the appearance of the autofluorescence upon autophagy induction was verified. To do so, cells were supplemented with 250 nM rapamycin and incubated for 30 and 60 minutes before vitrification. Representative slices of z-stacks were chosen as means of comparison to minimise the effect of different cell and ice thicknesses across samples. As previously shown, autofluorescence was most easily detected in green, hence data was collected in green. No notable difference in granularity or intensity can be observed between the control (Fig. 3.11A), 30 minutes (Fig. 3.11B) and 60 minutes (Fig. 3.11C) rapamycin incubation. Therefore, autofluorescence in green does not appear to be changed to a relevant extent in our experimental setting by induction of autophagy and the cellular changes ensued.

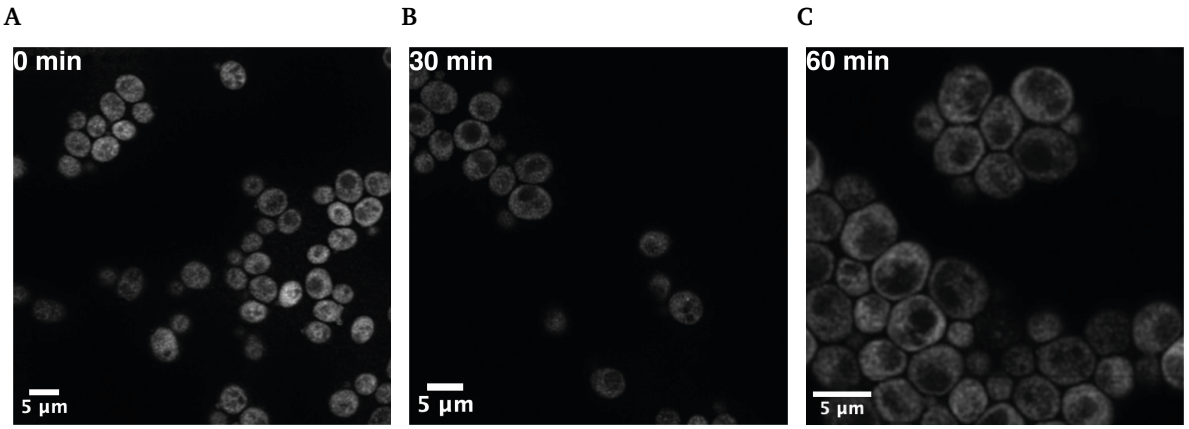

Figure 3.11: Confocal microscopy images of WT yeast in the EGFP channel, **A**) without rapamycin treatment, **B**) with 30 min rapamycin treatment, and **C**) with one hour rapamycin treatment. Each image represents a single slice from the centre of the cell cluster (focal depth 370 nm). All images were scaled to the same intensity range (0 to 3000).

3.2 Identifying suitable genetic mutations to accumulate phagophore structures *in situ*

Owing to systematic genetic dissection of the core autophagy machinery, it is known in which sequence autophagy factors localise to the PAS and are required for the progression of autophagosome biogenesis (Tsukada and Ohsumi, 1993; Suzuki et al., 2001, 2007). This section describes the screening of a variety of mutants known to accumulate different autophagosomal intermediates by halting the autophagosome biogenesis process. The studied mutants can be divided into three categories based on the stage in which autophagy is halted; early PAS, unsealed phagophores, and fully sealed unfusable autophagosomes (Fig. 3.12).

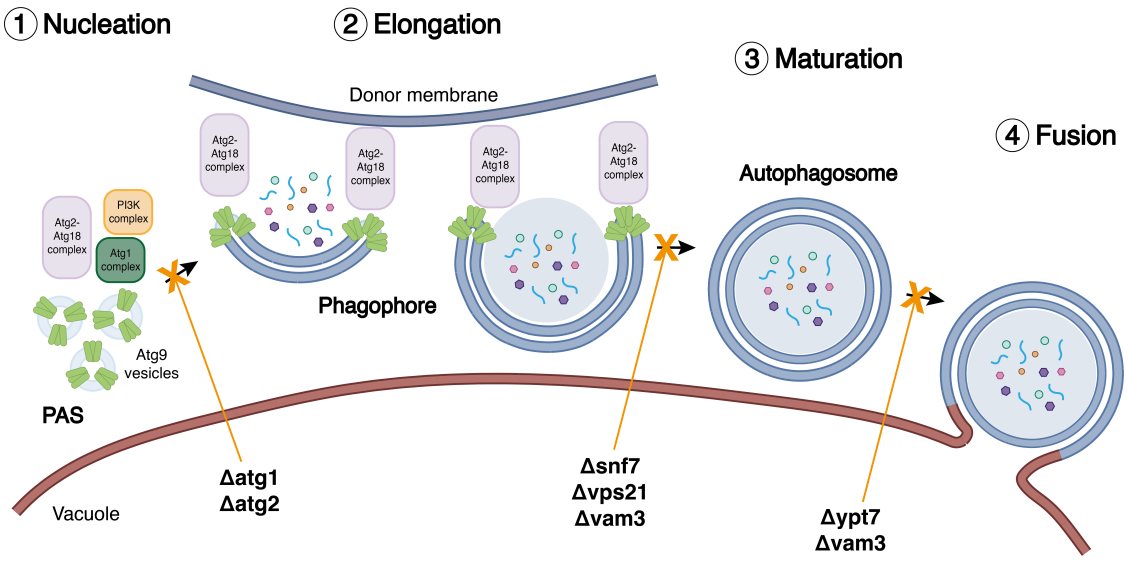

Figure 3.12: Schematic representation of macroautophagy illustrating which mutations halt the autophagosome biogenesis process at which step.

As detailed in section 3.1.1.1, Atg9 and Atg2 could not be unambiguously detected in a WT strain. To enhance the likelihood of detection this selective autophagy was disabled with a Δatg19 mutation (Fig. 3.13), though without a marked difference. In such a condition, only macroautophagy processes would remain active, which could lead to increased to punctae. However, the EGFP signal was still diffuse, with no clear punctae visible. To visualise the vacuolar membranes, the dye FM4-64 was utilised.

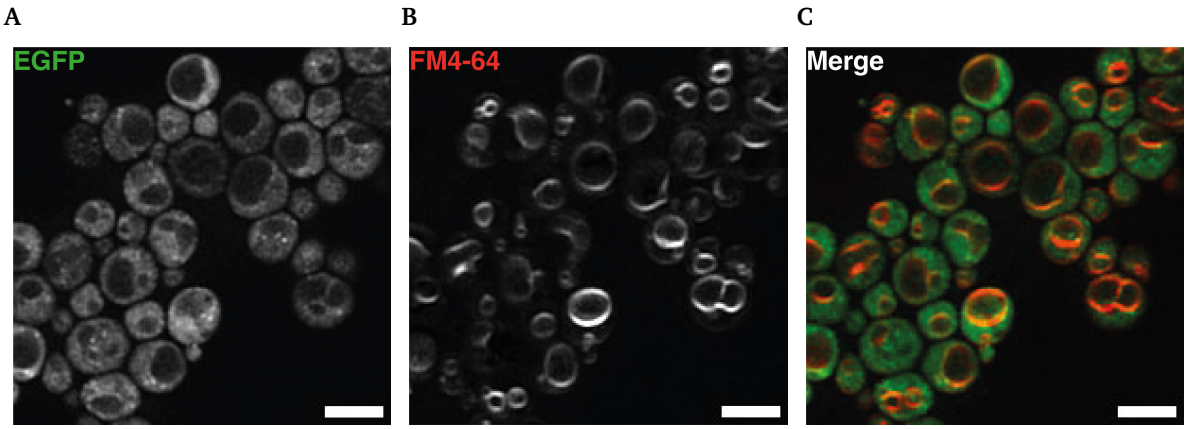

Figure 3.13: Confocal microscopy images of yDP652 (Atg9-3xEGFP Δatg19) **A**) in the EGFP channel, **B**) in the FM4-64 channel, and **C**) merge of the two channels, EGFP in green and FM4-64 in red. All images are a slice of a z-stack (focal depth 220nm). Scale bars 5 μm.

3.2.1 Early △ PAS mutant

For comparison an early PAS mutant, Δatg1 was tested (Fig. 3.14). In the absence of Atg1, autophagy is halted at its earliest stage since the Atg1 complex is required to recruit other downstream autophagy proteins (Suzuki et al., 2007; Hollenstein and Kraft, 2020). However, Atg9 vesicles still localise to the PAS and do not get recycled (Reggiori et al., 2004; Mari et al., 2010). The Δatg1 mutant has the advantage that many more Atg9 vesicles can accumulate compared to physiological conditions at a single early PAS (Fig. 3.14A), located at the vacuole (Fig. 3.14B). Consequently, this mutant provides a single structure per cell with more fluorophores which makes it easier to detect. However, the structure accumulated in this mutant is not a phagophore in the process of elongation and thus unfortunately outside of the scope of this study.

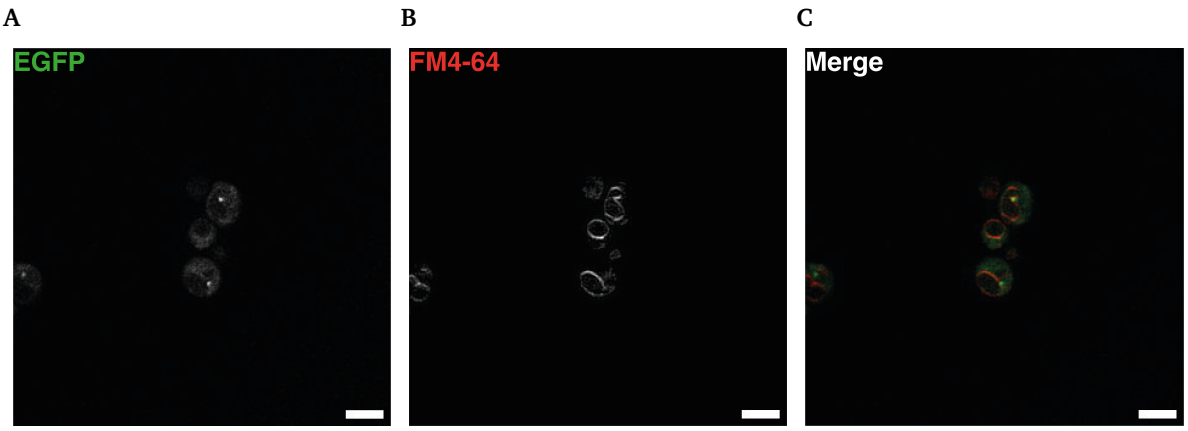

Figure 3.14: Confocal microscopy images of ySB4 (Atg9-3xEGFP Δatg1) **A**) in the EGFP channel, **B**) in the FM4-64 channel, and **C**) merge of the two channels, EGFP in green and FM4-64 in red. All images are a slice of a z-stack (focal depth 630 nm). Scale bars 5 µm.

3.2.2 Unsealed phagophore mutants

Two mutants were studied that both are deficient in sealing of the isolation membrane to form a fully closed autophagosome. The first mutant is deficient in Vps21. Vps21 is a known Rab5-GTPase in the endosomal pathway which was shown to be responsible for initiating phagophore closure by recruitment of ESCRT III components (Chen et al., 2014; Zhou et al., 2017, 2019). Among those ESCRT III proteins is Snf7, the other protein whose deletion was studied here as a second mutant. Snf7 was shown to also be involved in autophagosome sealing (Zhou et al., 2019). Deletion of either Vps21 or Snf7 leads to impairment of autophagic processing of cargo and to an accumulation of unsealed autophagosomes outside the vacuole (Zhou et al., 2017, 2019).

Accordingly, the accumulation of Atg9-positive structures adjacent to the vacuole can be seen in our set-up in both the Δvps21 mutant (Fig. 3.15 and A.1, white arrows) and the Δsnf7 mutant (Fig. 3.16, white arrows). While not all cells to appear to have punctae in the presented z-slice, the Atg9-positive structures can be found throughout the cell volume. Cells with a very strong signal for the membrane stain FM4-64 (Fig. 3.16B, orange arrows) are most likely apoptotic, as was confirmed by cryoEM (data not shown). These cells can be disregarded since this is most likely a result of extensive starvation before vitrification. Both mutants seem to be equally suitable considering both show numerous punctae distinguishable from the background across the cells.

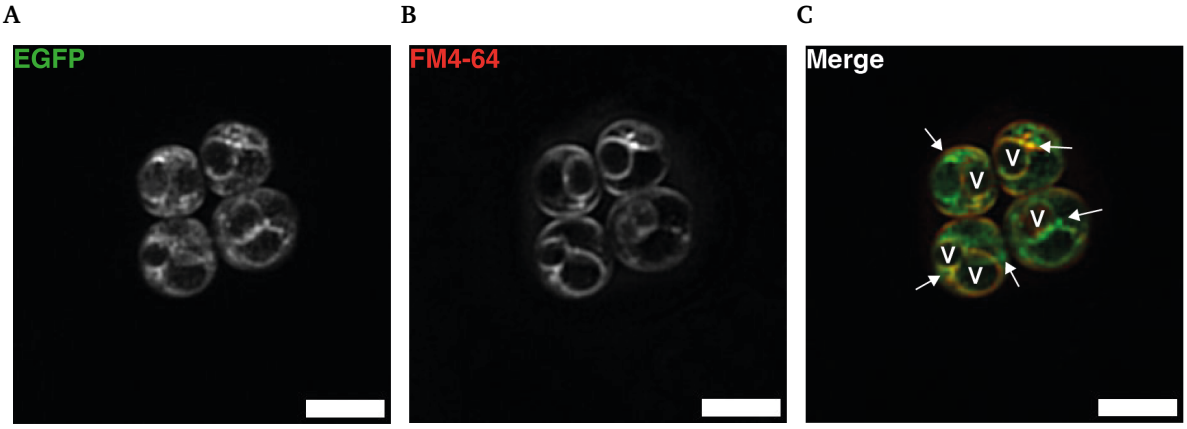

Figure 3.15: Confocal microscopy images of yML63 (Atg9-3xEGFP Δvps21). **A**) EGFP channel, **B**) FM4-64 channel, and **C**) Merge of the two channels, EGFP in green and FM4-64 in red. Vacuoles are marked with **V** and the white arrows points at Atg9 punctae. All images are a slice of a z-stack (focal depth 420 nm). Scale bars 5 μm.

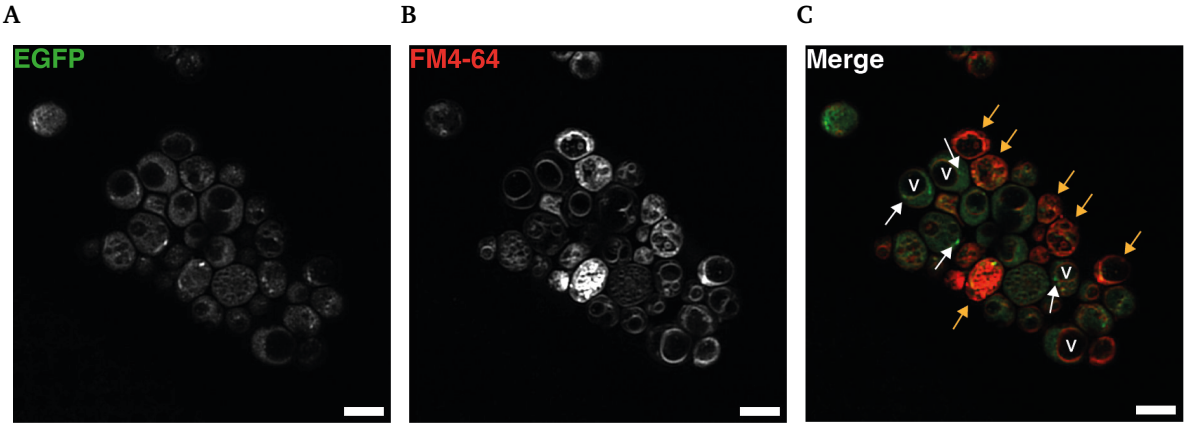

Figure 3.16: Confocal microscopy images of yML65 (Atg9-3xEGFP Δsnf7). **A**) EGFP channel, **B**) FM4-64 channel, and **C**) Merge of the two channels, EGFP in green and FM4-64 in red. Vacuole are marked with **V**, Atg9 punctae pointed out by white arrows, orange arrows point out likely apoptotic cells. Images were recorded with a focal depth of approx. 250 nm. Scale bars 5 μm.

3.2.3 Unfused autophagosome mutants

Ypt7 is a Rab-GTPase recruited to and activated at autophagosomal and vacuolar membranes (Gao et al., 2018; Kriegenburg et al., 2019). It facilitates the fusion of autophagosomes with the vacuole. It was shown that in the absence of Ypt7 autophagosomes accumulate in the cytoplasm and do not fuse with the vacuole (Kirisako et al., 1999). This has made this mutant extremely widely used in autophagy research. In contrast to Δsnf7 and Δvps21 mutants it was demonstrated that in Δypt7 mutants the autophagosomal cargo is protected from degradation (Kirisako et al., 1999; Zhou et al., 2017). In the cryoFM set-up the Δypt7 mutant showed numerous Atg9-positive punctae adjacent to vacuolar membranes (Fig. 3.17) similar to the unsealed phagophore mutants.

Vam3 is a vacuolar t-SNARE required for all membrane trafficking into the vacuole. Deletion of vam3 prevents the fusion of autophagosomes with the vacuole (Darsow et al., 1997; Sato et al., 2000). In this mutant as well, multiple Atg9-positive punctae are visible and adjacent to vacuolar membranes (Fig. 3.18). In both Δypt7 and Δ vam3 the fragmented vacuole phenotype is prominent (Fig. 3.17B and Fig. 3.18B, respectively) as can be seen by the numerous punctae stained with FM4-64 dye. There is a higher number of smaller vacuolar membranes rather than fewer larger vacuoles (for instance in Fig. 3.14).
Both the unsealed phagophore mutants and the sealed unfused autophagosome mutants are qualitatively equally suitable for this study from an accumulation and detection standpoint. The Δsnf7 variant was chosen as a genetic mutation to study the Atg9-Atg2-Atg18 complex on the grounds that this mutation halts the autophagic process after completion of elongation but before sealing into an autophagosome. This increases the probability of imaging phagophore rims with the complex of interest active in IM elongation.

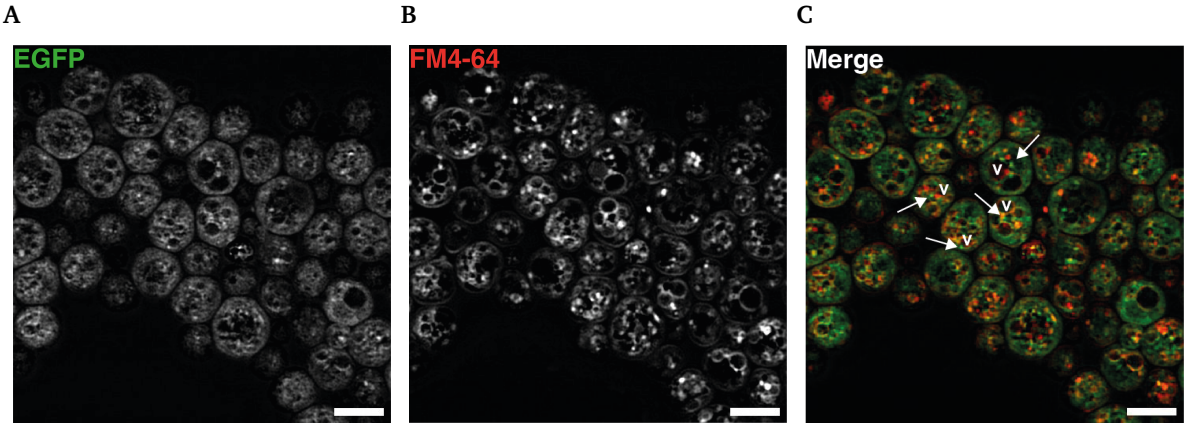

Figure 3.17: Confocal microscopy images of yML61 (Atg9-3xEGFP Δypt7). **A**) in the EGFP channel, **B**) in the FM4-64 channel, and **C**) the merge of the two channels, EGFP in green and FM4-64 in red. Vacuoles are indicated by a **V**, white arrows point at Atg9 punctae. All images are a slice of a z-stack (focal depth 220nm). Scale bars 5 µm.

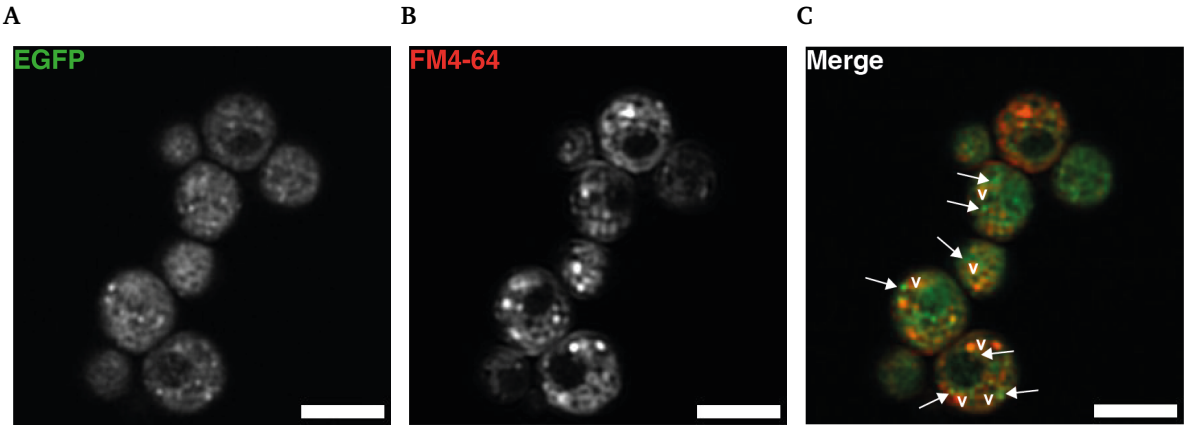

Figure 3.18: Confocal microscopy images of yDP707 (Atg9-3xEGFP Δvam3) **A**) in the EGFP channel, **B**) in the FM4-64 channel, and **C**) merge of the two channels, EGFP in green and FM4-64 in red. Vacuoles are indicated by a **V**, white arrows point at Atg9 punctae. All images are a slice of a z-stack (focal depth 220nm). Scale bars 5 µm.

3.2.4 Verification of constructs for autophagy activity

After deciding which fluorescent tags should be used for Atg9 and Atg2 in this CLEM set-up, the expressing constructs were tested by Western blot and by conventional fluorescence microscopy by Mariya Licheva (Kraft group, University of Freiburg, Germany). To do so, each construct was expressed in a yeast strain lacking the genomic copy of the protein expressed from the plasmid. Ape1 processing was chosen as a standard marker for autophagic activity. For both Atg9 constructs, wild-type Atg9 and Atg9-basic mutant (introduced in section 1.7) Ape1 processing, and thus autophagy, functions efficiently upon nitrogen starvation (SD-N, Fig. 3.19A). However, under nutrient rich conditions the Atg9-basic mutant is autophagy impaired and the wild-type Atg9 expressed from the construct shows less efficient Ape1 processing compared to wild-type yeast cells (Fig. 3.19A). These observations match the description of the Atg9-basic mutant in the original publication (Matoba et al., 2020). In the absence of a suitable antibody, Atg9 expression from the plasmids was tested using conventional fluorescence microscopy to detect the mTagBFP2 in Δatg9 cells transformed with each plasmid (Fig. 3.19B). For both Atg9 constructs mTagBFP2 signal could be detected. Taken together, it can be assumed that both Atg9 constructs give rise to sufficient functional amounts of Atg9 and are suitable for the subsequent visualisation studies.

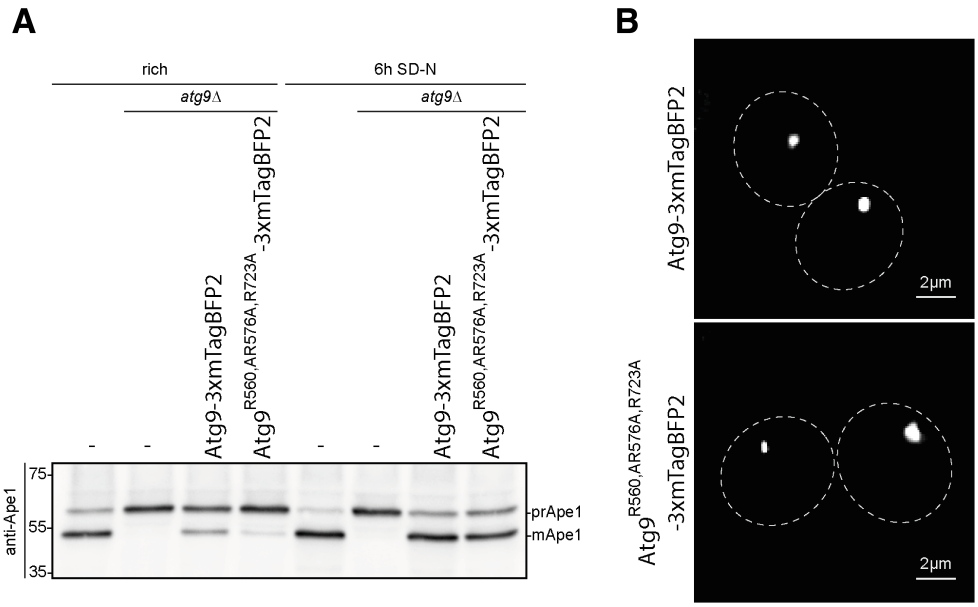

Figure 3.19: Biochemical and microscopical verification of Atg9 expressing constructs used for cryoCLEM. **A**) Western blot of cell lysate from a Δatg9 strain transformed with the Atg9 constructs, in nitrogen starvation and rich media conditions. Cell lysate was probed with an Ape1 antibody, to identify the level of Ape1 processing, from pre-processing Ape1 (prApe1) to mature Ape1 (mApe1). **B**) Conventional fluorescence microscopy images of the cells tested in panel **A**). All results shown in this figure were generated by Mariya Licheva (Kraft group, University of Freiburg, Germany).

The wild-type Atg2 construct gives rise to the same Ape1 processing pattern as wild-type cells (Fig. 3.20, top) indicating that the wild-type Atg2 expressed from the plasmid, works approximately as efficiently as the genomic copy. The Atg2-PM4 mutant construct (introduced in section 1.7) does not show any Ape1 processing, neither under nutrient rich nor under nitrogen starvation conditions (Fig. 3.20, top blot). This is in line with the results of the original publication that studied the Atg2-PM4 mutant (Gómez-Sánchez et al., 2018). Although neither of the constructs could be detected by conventional fluorescence microscopy, both variants of the protein can be detected in the Western blot via the mScarlet tag under nutrient rich conditions (Fig. 3.20, bottom blot, left and middle asterisk). This observation indicates that the lack of Ape1 processing of the Atg2-PM4 mutant is not due to a lack of expression. However, under nitrogen starvation conditions only the wild-type Atg2 protein can be detected via the mScarlet tag (Fig. 3.20, bottom blot, right asterisk). Under both nutrient rich and nitrogen starvation condition, a prominent degradation pattern can be seen for both constructs. Since the wild-type Atg2 construct allows for efficient Ape1 processing under nitrogen starvation conditions and expression of the PM4 variant without an mScarlet tag has been demonstrated by Gómez-Sánchez et al. (2018) and since the PM4 variant can be detected under nutrient rich conditions, it can be assumed that sufficient quantities of both variants are available.

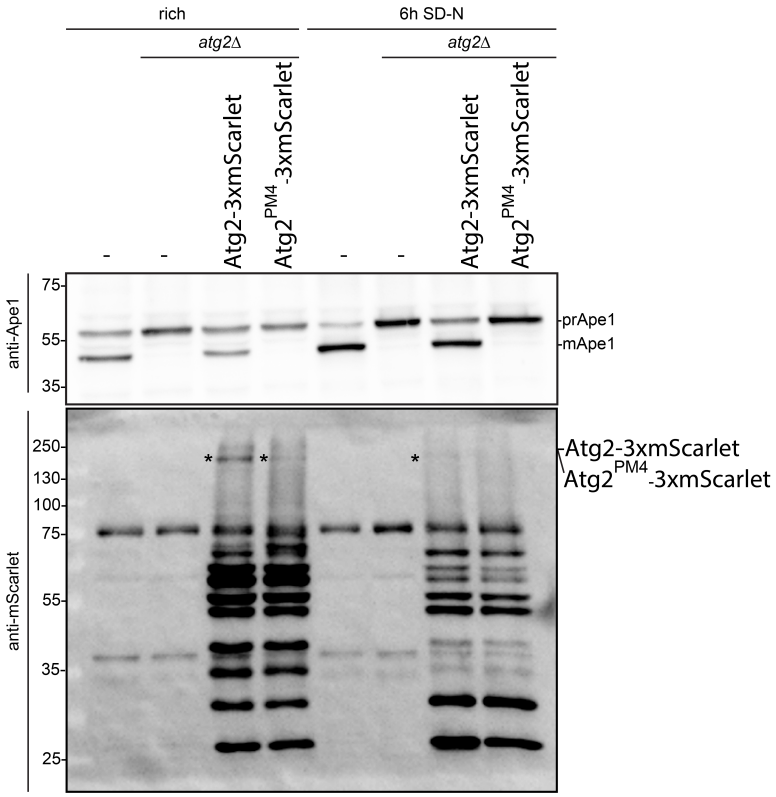

Figure 3.20: Biochemical verification of Atg2 expressing constructs used for cryoCLEM. Western blots of cell lysate from a Δatg2 strain transformed with the Atg2 constructs, in nitrogen starvation and rich media conditions. Western blots were probed for Ape1 and the tag mScarlet. Pre-processed Ape1 and mature Ape1 are indicated as **prApe1** and **mApe1**, respectively. All results shown in this figure were generated by Mariya Licheva (Kraft group, University of Freiburg, Germany).

3.3 Cryogenic CLEM workflow optimisations

The cryoCLEM workflow evolved along the course of this study. the placement of the cryoFM step in a cryoCLEM workflow depends on what the correlation is required for. A targeted milling approach requires a cryoFM step prior to FIB milling. Moreover, if the structure of interest is not readily recognisable in TEM an additional cryoFM step on the thinned lamella preceding TEM, is required. The initial and the final version the cryoCLEM workflow are illustrated in Figure 3.21. With this modularity in mind, the changes and optimisation of this workflow for the posed research question will be explained in this section.

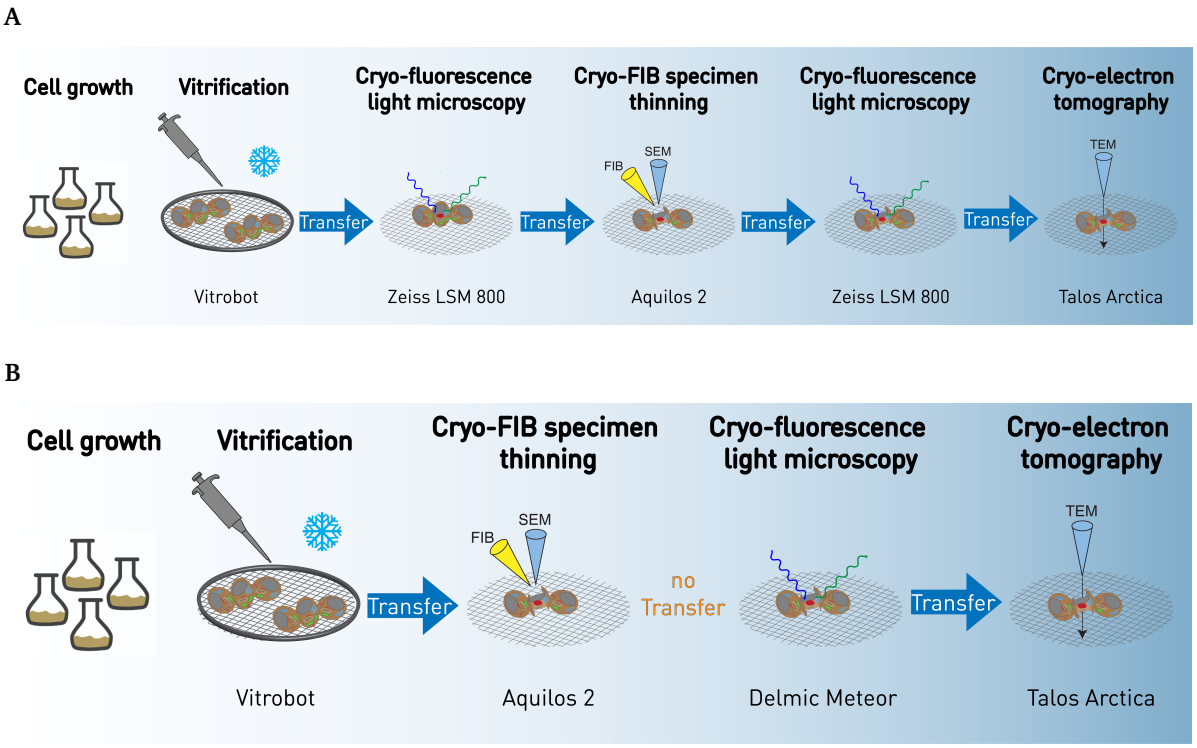

Figure 3.21: Schematic cryoCLEM workflow overview **A**) including the cryo-confocal microscope for screening and imaging of polished lamellae. **B**) Final workflow including retrofitted in-chamber widefield fluorescence microscope.

The initial workflow is schematically represented in Figure 3.21A. By optimising the distribution of cell clusters across the grid and by choosing a strain that increased the number of structures of interest per cell, the first cryoFM step could be omitted. This led to a noticeable reduction in ice contamination visible as black surface deposits on grids in the FIB-SEM as shown in Figure 3.22.

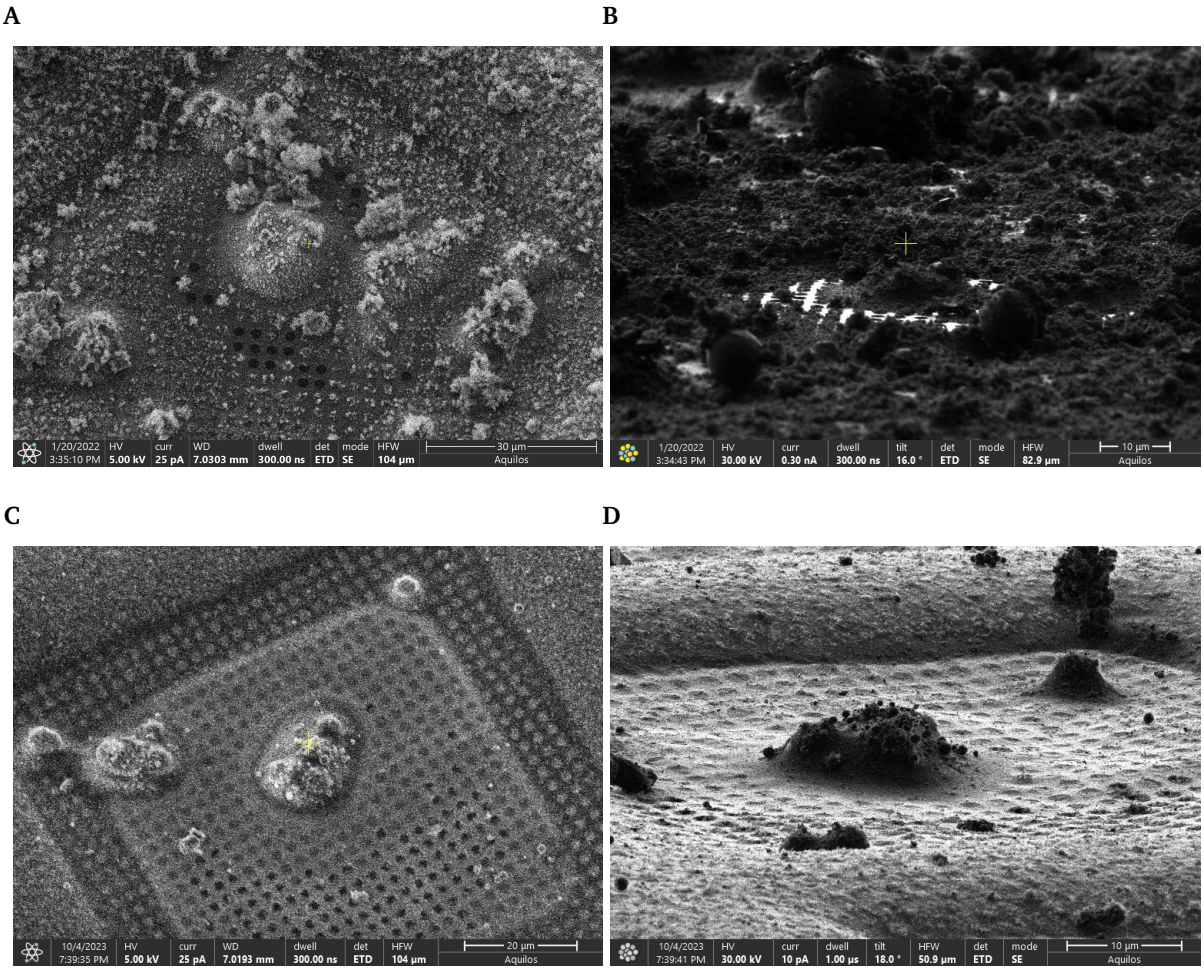

Figure 3.22: Reduction of pre-milling contamination by omitting the screening step on the cryo-confocal microscope. **A**) Electron beam image and **B**) ion beam image of cell cluster on a grid that was screened on the cryo-confocal microscope prior to FIB milling. **C**) Electron beam image and **D**) ion beam image of a sample that was not screened prior to loading it into the FIB-SEM.

The cell cluster on the heavily contaminated grid is more difficult to identify among the dark, textured signal from the ice contamination in both the SEM and FIB image (3.22A and Fig. 3.22B, respectively). Cell clusters are more easily visualised with nearly no contamination on the support film around them (Fig. 3.22C and Fig. 3.22D), which accelerates the milling process.

Another significant change to this workflow came with the addition of an in-chamber cryoFM, Meteor (Delmic BV, Delft NL), to the FIB-SEM. This microscope allows for fluorescence imaging on the same stage and in the same chamber as for the milling process. With such a set-up it is possible to check a lamella in between milling steps for the presence of the structure of interest and in its absence stop work on this lamella to save time. However, doing so makes the total milling time longer and removes possibility for optimisation. After initial trials this time investment had to be weighed against automated milling and manual polishing of all lamellae and only checking for the presence of structures of interest in all lamellae at the end. In order to increase efficiency and throughput, lamellae were not imaged in between each milling steps. Instead, more lamellae were milled per grid.

A

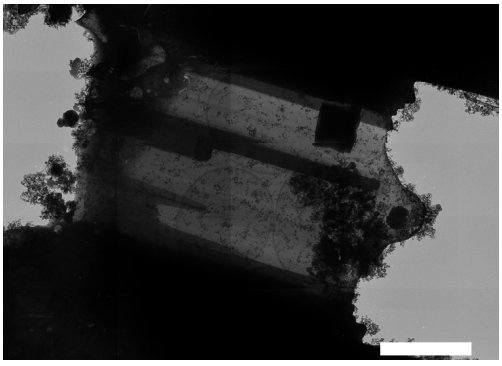

B

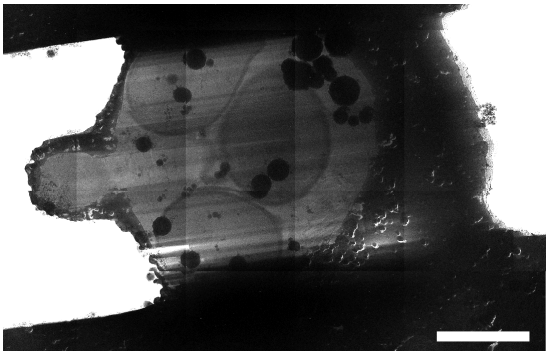

Figure 3.23: Electron microscopy overview of lamella imaged prior on the **A**) cryo-confocal microscope or on the **B**) retrofitted in-chamber widefield fluorescence microscope. Scale bars are 5 µm.

Consequently, the main advantage of the Meteor in this workflow is the reduction of surface ice contamination on the lamellae prior to TEM (Fig. 3.23). A difference in contamination levels is noticeable where tiled overview images of lamellae are shown, one imaged using the Linkam cryo-stage on the LSM800 (Fig. 3.23A) and the other using the in-chamber widefield microscope Meteor (Fig. 3.23B). This is a result of avoiding one sample transfer step in the workflow since the sample does not have to be transferred to the cryo-confocal microscope (Fig. 3.21B). Additionally, imaging the lamellae in a high vacuum environment with an average ice contamination rate of 3 nm per hour (personal communication, FIB-SEM technician Pia Sundermeyer) is significantly better in terms of avoiding contamination, than on the cryo-stage of the LSM800 (Zeiss, Oberkochen, Germany). On the Linkam cryo-stage (CMS196 cryostage, Linkam Scientific Instruments Ltd, Redhill, UK) the sample is held in a nitrogen gas phase above a reservoir with liquid nitrogen to allow measurement with the air objective of the cryo-confocal microscope (explained in more detail section 1.3.1). This set-up is exposed to water vapor from the air which crystallises on the cold surface. Such ice contamination accumulates over time and is highly dependent on the humidity at the time of measurement. While using the Meteor an overall reduction of contamination is apparent, it does not completely eliminate ice contamination as the sample transfer from the FIB-SEM to the TEM still has to be made and is also dependent on atmospheric humidity at the time of transfer. However, the nature of contamination is different and a few larger chunks of ice are deposited rather than the observed carpet of finer contamination over the lamellae. With this different kind of contamination it is possible to find positions on the lamella that are free of contamination. The surface ice contamination increases the total sample thickness to a degree where electrons cannot penetrate and consequently form an image from this region. A more extensive analysis and discussion of ice contamination on FIB-milled lamellae and improvements with the Meteor was done by Berkamp et al. (2023).

As the LSM800 is a cryo-confocal microscope, it has higher resolution in z than the Meteor. Therefore, images of whole cells will inherently be more blurred in the Meteor. By imaging the polished lamella, this difference becomes to a large extent irrelevant as the lamellae are less than 300 nm thick which corresponds approximately to the z-resolution of the LSM800.

For correlation, a linear transformation, potential stretching and mirroring has to be calculated from the cryoFM image to the TEM lamella overview. Correlation was done in SerialEM (Mastronarde, 2003), such that regions of interest could be chosen on the fluorescent image for navigation on the lamellae and imaging in the TEM. To do so a minimum of five registration points present in both images are chosen. Registration points have to be features that are recognisable in both imaging modalities.

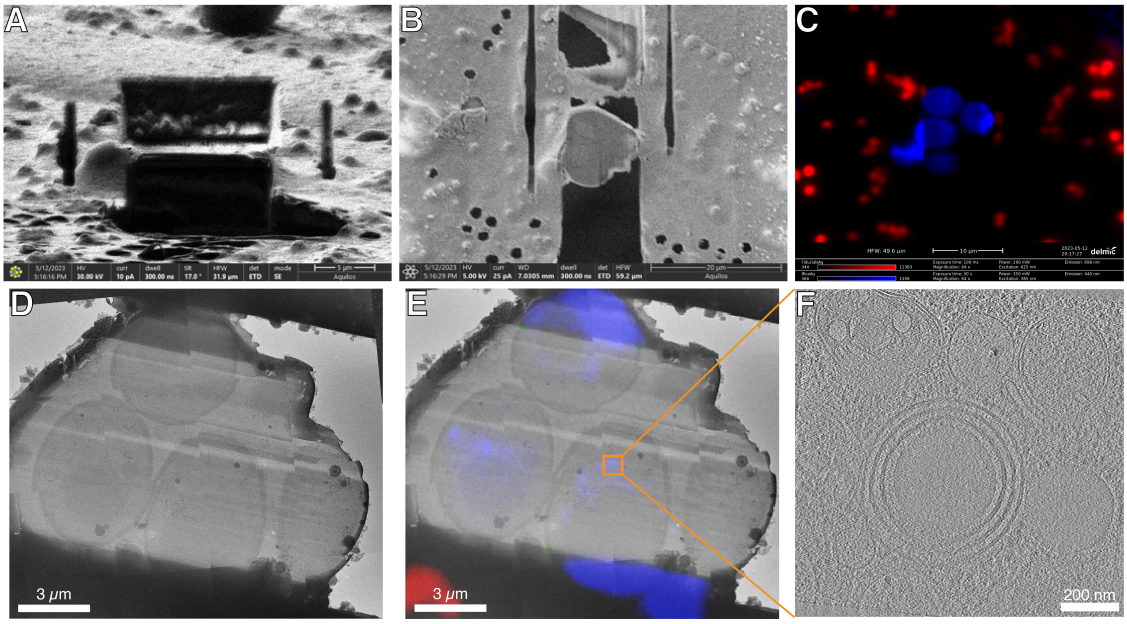

Figure 3.24: Example data collected from the same *S. cerevisiae* lamella across the different microscopes along the presented cryoCLEM workflow. **A**) FIB, **B**) SEM and **C**) fluorescent images of a polished lamella collected in the Aquilos 2 and with the Meteor, respectively. **D**) TEM overview image of the same lamella. **E**) correlated TEM-FM view of the same lamella. **F**)Slice of the tomogram imaged at the indicated (orange box) position in this lamella.

Registration points are also referred to as fiducials which can be prominent cellular features such as lipid droplets or polystyrene microspheres added to the cell media, which can be fluorescently labelled. After trying out two kinds of fluorescently labelled polystyrene microspheres, a different correlation approach was chosen. Since a lamella of yeast cells usually contains several cells, in contrast to mammalian cells, the cell walls visible in the TEM lamella overview were correlated to the autofluorescence of the cytoplasm (Fig. 3.24D). Equally the reflection of the edges of the lamella were used to correlate the cryoFM images of lamellae to their respective TEM images (data not shown). With this correlation approach, mean correlation accuracies of 50 to 300 nm (as calculated by SerialEM after correlation) could still be obtained.

3.4 Multilamellar structures in *S. cerevisiae* △snf7 mutants

As described in section 3.2, in order to accumulate the autophagic membranes in the necessary state of progression all tomographic studies were conducted in snf7 deletion strains. These strains were generated and their genotype verified by Mariya Licheva (Kraft Lab, University of Freiburg, Germany, Fig.A.3). Interestingly, in each studied cell type (introduced in section 1.7), one structure could be observed (Fig. 3.25), resembling multilamellar bodies (MLBs). These structures contain double membranes similar to autophagic membranes but with reduced and highly irregular spacing (up to 10 nm) between the lipid bilayers and with several membranes surrounding each other. Characteristic phagophore rims were not found in these structures, even though one structure presents some highly curved regions (Fig. 3.25, right). These structures were found to be correlated well with fluorescent signal from labelled Atg9 suggesting that these membranes contain Atg9. However, in the WT and Atg2-PM4 mutant these structures were found at 130 nm and 300 nm distance from a phagophore, respectively. Therefore it is also possible that the fluorescent signal originates only from the phagophores. Due to the low resolving power of fluorescence microscopy the exact origin of the fluorescence signals cannot be distinguished clearly. In the Atg9-Basic mutant, no characteristic isolation membranes could be observed in the vicinity of the double membraned structure. While the structure in the variant with WT autophagy factors has a lipid droplet in the centre of the membrane layers, no content is detectable at the centre of the structures in the Atg9-basic and the Atg2-PM4 mutants. It is likely that these structures are ER whorls accumulated in the cytosol due to the lack of Snf7 in the studied strains. Similar observations of ER whorls accumulated in the cytosol in a snf7 deletion strain were made by Schäfer et al. (2020).

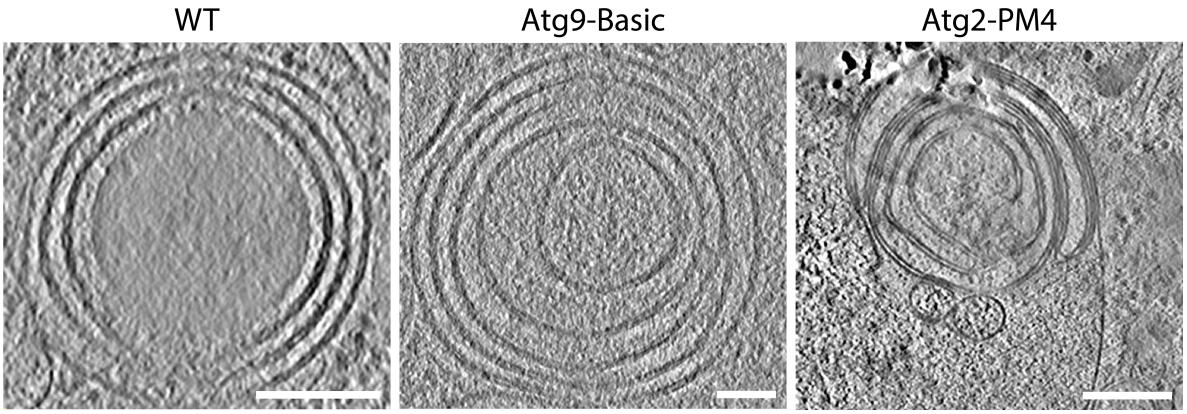

Figure 3.25: Tomograms of unknown multi membrane structures in Δsnf7 strains. Data presented as x-y slices of IsoNet-denoised tomograms. Scale bars 200 nm.

3.5 Characterisation of phagophore elongation by *in situ* cryo-electron tomography

Using the correlative microscopy approach described in section 3.3 the autophagy machinery was studied with wild-type autophagy factors (Atg9 and Atg2, in the following referred to as Aut-WT) as well as with an Atg9 mutant and an Atg2 mutant (introduced in section 1.7), in yeast strains that had the snf7 gene deleted (yML61 and yML123, Tab. A.1). A total of 50 tomograms were collected across the mentioned yeast strains. After excluding the tomograms that were not of sufficient quality due to technical problems and the ones that did not contain clear phagophore rims, 20 tomograms remained, of which six, four and eleven were of the Aut-WT, Atg9-basic and the Atg2-PM4 mutant, respectively (Tab. 3.2). After recording an initial data set of the Atg2-PM4 mutant, a technical replicate was made. Thus, mutant cells were cultured again, vitrified, thinned, and subsequently imaged with TEM in order to ensure the validity of the phenotype observed in this mutant. All tomograms used for analysis are presented as x-y slices of IsoNet denoised tomograms. Segmentation was performed using the neural network based software MemBrain v2 and

manually corrected for errors. The three-dimensional rendering of an segmented Aut-WT phagophore imaged in the process of elongation with ER in close proximity to the phagophore rims is illustrated in Figure 3.26.

TABLE 3.2: **Data collection parameter summary.**

	Total tomograms collected	**Tomograms containing phagophore rims**	**Acceleration voltage (keV)**	**Date cells were grown**
Total	50	21		
Aut-WT	13	2	200	08.02.2022
		4	300	25.04.2023
Atg9-basic	20	4	200	05.07.2023
Atg2-PM4	17	4	200	08.08.2023
		7		12.09.2023

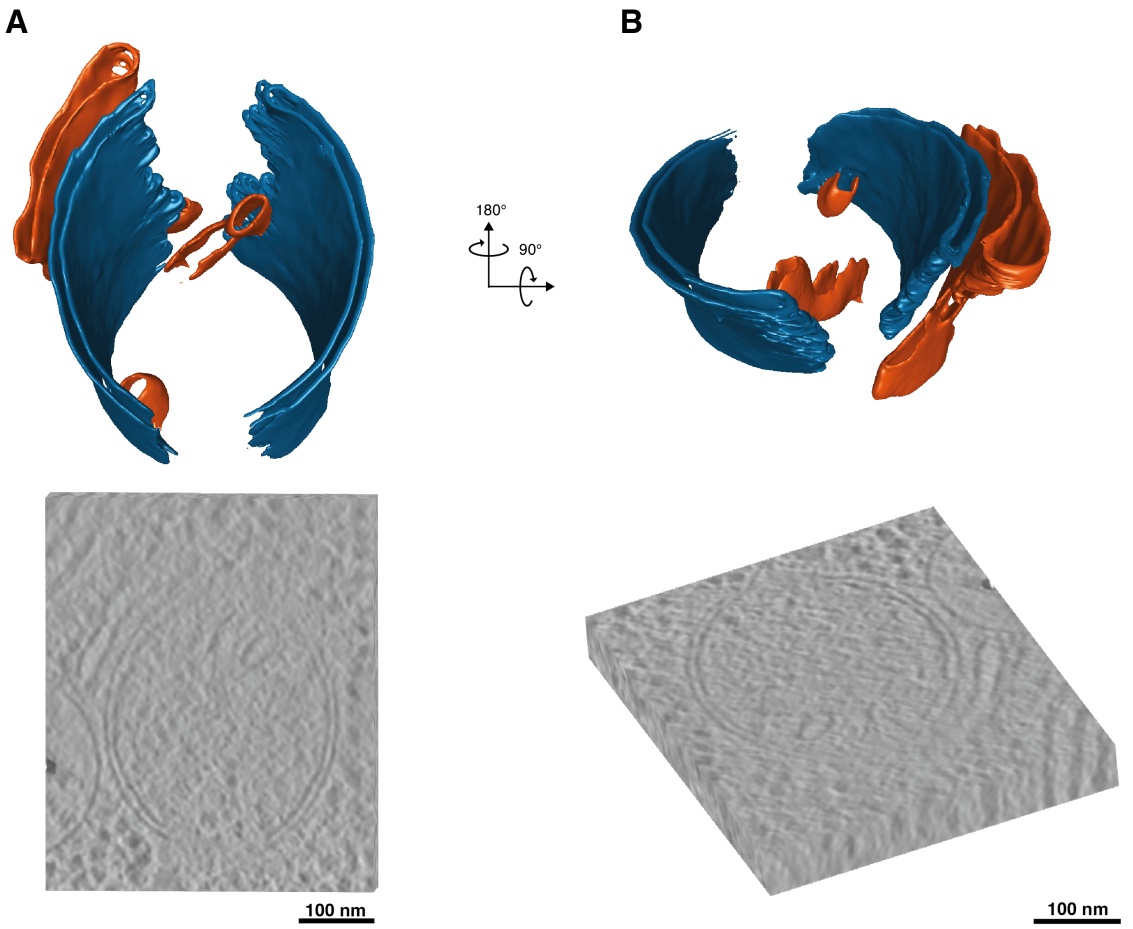

Figure 3.26: 3D rendering of segmentation of an emblematic phagophore during elongation, studied with wild-type autophagy factors from a tomogram shown in Fig. 3.27D. The isolation membrane is shown in blue and the endoplasmic reticulum is shown in organge. Below are shown orthoslices of the tomographic volume in the same the orientation as the 3D rendered segmentations above.

3.5.1 Characterisation of phagophores with wild-type Atg9 and Atg2 in a △snf7 background

In the Aut-WT, phagophores display the characteristic double membrane with visually consistent spacing as well as the recognisable cup-shape (Fig. 3.27). These six phagophores vary in size, from approximately 180 nm to 440 nm. Altogether, phagophores were found proximal to the vacuole, the nucleus, lipid droplets (LDs), and the cell wall. While no organelle contact can be observed in three tomograms (Fig. 3.27A-C), the other three tomograms display phagophores in the process of receiving lipids from the endoplasmic reticulum (Fig. 3.27D), a lipid droplet (Fig. 3.27E) and the nucleus (Fig. 3.27F), indicated by red arrows. In Figure 3.27A one can even observe endoplasmic reticulum (ER) at each rim of the phagophore. The regions of putative lipid transfer are displayed in more detail in Figures 3.27D*-F*. The densities spanning from the ER to the isolation membrane (IM) (Fig. 3.27D*) and the phospholipid monolayer on the LD surface to the IM (Fig. 3.27E*), are 20 to 24 nm long (Tab. 3.3), which corresponds roughly to the suggested length of mammalian ATG2 (Valverde et al., 2019). Interestingly, it is hard to distinguish in Figure 3.27F* whether the nuclear membrane and the IM are bridged by a density or whether this is a direct contact site. In four of six tomograms lipid droplets (LDs) were in proximity to a phagophore (not visible in chosen slice of Fig. 3.27A) which have recently been suggested to play a role in the homeostasis of LDs (Schepers and Behl, 2021).

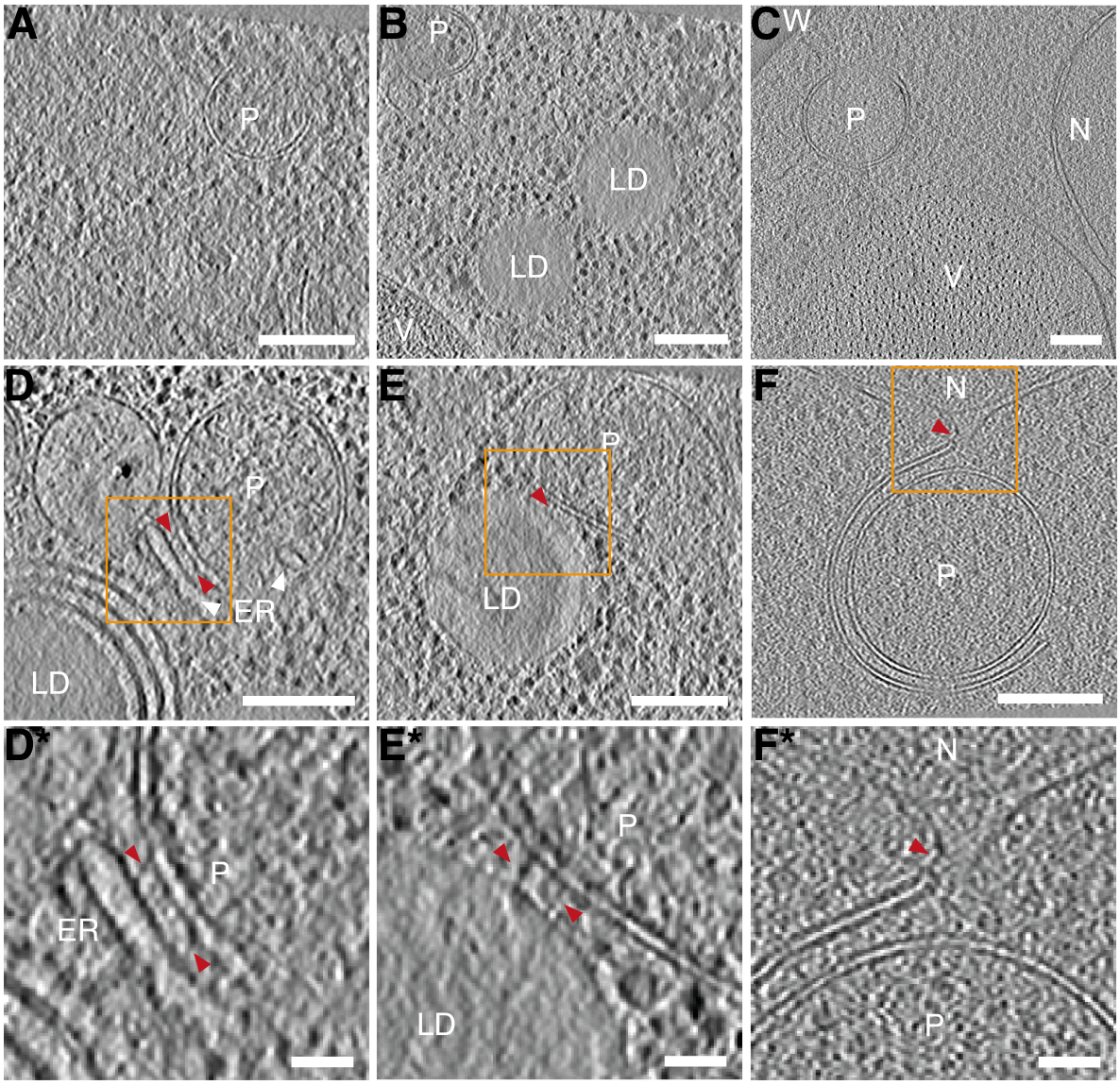

Figure 3.27: Tomograms of phagophores from Aut-WT yeast cells. The presented x-y slices show all the rims that were segmented and analysed from this mutant. Panels **D***) to **F***) represent enlarged views of regions from panels **D**) to **F**) marked with orange boxes. Red arrows in panels **D**) to **F***) show densities spanning from a donor membrane to the isolation membrane, lengths listed in Tab. 3.3. Phagophores are indicated with **P**, lipid droplets with **LD**, endoplasmic reticulum with **ER**, vacuole with **V**, nucleus with **N** and the cell wall with **W**. Presented data stems entirely from IsoNet-denoised tomograms. Scale bars are 200 nm for **A**)-**F**) and 100nm for **D***)-**F***).

TABLE 3.3: **Lengths of densities spanning IM and putative donor membranes in the different yeast mutants. Values were rounded to the nearest nanometer.**

Phenotype	Measured length (nm)	Figure
Aut-WT	20	Fig. 3.27D* (top)
	21	Fig. 3.27D* (bottom)
	24	Fig. 3.27E*(top)
	23	Fig. 3.27E* (bottom)
Atg9-basic	21	Fig. 3.28C
Atg2-PM4	29	Fig. 3.29K and 3.30A (top)
	29	Fig. 3.29K and 3.30A (bottom)
	23	Fig. 3.30B

3.5.2 Characterisation of phagophores in the presence of the Atg9-basic variant

The phagophores of the Atg9-basic mutant presented in tomogram x-y slices (Fig. 3.28) show strong resemblance to the Aut-WT phagophores with the characteristic cup-shape and equally spaced double membrane. As measured from a total of nine phagophores, their size varies from approximately 330 nm to 680 nm.

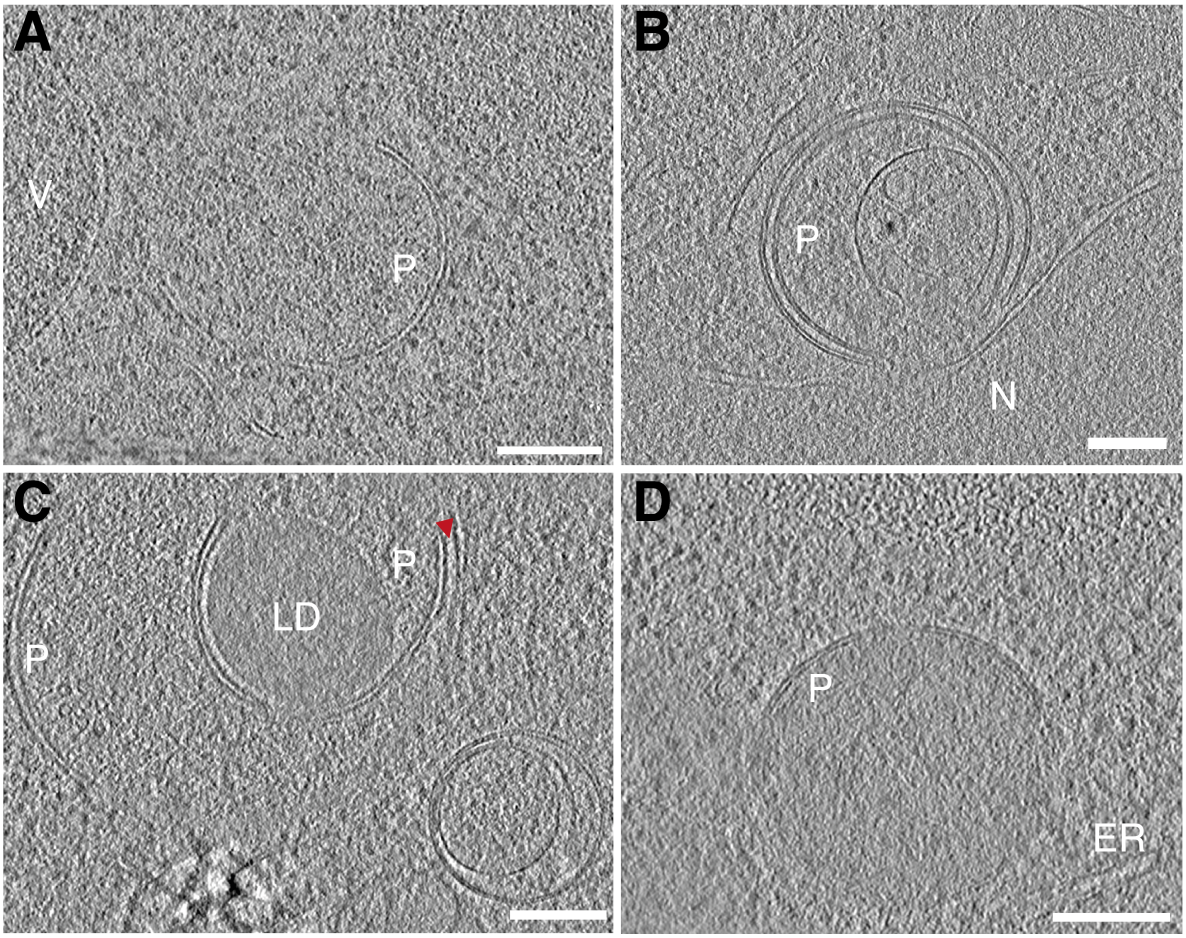

Figure 3.28: Tomograms of the Atg9-basic mutant. Presented x-y slices show all the rims that were segmented and analysed from this mutant. The red arrow in panel **C**) indicates density spanning from phagophore rim to unidentified double membrane, length listed in Tab. 3.3. Phagophores are indicated with **P**, lipid droplets with **LD**, endoplasmic reticulum with **ER**, vacuole with **V**, and nucleus with **N**. Presented data stems from IsoNet-denoised tomograms. Scale bars 200 nm.

Similar to the Aut-WT, phagophores are found in proximity to the vacuole (Fig. 3.28A), the nucleus (Fig. 3.28B), and the ER (Fig. 3.28D). Additionally, in both Figure 3.28C and 3.28D the phagophores are in the process of engulfing LDs. As can be seen in Figure 3.28C, indicated by the red arrow, there is thin density spanning from the IM to another unidentified membrane. This density is approximately 20 nm long (Tab. 3.3) corresponding to the reported mammalian ATG2 length (Valverde et al., 2019).

3.5.3 Characterisation of phagophores in the presence of the Atg2-PM4 variant

The Atg2-PM4 mutant stands in stark contrast to the Aut-WT and the Atg9-basic mutant. The phagophores of the Atg2-PM4 mutant have two types of shapes. While some phagophore rims have a substantially larger intermembrane space (Fig. 3.29A, 3.29C, 3.29D-J), others strongly resemble the Aut-WT (Fig. 3.29B, 3.29F, 3.29J, 3.29K, 3.29L, 3.29M). The rims with larger intermembrane space will subsequently be referred to as 'bloated' rims. Interestingly, one phagophore has one of the aforementioned bloated rims and the other rim of the same phagophore appears to be Aut-WT-like (Fig. 3.29E), while the others exhibit either two Aut-WT-like or two bloated rims. In four out of ten tomograms, there are vesicles in the proximity of bloated rims (Fig. 3.29C, 3.29F, 3.29G-H). In two tomograms, vesicular fusion with the phagophore rims can be observed (Fig. 3.29A, 3.29D-E). Additionally, in three tomograms lipid transfer is observed via direct membrane contact to the phospholipid monolayer of an LD (Fig. 3.30C) as well as what appears to be a protein, seen as density spanning from IM to donor membrane (Fig. 3.30A and 3.30B). Notably, the densities in Fig. 3.30A are approximately 29 nm long, which is 6-10 nm longer than the densities observed in the Aut-WT and Atg9-basic mutant and than the reported length of Vps13p and mammalian ATG2 (De et al., 2017; Valverde et al., 2019). This length corresponds more closely to the yeast protein Csf1, another BLTP family member with a predicted length of 30 nm (Toulmay et al., 2022). Interestingly, the density observed

between the IM and the surface monolayer of the LD (Fig. 3.30) is approximately 22 nm long, which is much closer to the reported length of Vps13p and human ATG2 and the observed densities in Aut-WT (De et al., 2017; Valverde et al., 2019).

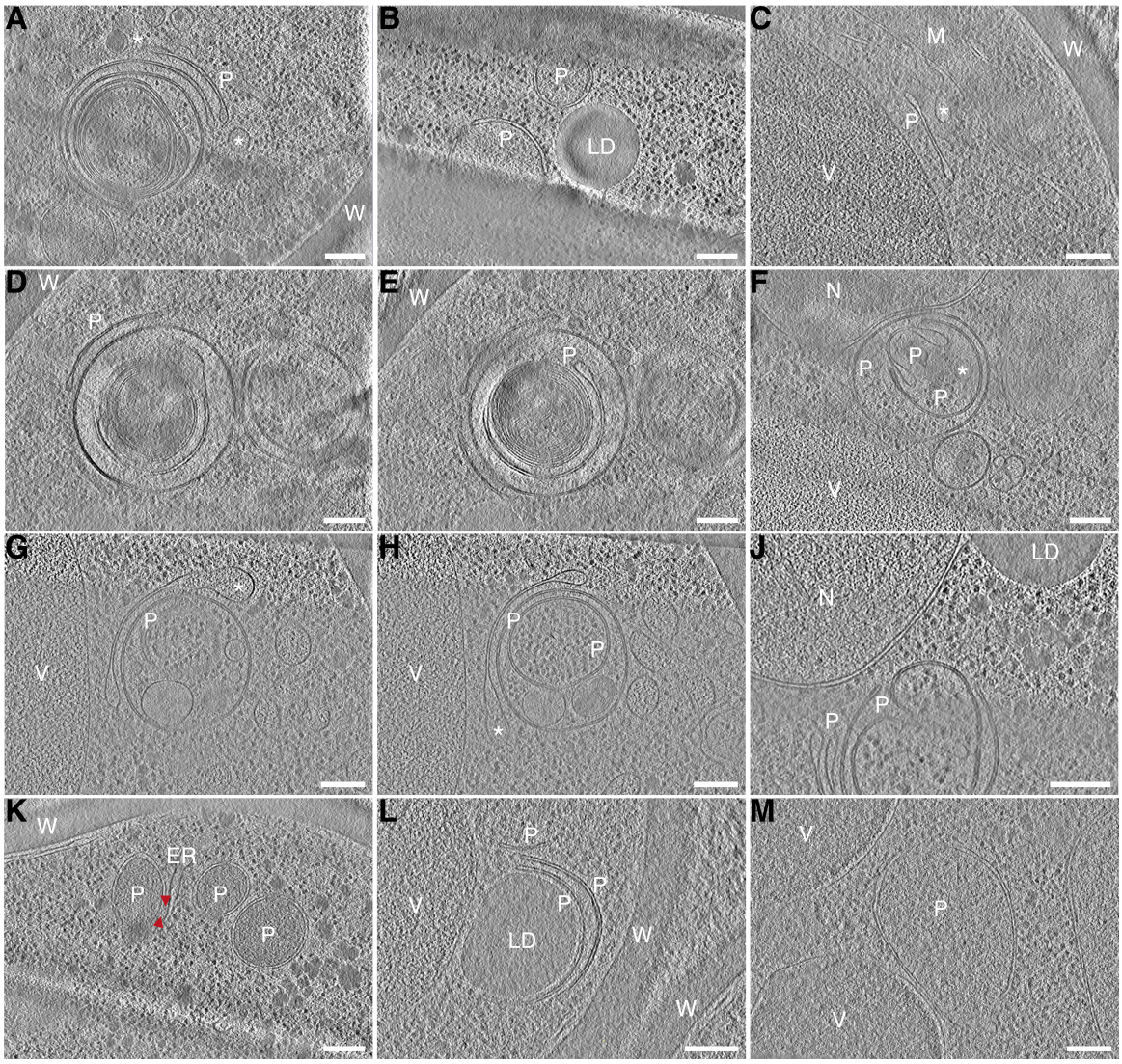

Figure 3.29: Tomograms of the Atg2-PM4 muntant. The presented x-y slices show all the rims that were segmented and analysed from this mutant. **D**) and **E**) as well as **G**) and **H**) show x-y slices from the same tomogram at different positions along z to present both rims as they were segemented and analysed. **K**) Red arrows indicate elongated densities spanning from the isolation membrane to the ER. Phagophores are indicated with **P**, lipid droplets with **LD**, endoplasmic reticulum with **ER**, vacuole with **V**, nucleus with **N**, and the cell wall with **W**. asterisks indicate vesicles of unknown origin. Presented data stems from IsoNet-denoised tomograms. Scale bars 200 nm.

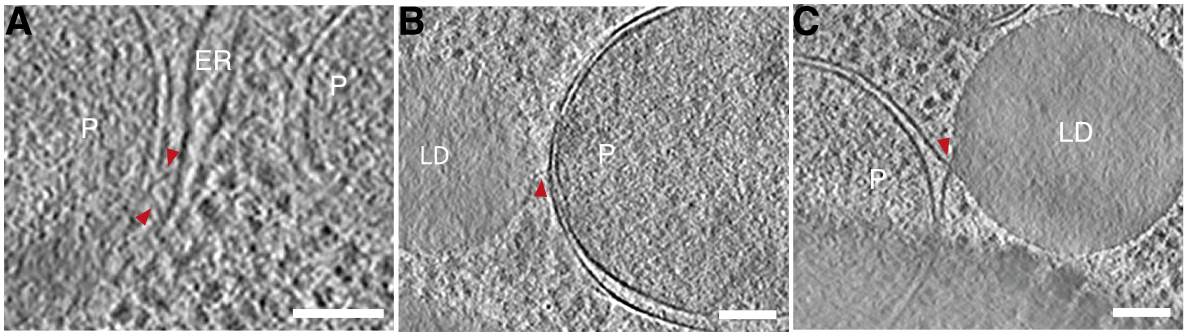

Figure 3.30: Tomograms (x-y slices) of the Atg2-PM4 muntant showing forms of lipid supply. **A**) Zoomed in view of tomogram shown in Fig. 3.29K. **B**) x-y slice of a tomogram showing density bridging lipid droplet surface to isolation membrane (not shown in Fig- 3.29). Lengths listed in Tab. 3.3. **C**) Different x-y slice of the tomogram shown in Fig. 3.29B. Phagophores are indicated with **P**, lipid droplets with **LD**, and endoplasmic reticulum with **ER**. Presented data stems from IsoNet-denoised tomograms. Scale bars 100 nm.

3.5.4 Analysis of the spatial parameters of phagophores

The sizes of phagophores were manually measured in the tomographic x-y slices displayed in Figures 3.27, 3.29, and 3.28 and are presented as box plots in Figure 3.31. While the average size of the Aut-WT is approximately 338 nm, the average phagophore sizes of Atg9-basic and Atg2-PM4 are closer to each other with 481 and 461 nm, respectively. The standard deviation (SD) varies rather strongly with 93, 140 and 163 nm for the Aut-WT, Atg9-basic and Atg2-PM4, respectively. The sizes measured in this study were taken from tomographic x-y slices, which may not show the largest region of the structure. Additionally the sample sizes of the Aut-WT, Atg9-basic and Atg2-PM4 vary strongly with six, nine and 24 phagophores, respectively. Therefore, no conclusions should be drawn from the difference in average size between the Aut-WT and the other variants. Overall, the measured phagophore sizes can be considered in the normal reported range for yeast phagophores (Wen and Klionsky, 2016).

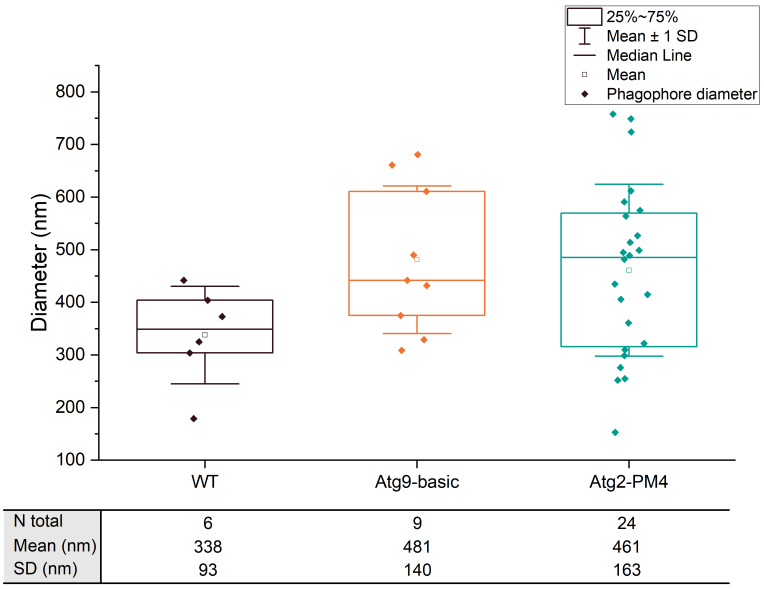

Figure 3.31: Comparison of phagophore size across the *S. cerevisiae* variants. Phagophore sizes (diameter) were manually measured in IMOD.

3.5.4.1 Comparison of isolation membrane distances

For a more thorough comparison of the phagophore rims across the Aut-WT and mutants, the phagophores rims and whenever possible the rest of the IM were segmented in representative tomographic x-y slices with best local contrast. In order to computationally quantify the distance between the outer and inner isolation membranes, small cuts (asterisks in Fig. 3.32) were made in the segmentation to divide it into sub-segmentations. In every phagophore, two cuts were made between the IM and the rims to separate the rim from the rest of the phagophore. Another cut was made in the centre of the bridging section of the rim (see example segmentation in Fig. 3.32) to separate the outer and inner rim membrane. In order to measure the distance between the sub-segmentations (green and orange for rim width or blue and purple for backbone intermembrane distance, Fig. 3.32) a line separating the sub-segmentations was determined using a support vector machine. The distance of a given pixel from one sub-segmentation was defined as the length of the orthogonal line (relative to the separation line) connecting this pixel with a pixel from the other sub-segment. The separate sub-segmentations make it possible to distinguish between rim membrane spacing and the rest of the IM (from now on referred to as backbone, Fig. 3.32).

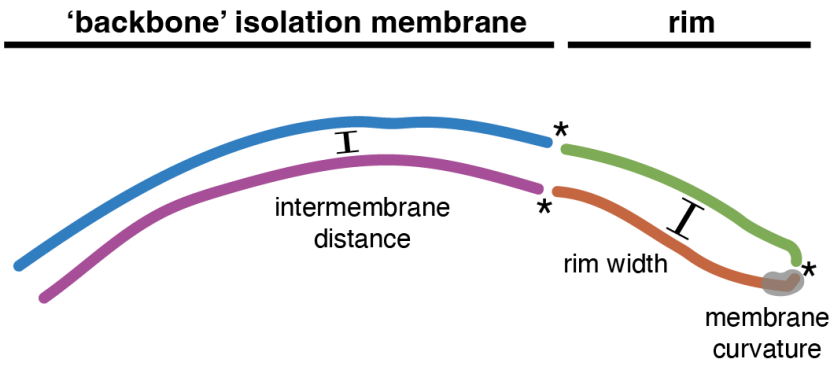

Figure 3.32: Illustration of how the membrane segments were divided and the morphological aspects that were measured (rim width, intermembrane distance, membrane curvature). Cuts made to create the sub-segmentations are marked by asterisks. The blue and purple segment are the outer and inner backbone membranes, the green and orange segment are the outer and inner rim membranes.

The mean spacing between membranes at each rim is plotted in Figure 3.33 along with example segmentations of representative phagophore rims. The mean rim width of the bloated Atg2-PM4 rims with 284 Å differs significantly from the Aut-WT mean rim width of 127 Å. In contrast, the mean rim width of Atg9-basic and Atg2-PM4 thin with 113 Å and 131 Å, respectively do not differ significantly from the Aut-WT. It is also notable that the standard deviation (SD) of Atg2-PM4 bloated rims is much higher than all other rims, with 92 Å as opposed to 21 Å, 18 Å and 26 Å for the Aut-WT, Atg9-basic and Atg2-PM4 thin, respectively.

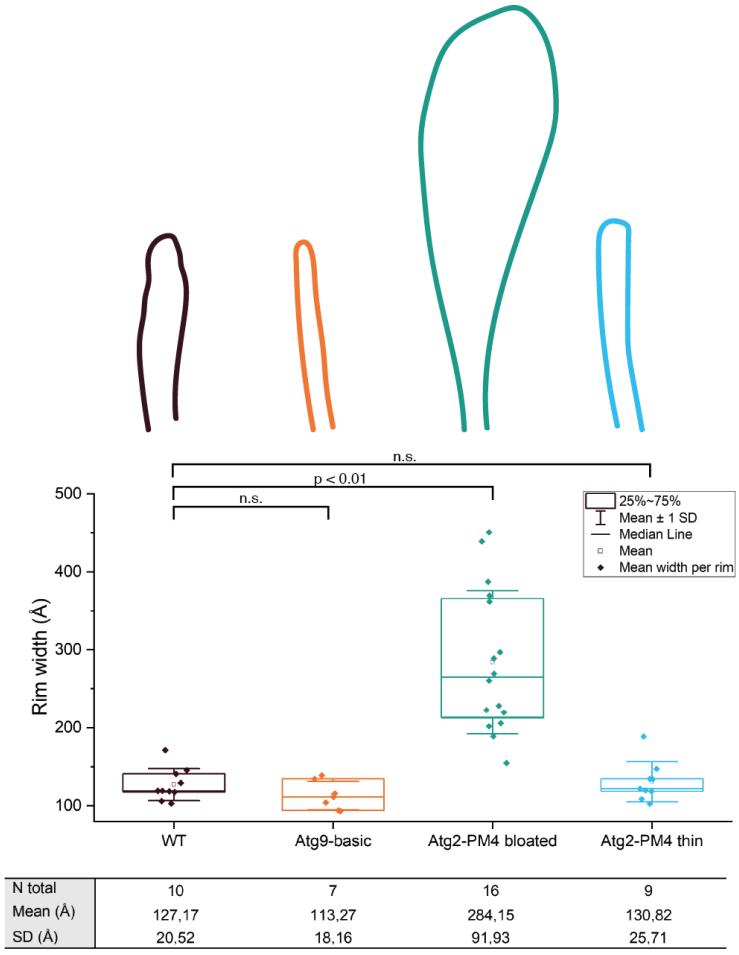

N total	10	7	16	9
Mean (Å)	127,17	113,27	284,15	130,82
SD (Å)	20,52	18,16	91,93	25,71

Figure 3.33: Mean phagophore rim widths from *S. cerevisiae* variants. Illustrated segmentations of representative phagophore rims of each phenotype are shown above the relating plot. Each item in the box plots represents the average rim width of a single rim. Differences between data sets have been assessed with two-sample t-tests. The number of rims (N total), the mean and the standard deviation (SD) for each variant are listed in the table below the graph.

In contrast to the rim width, the intermembrane distances at the phagophore centre, away from the rims (Fig. 3.34) of the mutants do not differ significantly from the Aut-WT. The intermembrane distances of the Aut-WT, Atg9-basic mutant and both bloated and thin Atg2-PM4 phenotypes are 125 Å (± 24 Å), 113 Å (± 32 Å), 119 Å (± 29 Å) and 135 Å (± 29 Å), respectively. Consequently, the Atg2-PM4 mutation only seems to affect the rim morphology rather than the entirety of the phagophore. For better comparison of sample

sizes, the total analysed membrane lengths of 15098 Å, 40122 Å, 23178 Å and 37284 Å for the Aut-WT, Atg9-basic, Atg2 bloated and Atg2-PM4 thin, respectively, are used rather than the number of segmented regions.

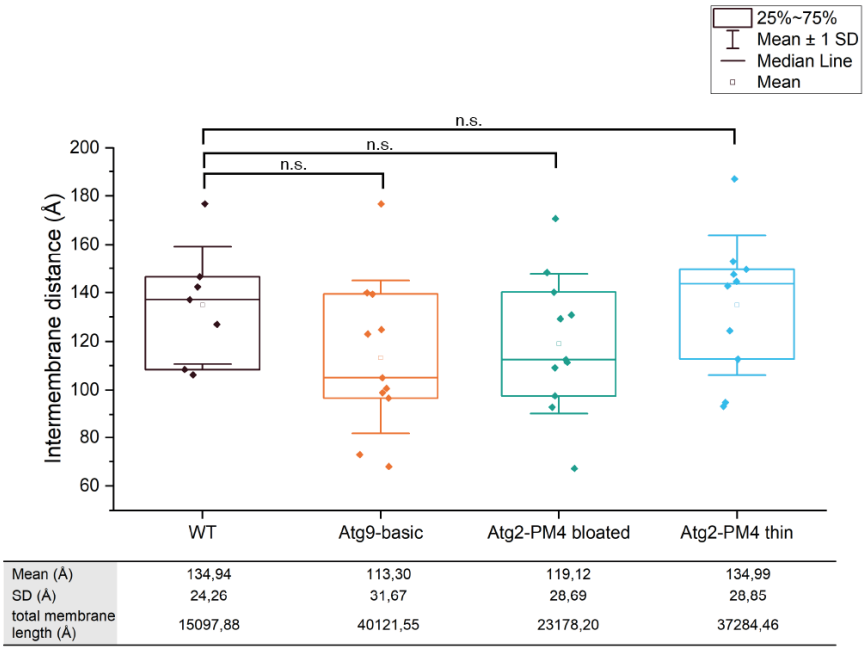

	WT	Atg9-basic	Atg2-PM4 bloated	Atg2-PM4 thin
Mean (Å)	134,94	113,30	119,12	134,99
SD (Å)	24,26	31,67	28,69	28,85
total membrane length (Å)	15097,88	40121,55	23178,20	37284,46

Figure 3.34: Mean isolation membrane spacing at the rim-distal side of the phagophore. Differences between data sets have been assessed with two-sample t-tests. Each item in the box plots represents the average intermembrane distance from a given membrane segment. The mean, standard deviation (SD) and the length of total analysed membrane for each variant are listed in the table below the graph.

3.5.4.2 Analysing the relation between phagophore maturity and rim width

In order to understand whether the changes observed at the phagophore rims are related or dependent on the maturity of the phagophore, the rim opening angle of every rim was determined. The rim opening angle is a measure proposed by Bieber et al. (2022) whereby this angle ranges from close to 0° when the IM is barely cup-shaped to 180° when the rims are nearly facing each other head-on before fusing with each other (illustrated

in Fig. 3.35A). It has been suggested that the rim width increases with the increasing maturity of the phagophore. This has been interpreted as a way to energetically favour the sealing of the phagophore rims to form an autophagosome (Bieber et al., 2022). While this correlation is reflected in the Aut-WT and the Atg2-PM4-thin rims (see linear fit Fig. 3.35B), this effect appears to be completely disrupted in the Atg2-PM4-bloated rims.

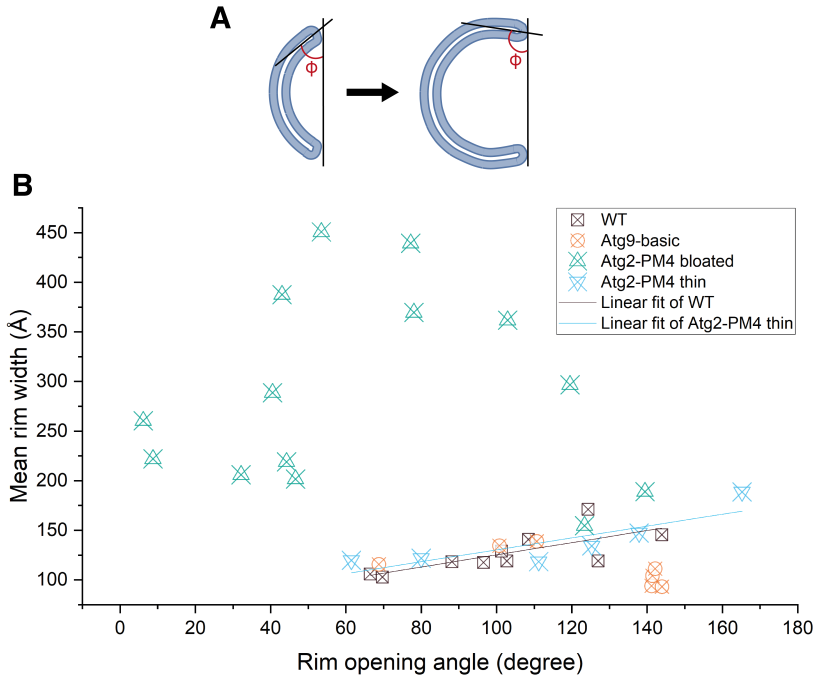

Equation	y = a + b*x	y = a + b*x
Plot	WT	Atg2-PM4 thin
Weight	No Weighting	No Weighting
Intercept	63.98424 ± 21.04012	70.52567 ± 22.54835
Slope	0.61445 ± 0.19953	0.59925 ± 0.18999
Residual Sum of Squares	1734.03279	1046.43455
Pearson's r	0.73649	0.84453
R-Square (COD)	0.54242	0.71323
Adj. R-Square	0.48522	0.64153

Figure 3.35: Rim opening angle in relation to phagophore progression. **A**) Illustration of the rim opening angle at two different stages of phagophore completeness, as proposed by (Bieber et al., 2022). **B**) Rim opening angle plotted against the mean rim width. Each data point represents a single phagophore rim. The tables below the graph summarise the linear fits of the Aut-WT and Atg2-thin data, performed with Origin(Pro) 2023.

The Atg9-basic mutant mean rim widths are within the same range as the Aut-WT up until a rim opening angle of 120°. Between 140° and 150° rim opening angle, the mean rim widths of the Atg9-basic mutant are smaller than of the Aut-WT. However, due to the small sample size one cannot conclusively say whether this effect has been disrupted by the Atg9-basic mutations.

3.5.4.3 Comparison of membrane curvature at phagophore rims

In an attempt to understand the bloated rim phenotype further, the membrane curvature of the rims was measured. To avoid errors due to inaccuracies of segmentation, the segmentations were smoothed with a Gaussian filter prior to measuring curvature of each pixel (more detail in section 6.3.5). Since phagophore rims often have a global curvature additionally to the highly curved membrane region at the very tip, which give the inner membrane an opposite curvature to the outer membrane (Fig. 3.32), the absolute curvature values were used. Comparing the maximum absolute curvature values of the Aut-WT and mutant rims, only the Atg2-PM4 bloated rims differ significantly from the Aut-WT (Fig. 3.36) with a mean of 0.00156 1/Å compared to 0.000862 1/Å, 0.000904 1/Å, and 0.000817 1/Å of the WT, Atg9-basic and Atg2-PM4 thin, respectively.

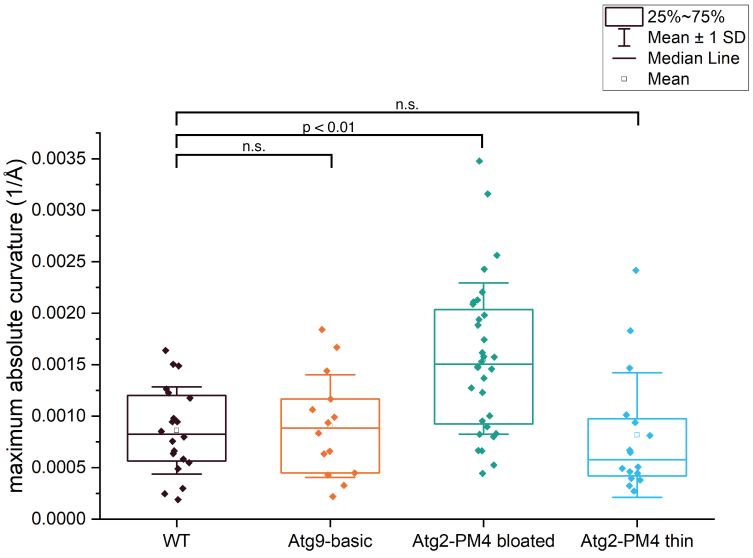

Figure 3.36: Comparison of maximum absolute curvatures of phagophore rims across the different mutants. Each diamond shape plotted represents the max. absolute curvature. Differences between data sets have been assessed with two-sample t-tests in Origin(Pro) 2023.

3.5.5 Vesicular lipid supply in the Atg2-PM4 mutant

The aforementioned vesicular lipid supply is depicted in more detail in Figure 3.37, including maximum diameter and circularity (defined as $\frac{4\times\pi\times area}{circumference^2}$) for each vesicle. While the fusion process itself can only be observed in two tomograms (Fig. 3.37B, vesicle 5 and Fig. 3.37F-G), the close proximity of vesicles to phagophore rims in the other presented tomograms (Fig. 3.37A, 3.37C-E, 3.37H) suggests that fusion of the phagophore with vesicles is likely. Vesicles 1 to 8 are of more circular shape than vesicles 9 and 10. The other vesicles could not be assessed for circularity as the segmentation did not produce a closed object. However, from visual inspection vesicle 11 appears more circular than vesicles 12 to 15. Additionally, the vesicles vary strongly in size (36-189 nm), and appearance across the different tomograms. None of the vesicles have clearly detectable coats, such as clathrin or COPII protein coats as reported by Bykov et al. (2017); Cheng et al. (2007); Zanetti et al. (2013).

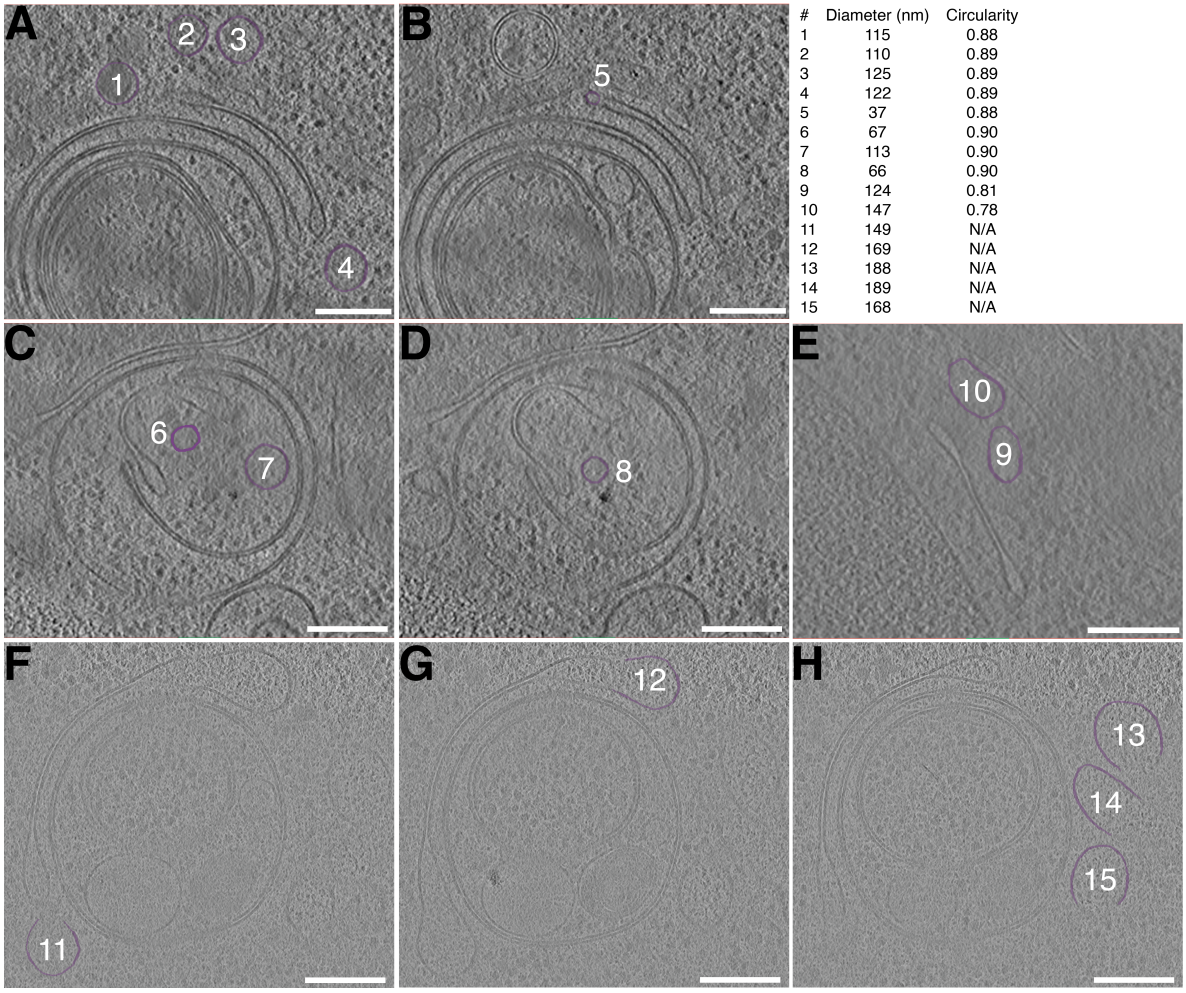

#	Diameter (nm)	Circularity
1	115	0.88
2	110	0.89
3	125	0.89
4	122	0.89
5	37	0.88
6	67	0.90
7	113	0.90
8	66	0.90
9	124	0.81
10	147	0.78
11	149	N/A
12	169	N/A
13	188	N/A
14	189	N/A
15	168	N/A

Figure 3.37: Tomograms of the Atg2-PM4 muntant with vesicles proximal to rims. These are zoomed in x-y slices of tomograms presented in Fig. 3.29. Circularity is defined here as $\frac{4\times\pi\times area}{circumference^2}$. Presented data stems from IsoNet-denoised tomograms. Scale bars 200 nm.

4 Discussion

4.1 Deletion of snf7 in autophagy studies

The Δsnf7 mutation was utilised in this project to prevent the closure of phagophores and the fusion of autophagosomes with the vacuole and hence accumulate phagophores. Based on the data presented in this thesis, the snf 7 deletion mutant showed two notable differences to WT yeast in *in situ* cryoET. Firstly, some of the phagophores observed have other phagophores forming around them (Fig. 3.27F, 3.28B, 3.29A, 3.29D, 3.29F, 3.29J, and 3.29L). This observation can be interpreted as attempts to clear accumulated phagophores from the cytoplasm via the formation of new phagophores. To verify this hypothesis, other unsealed phagophore mutants (such as vps21) or other autophagosome fusion mutants (such as vam3 or ypt7) would need to be studied with *in situ* cryoET.

Secondly, multilamellar structures were observed (Fig. 3.25) resembling MLBs or ER whorls. ER whorls are a stacking of ER membranes in response to various forms of ER stress, namely exposure to DTT, increase of ER specific lipids in the cell or the increased retention of membrane proteins at the ER (Schuck et al., 2014; Koning et al., 1996; Wright et al., 1988). ER whorls have also been observed in other species such as tabacco cells (Gong et al., 1996). Interestingly, the relationship between such ER whorls and the ESCRT machinery has been investigated by Schäfer et al. (2020). In their study, a fusion protein of GFP-Pho8, a common autophagy marker was used to create ER whorls and test the clearing of such via macro-ER-phagy and micro-ER-pagy. It was shown that the deletion of snf7 did not affect the formation of ER whorls but increased their localisation in the cytosol as opposed to the vacuole or other cellular localisations (Schäfer et al., 2020). Since the putative whorls have been observed in Aut-WT, Atg9-basic, and Atg2-PM4 it is unlikely that the Atg9 and Atg2 specific mutations are related to the formation of these structures. However, it is possible that the tagging of Atg9 or Atg2 caused ER stress and that due to

the snf7 deletion, ER whorls accumulate more readily in the cytosol. To verify whether the tagged constructs play a role in the formation of the observed structures, another mutant would have to be studied by cryoET, in which no membrane protein is tagged but snf7 is still knocked out. If whorls were found in such a mutant, this would indicate that their formation is unrelated to the tagging of Atg9 and Atg2.

4.2 Lipid droplets in the context of phagophore elongation

Lipid droplets (LDs) were observed in proximity to phagophores in numerous tomograms of the Aut-WT, Atg9-basic, and Atg2-PM4 (Fig. 3.27, 3.28, 3.29, and 3.30), howerver, they were more numerous in the Atg2-PM4 mutant. The interplay between autophagy and lipid homeostasis has not been fully understood. Autophagy proteins such as Atg2 have been linked to LD homeostasis and vice versa LD-ER contact site proteins have been shown to regulate autophagy (Velikkakath et al., 2012; Pfisterer et al., 2014; Shpilka et al., 2015). Additionally, several enzymes involved in the triacylglycerol (TAG) and steryl ester (STE) synthesis have been shown to be essential for autophagy (Shpilka et al., 2015). It has been reported that when impairing lipid buffering by preventing the formation of lipid droplets, the growth of phagophores is affected due to the altered phospholipid composition of cellular membranes rather than by the restriction of total available lipids for phagophore elongation (Velázquez et al., 2016; Graef, 2018). Moreover, it has been shown that by metabolically correcting the changed phospholipid composition of cellular membranes in lipid-droplet-less cells and reducing fatty-acid stress could rescue the defective autophagy phenotype (Velázquez et al., 2016; Graef, 2018). Lipid droplets have been considered an optional lipid source for phagophore elongation (Graef, 2018).

In the Atg2-PM4 mutant, I have observed one LD making direct contact from the phospholipid monolayer on its surface with the IM of a phagophore (Fig. 3.30C). Furthermore, I have observed LDs tethered by a 23 nm long density to the IM of a phagophore in both

the Atg2-PM4 mutant as well as the Aut-WT (Fig. 3.27E*, Fig. 3.30B, and Tab. 3.3). The densities tethering an LD to a phagophore observed in our data corresponds in length approximately to the reported length of 20 nm of human ATG2 and Vps13p (De et al., 2017; Valverde et al., 2019) which, corroborates the lipid supply function of the lipid droplet for this phagophore.

Direct membrane-to-membrane contact of a phagophore with a lipid droplet *in situ*, as observed in our data, has not been described before. However, short-lived interactions have been captured by traditional fluorescence microscopy (Dupont et al., 2014). Furthermore, a recently published study has shown that LDs are able to carry lipidated LC3B on their surface and during prolonged starvation LC3B positive LDs are tethered to phagophores potentially by LC3B dimers (Omrane et al., 2023). To further disentangle the role of LDs as a lipid source for autophagy from the changes caused by the Atg2-PM4 mutant, phagophore elongation should be studied with *in situ* cryoET with the Atg2-PM4 variant in lipid-droplet-less cells which are metabolically corrected for changed phospholipid composition (as used in (Velázquez et al., 2016)).

4.3 The Atg9-basic variant does not affect phagophore morphology *in situ*

The phagophores observed in the Atg9-basic mutant did not show any significant differences in overall size, rim width, backbone intermembrane space or absolute rim curvature compared to the Aut-WT phagophores (Fig. 3.28, 3.31, 3.33, 3.34, and 3.36). This observation suggests that the investigated mutations in the lateral pore (LP) do not have a significantly strong effect to affect the detectable morphology of phagophores. I chose this mutant because the biochemical data indicated a slight defect in phagophore elongation (Matoba et al., 2020). However, this observation stems from a giant Ape assay, in which

Ape1 is overexpressed to form a large cargo (Suzuki et al., 2013; Gómez-Sánchez et al., 2018; Torggler et al., 2017). Additionally, an *in vitro* assay showed reduced translocation of PI3P to the inner leaflet of liposomes by Atg9-basic (Matoba et al., 2020). I interpreted both of these reported results as indicators for an alteration in the scramblase activity of Atg9 that could have wider effects on the morphology of a native phagophore, possibly by a reduced ability to maintain membrane leaflet asymmetry of the IM (Cheng et al., 2014). However, these experiments were both carried out in non-physiological settings such as giant Ape and *in vitro*. The data presented in this thesis was gathered in a more native experimental setting. The regulation of directionality of lipid translocation by Atg9 is still unresolved (Melia, 2023; Osawa et al., 2022). It is possible that this regulation is carried out by a protein present in our more physiological model, which could buffer the effect of the Atg9-basic mutations. Alternatively, the directionality could be driven by an influx of lipids from Atg2 that was not present in the *in vitro* assay (Osawa et al., 2022). Furthermore, the augmented requirement for supplying lipids in a giant Ape phenotype compared to physiological conditions could be the reason for diminished IM elongation in the Atg9-basic mutant. It is important to note that mutations in the vertical pore (VP) of the Atg9 trimer lead to a complete loss of autophagic flux and a complete block in PI3P translocation in liposomes (Matoba et al., 2020). This loss of function indicates that the VP is more crucial for the proper functioning of Atg9 than the LP. In conclusion, the Atg9-basic mutations do not appear to affect the function of Atg9 severely enough to have an effect on the observable morphology of native phagophores.

4.4 The Atg2-PM4 mutant causes altered phagophore morphology

In the Atg2-PM4 mutant, nearly two thirds of the phagophore rims that were observed had a significantly larger width compared to the phagophore rims in the Aut-WT (Fig. 3.29, and 3.33). The mutated stretch of amino acids in the Atg2-PM4 variant disrupts the interaction between Atg9 and Atg2 (Gómez-Sánchez et al., 2018). As a result, Atg2-PM4 localises at the back of the IM, distal from the phagophore rims where Atg9 and Atg18 are still localised (Gómez-Sánchez et al., 2018). Having this in mind, there are several possibilities how the bloated rims could arise. On one hand, the disrupted interaction with Atg9, could cause a change in the effective scramblase activity of Atg9, which in turn could cause an altered lipid profile of the inner and outer leaflet of the IM. Changes in lipid composition in comparison with WT may already explain the observed changes in the phagophore rim structure. Moreover, since the regulation of the scramblase activity is still not clear, it is reasonable to hypothesise that the interaction of Atg9 with Atg2 could play a role in this regulation. On the other hand, it is possible that the lipid transport activity of Atg2 is reduced and that this lack of lipids is compensated for by an increase in vesicles fusing with the phagophore rims to provide lipids. Vesicle fusion with phagophore rims could be observed on two rims in our data (Fig. 3.37F - 3.37H). It is possible that both putative mechanisms are occurring in this mutant at the same time (illustrated in Fig. 4.1).

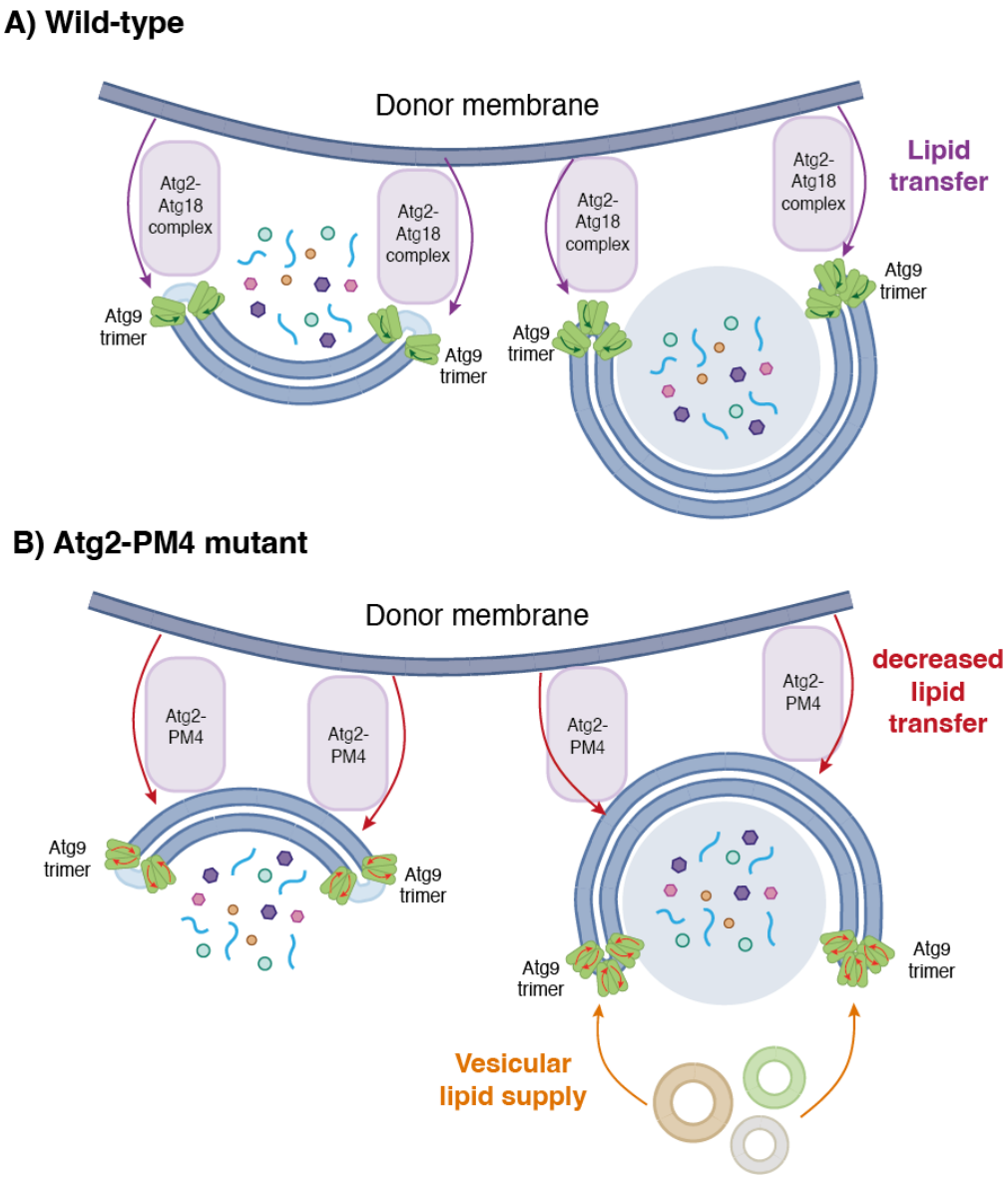

Figure 4.1: Schematic representation of the putative model of altered lipid transfer in the Atg2-PM4 mutant. **A)** Current phagophore elongation model in wild-type yeast with Atg2 transferring lipids (purple arrows) from the donor membrane to the phagophore rims where Atg9 incorporates lipids into the membrane and transfers them to the inner leaflet of the IM (dark green arrows). **B)** Proposed model of altered lipid transfer activity of both Atg2 (large red arrows) and Atg9 (small red arrows) and vesicular lipid supply (orange arrows) in the Atg2-PM4 mutant.

A regulation mechanism has been proposed that could explain both of the above mentioned aspects, lipid transport across the IM leaflets by Atg9, and lipid transport from ER to IM by Atg2. This regulation mechanism involves the fatty acyl-CoA synthetase 1 (Faa1) that generates acetyl-CoA at the phagophore for *de novo* phospholipid synthesis at the ER (Baumann et al., 2024; Schütter et al., 2020). The newly-formed phospholipids are thought to subsequently be channelled to the phagophore by Atg2 with a transfer rate of approximately 200 phospholipids per Atg2 molecule per second (Schütter et al., 2020; Dabrowski et al., 2023). It has been hypothesised that this mechanism drives the net flow of phospholipids from the ER to the phagophore (Osawa et al., 2022). Since the Atg2-PM4 variant tethers the ER to the back of the phagophore, distal from the rims, the putative lipid flow regulation mechanism would be disrupted. Another possibility is that with the lipid influx not proximal to Atg9, the enzymatic activity of Atg9 could be bidirectional instead of unidirectional from the outer to the inner IM leaflet (Fig. 4.1, small red arrows). This suggested model would cover both putative reasons for the bloating of phagophore rims.

The remaining third of phagophore rims in this mutant that have a width resembling the Aut-WT (Fig. 3.29, and 3.33), which can be explained by the presence of alternative lipid transporters such as Vps13 (Dabrowski et al., 2023). Vps13 has been shown to be a lipid transporter acting complementary and non-rate limiting to Atg2 in autophagy (Dabrowski et al., 2023). Furthermore, VPS13A was shown to interact with ATG9A in human cells (Van Vliet et al., 2024). In addition to Vps13 and Atg2, another BLTP family member, Csf1, has been suggested to transfer lipids (Toulmay et al., 2022). Csf1 has a putative length of 30 nm which is in line which the length of densities observed to tether a phagophore with the ER close to the phagophore rim (Fig. 3.30A). Additionally, it is possible that in the absence of regulation of its activity, Atg9 transfers lipids bidirectionally between the membrane leaflets (Fig. 4.1, small red arrows). In this case, it would take longer to

achieve the lipid profile required for thinner phagophore rims. The importance of lipid profile asymmetry in autophagic membranes has previously been demonstrated, with increased levels of PI3P in the luminal leaflets of outer and inner autophagic membrane than in the cytoplasmic leaflet of the outer membrane and the inner leaflet of the inner autophagic membrane (Cheng et al., 2014). In summary, the presence of alternative lipid transporters and the enzymatic activity of Atg9 could both contribute the the occurrence of thin phagophore rims despite the Atg2-PM4 mutations.

4.4.1 Vesicular lipid transfer in the Atg2-PM4 mutant

On two phagophore rims, we observed the fusion of vesicles with approximately 150 nm and 170 nm diameter (Fig. 3.37F, and 3.37G). In other tomograms, vesicles of various sizes were visualised in the proximity of phagophores (Fig. 3.37). The COPII machinery has been shown to directly interact with core autophagy components in yeast (Graef et al., 2013). Furthermore, COPII coat proteins have been observed to localise at the phagophore rims. Additionally, COPII vesicles have been identified as an important lipid source for phagophores in yeast (Shima et al., 2019). However, as can be seen in Figure 4.2, I could not identify characteristic features of clathrin, COPII or COPI protein coats on the vesicles fusing or in the proximity of phagophore rims (examples in Fig. 4.2D and 4.2E). For comparison, examples from *Chlamydomonas reinhardtii* of such protein coats are shown in Figure 4.2B, with the distinct triskelion of clathrin (in panel C') or the triangular Sec13/31 COPII lattice (in panel D'), as elucidated by Bykov et al. (2017). While it is possible that the features visible in the vesicle cross section in Figure 4.2E (yellow arrow), are signal from proteins at the membrane, the limited contrast of this tomogram, does not allow for further conclusions. This could be due to differences in lamellae thickness, or the difference in studied organisms. Taken together, the wide range of observed diameters of

the vesicles next to the phagophore rims (Fig. 3.37) and the lack of detectable specific protein coats (Fig. 4.2) indicate that the vesicles putatively providing lipids to the growing phagophores in the Atg2-PM4 mutant can have very different cellular origins.

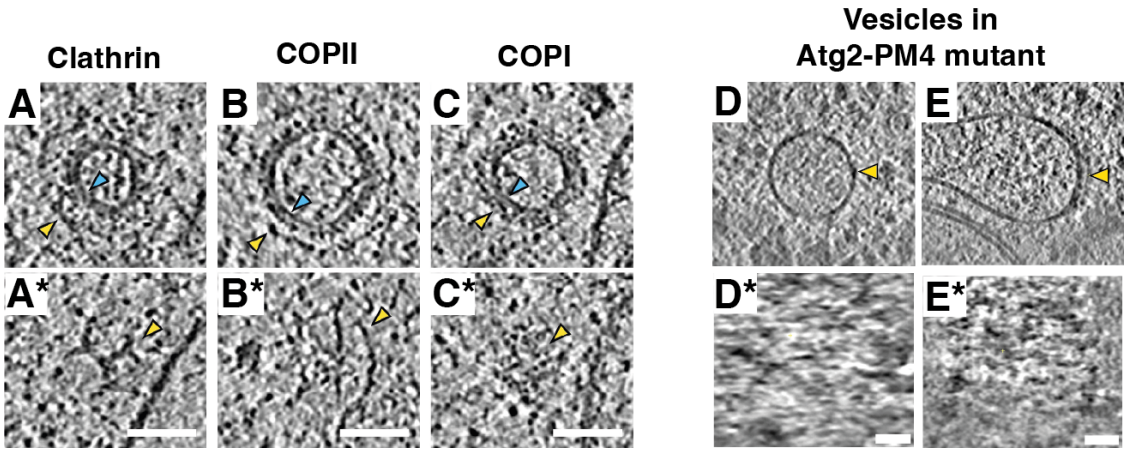

Figure 4.2: Comparison of Atg2-PM4 mutant vesicles with known coated vesicles. **A)** - **C)** Tomographic slices through the centre of **A**) clathrin, **B)** COPII, and **C)** COPI vesicles. **A*)** to **C*)** Tomographic cross section through the protein coat of the vesicles shown in panels **A)** to **C)** by yellow arrows. **D)** - **E)** Example vesicles fusing or proximal to phagophore rims in Atg2-PM4 mutant yeast cells. **D*)** - **E*)** Tomographic cross section where a protein coat should be located, indicated by yellow arrows in panels **D)** and **E)**. Panels **A)** to **C)** and **A*)** to **C*)** are tomographic slices from *Chlamydomonas reinhardtii* reproduced and modified from Bykov et al. (2017). Scale bars are 50 nm.

4.4.2 Rim opening angle and rim aperture constriction in the Atg2-PM4 mutant

The correlation of rim opening angle and mean phagophore rim width has been suggested to reflect on a mechanism priming the phagophore rims for closure of the phagophore into an autophagosome (Bieber et al., 2022). Such a correlation is apparent in the Aut-WT rims, and the Atg2-PM4 thin rims (Fig. 3.35). However, no correlation can be seen in the Atg2-PM4 bloated rims. In light of the previously mentioned vesicular fusion with phagophore rims, it is possible that the mean rim width in the Atg2-PM4 bloated rims

is altered to varying degrees depending on the diameter of the vesicle that fused with the rim. Interestingly, a recent study in yeast found a regulatory role of the Atg2-Atg18 complex in constricting the so-called rim aperture, the opening between the phagophore rims to the cytosol (Shatz et al., 2024). When replacing Atg2 with an N-terminal chorein domain (residues 1-235) Vps13 chimera, rim aperture constriction was rescued. The authors also tested a related Atg9-binding mutant, known as Atg2-PM1 (generated by Gómez-Sánchez et al. (2018) in the same study as Atg2-PM4), which failed to perform rim aperture constriction due to mislocalisation. The mislocalisation of Atg2-PM4 has been shown to be the same as for Atg2-PM1 (Gómez-Sánchez et al., 2018). One may therefore conclude that the Atg2-PM4 variant, not localised at the rims, should equally fail to constrict the rim aperture. The correlation of mean rim width and rim opening angle of the Atg2-PM4 thin rims in our data appears to contradict this finding. It is unclear how the localisation of Atg18 at the phagophore rims without Atg2 in the Atg2-PM4 mutant affects the rim aperture constriction. Further studies are required to disentangle the specific roles of Atg18 and Atg2 in this process and to understand how the Atg2 analogue Vps13 acts in rim aperture constriction.

5 Outlook

CryoCLEM, *in situ* cryoET, and subtomogram averaging (STA) are methods enabling the advancement of structural knowledge in the context of native cellular environments. These methods are expected to reach higher resolution and gain more detailed information (Böhning and Bharat, 2021). So called montaged or tiled tomography is a recent development to bride the gap between large field of view tomogram acquisition and higher magnification, i.e., higher resolution data acquisition (Peck et al., 2022; Yang et al., 2023). In such a montaged acquisition scheme, several high-magnification tilt-series are acquired in parallel for instance in a spiral pattern, with sufficient overlap for cross-correlation guided alignment of the tiles. This measurement scheme also allows for STA to be performed across the individual tilt-series. With further development montaged tomography will make large fields of view such as entire lamellae accessible for high-resolution characterisation. For the rare events visualized in this thesis, such improved approaches will easily increase the amount and quality of data available for detailed image analysis.

Another current hurdle for more comprehensive analysis, is that only approximately 0.22 % of the cellular volume are captured in the tomograms after the generation of thin lamellae (Turk and Baumeister, 2020). In an attempt to obtain a more complete coverage of the cellular volume at high resolution Schiøtz et al. (2023) developed a modified approach to cryo lift-out called serial lift-out. This method consists of producing lift-out lamellae from the majority of a vitrified organism or tissue slab as exemplified on a *Caenorhabditis elegans* L1 larvae with 38 sections. This method is extremely time consuming and error-prone, hence further development is required to render it more accessible to the wider structural biology community.

One limitation of this thesis work, is the necessity to produce thin lamella of 80 nm to 300 nm, limiting the observable section of phagophores that are commonly 400 nm to 900 nm in size (Takeshige et al., 1992). This limitation could be addressed in the future by using C_C-corrected microscopes (Rez et al., 2016; Dickerson et al., 2022) for signal contribution. Additional signal could be expected from reduced radiation damage using microscope stages at lower Helium temperatures (Naydenova et al., 2022). Moreover, the development of high-resolution STEM for biological specimens is a promising method to overcome some of the current thickness limitations (Lazić et al., 2022; Wolf et al., 2014; Rez et al., 2016).

To reduce the human operation time and increase sample through-put, machine learning has been used to automate milling site recognition for automated set-up and FIB-milling of lamellae. When wanting to set-up milling sites based on correlative information, no automation is currently available. The use of machine learning for fluorescence-guided targeted milling is yet to be addressed but has potential in further reducing human operation time at the FIB-SEM and therefore increasing sample through-put.

As the localisation of fluorescently labelled proteins is currently limited to about 200 nm (Kaufmann et al., 2014), advancing the localization resolution will be of significant benefit to reliably map proteins in the tomograms. Super-resolution (SR) cryogenic fluorescence microscopy (cryoFM) is an active area of method development. Obtaining higher resolution with cryoFM is advantages for the accuracy of cryoCLEM. One of the problems, that is yet to be addressed, is the lack of cryogenic immersion objectives, which would not only improve the obtainable resolution but also reduce devitrification (Dahlberg and Moerner, 2021). The difficulty in developing such a cryogenic immersion objective would be to avoid aberrations arising from the different elements in the objective with varying thermal expansion coefficients (Kaufmann et al., 2014). Furthermore, the use of TEM grids is a challenge

in SR cryoFM due to increased local devitrification and light-induced blinking which is not observed with traditional sample holders such as sapphire coverslips (Dahlberg and Moerner, 2021). Finding a more appropriate sample support than TEM grids may help SR cryoFM and by extension cryoCLEM reach higher resolution and correlation accuracies.

Ultimately, when proteins are reliably located to high resolution, they can also be considered for further structural averaging analysis. STA has proven useful to understand protein structures, especially protein complexes, in their cellular context. Bharat et al. (2017) used STA in combination with x-ray crystallography to elucidate the wider organisation of the bacterial S-layer in *Caulobacter crescentus*. The current resolution record with STA is 1.6 Å from purified mouse Apoferritin (EMD-16032), proving that there is no theoretical limitation on the obtainable resolution with STA. However, most STA structures derived from *in situ* tomograms currently have a resolution between 8 Å and 12 Å (The wwPDB Consortium et al., 2024). This practical limitation is due to a number of factors that are more pronounced in cryoET in comparison to cryoEM, including poor signal-to-noise ratio, sample movement and challenging defocus determination and CTF correction due to stage movement and specimen tilt (Wan and Briggs, 2016). The sample thickness of FIB-milled lamellae is still significantly higher than in typical single-particle samples leading to a higher fraction of inelastically scattered electrons. Additionally, the number of subvolumes, i.e., particles in *in situ* cryoET is more restricted than in SPA, due to the relatively low abundance of most proteins, unless studying a protein with high local concentration such as e.g. mitochondrial proteins. Recently, a new sub-variation of *in situ* electron microscopy arose referred to as *in situ* single particle analysis (isSPA) in which particles were picked in a template-matching fashion from a high-dose single tilt image of a cellular FIB-milled lamella (Lucas et al., 2021; You et al., 2023; Cheng et al., 2021). With technical improvements such as more stable microscope stages, FIB-milling schemes that

yield more stable lamellae and further software development the commonly obtainable resolution for STA will further improve and hopefully catch-up with SPA. Especially the use of Cc-correction will likely contribute by improving signal. Furthermore, cryogenic scanning transmission electron microscopy (croySTEM), a variation of TEM in which an electron probe is scanned across a specimen rather than illuminating the sample with a wider beam at once, will contribute to the improvement of *in situ* electron microscopy due to improved contrast of thicker samples and at higher tilts (Lazić et al., 2022; Wolf et al., 2014). All these emerging developments contribute to the goal of high-resolution structural proteomics of entire cells or even tissue sections.

The previously determined Atg9 and Atg2 structures contributed significantly to understanding the roles of Atg9 and Atg2 in phagophore elongation (Matoba et al., 2020; Maeda et al., 2020; Valverde et al., 2019; Wang et al., 2023). However, the regulatory mechanisms necessary for the scramblase and lipid transfer function of Atg9 and Atg2, respectively, have not been elucidated. In this work, I have established a fluorescence set-up usable in a cryoCLEM workflow in order to study phagophore elongation *in situ*. The data presented in this thesis underpins the importance of the interaction between Atg2 and Atg9 for the overall phagophore morphology by showing that the disruption of this interaction has drastic effects on the phagophore rim morphology. Moreover, the data in this thesis underlines the relevance of Atg2 as a lipid transporter in phagophore elongation, since mutating this protein appears to affect how lipids are brought to the phagophores.
To precisely understand the functioning of Atg2 and how phagophore elongation is being regulated, further studies are required including mutational studies on Atg2, both *in vitro* and *in situ* in the absence of Vps13 and possibly other BLTP family members. Specifically, lipid transfer blocking mutants that still interact with Atg9 and the ER, would be particularly relevant to disentangle the lipid transfer activity from potentially regulatory

interactions between Atg9 and Atg2. The emerging technologies and methodologies in *in situ* cryogenic electron microscopy will help in achieving this goal.

6 Experimental procedures

6.1 Molecular biology

Some constructs used in this work could not be cloned in-house after numerous attempts and were subsequently sent to GenScript (Piscataway NJ, USA) for cloning.

6.1.1 Polymerase chain reaction (PCR)

Polymerase chain reaction was carried out as described by Sambrook and Russell (2001) with minor modifications according to the recommendations of the manufacturer of Q5 polymerase (New England BioLabs, Ipswich, MA, USA) or Phusion polymerase (New England BioLabs, Ipswich, MA, USA). The PCR programs used are shown in Table 6.1. Denaturation, annealing and elongation steps were repeated for 30 cycles.

6.1.2 Agarose gel electrophoresis

Preparative agarose gel electrophoresis was carried out as described by Sambrook and Russell (2001). for the linearised plasmids 0.8 % or 1% agarose gels were used. For the insert PCR products, an agarose percentage of 2% was used. Electrophoresis was run at 100 to 120 V (const.) for 1 hour. Gel bands of the expected size were excised and retrieved

TABLE 6.1: **Polymerase chain reaction program used for a variety of cloning experiments including linearisation of plasmids for subsequent Gibson assembly or amplification of tags of interest.**

Step	Temperature	Time
Initial denaturation	98°C	30 seconds
Denaturation	98°C	10 seconds
Annealing	variable	20 seconds
Elongation	72°C	variable
Final Elongation	72°C	2 minutes

using a gel extraction kit (Qiagen, Hilden, Germany).

6.1.3 DpnI digest

Digestion of DNA was carried out by mixing 50 µl PCR product with 10 U of the enzyme (New England Biolabs, Ipswich, MA, USA). This mixture was incubated for one hour at 37°C.

6.1.4 Gibson assembly

Gibson assembly was carried out according to Gibson et al. (2009) and the instructions of the Gibson Assembly Master Mix manufacturer (New England BioLabs, Ipswich, MA, USA). Inserts were designed to have 5' and 3' overlapping regions of 15 to 30 nucleotides in length, with the ends of the linearised plasmid. For the reaction mixture, the linearised plasmid and insert were mixed 1:1 with Gibson Assembly Master Mix (New England BioLabs, Ipswich, MA, USA) to a total volume of 10 µl. This mixture was then incubated for up to 20 minutes at 50°C and subsequently transformed into *E. coli* DH5α.

6.1.5 Transformation of plasmids into DH5α

Competent *E. coli* DH5α cells were purchased from New England Biolabs (Ipswich, MA, USA). The transformation protocol was conducted as outlined in the manufacturers manual. Briefly, the plasmid DNA was incubated 30 minutes with the cells on ice. Subsequently the cells were exposed to a heat shock of 30 seconds at 42°C before being cooled again on ice for five minutes. The cell suspension was then supplemented with 450 µl SOC medium (supplied by manufacturer) and incubated at 37°C for a minimum of one hour. Finally, 50 to 100 µl of this suspension was used to be spread on an LB agar plate supplemented with the antibiotic that the plasmid carries a resistance gene for.

6.2 Yeast handling

All yeast strains used for this work (Table A.1) were kindly provided by Prof. Dr. Claudine Kraft (University of Freiburg, Germany). These strains were generated and verified for accurate genotype by Maria Licheva from the Kraft lab. When necessary the cells were transformed with plasmids (Table A.2) as described below. Some plasmids were modified as described above from plasmids also kindly provided by Prof. Dr. Claudine Kraft.

6.2.1 Yeast cell transformation by the LiAc/SS Carrier DNA/PEG Method

Transformation procedures are described in (Gietz, 2014) as the 'Quick and Easy Transformation Protocol' with minor modifications. In brief, the transformation buffer should be prepared in advance (0.24 M Lithium acetate, 47% PEG 3550 or PEG 4000, sterile filtered). Prior to the reaction a patch of the yeast strain of interest were grown on a selection agar plate (usually YPD agar supplemented with the required antibiotic). The salmon sperm carrier DNA (Sigma Aldrich, Burlington, MA, USA) was denatured in a boiling water bath for five minutes before quenching it on ice for two minutes. The reaction mix was composed of 5 µl single stranded carrier DNA, 85 µl transformation buffer, 10 µl 1M DTT and 0.5 to 2 µl of the plasmid (at 300 to 500 ng/µl concentration). Subsequently the yeast colony/path was scraped off the agar with a sterile loop and mixed into the transformation reaction mix. This suspension was very briefly vortexed and incubated at 45°C for exactly 30 minutes. Finally, the reaction mix was plated out on the appropriate selection agar plate, depending on the selection marker on the plasmid. The agar plate was incubated at 30°C for two to three days.

6.2.2 Yeast cell cultivation

Pre-cultures (10 ml) with either YPD or synthetic drop-out media (Formedium, Norfolk, UK) supplemented with 2% glucose (Tab. 6.2), were inoculated with a single colony. Cultures were incubated at 30°C and agitated with 95 rpm for at least 14 hours to ensure cells would not be stressed. The $O.D._{600}$ was monitored and as soon as it was between 0.55 and 0.8 the pre-culture was used for starvation and plunge freezing. For nitrogen starvation the cells were pelleted at 3000 x g for five minutes and washed three times with SD-N media (Formedium, Norfolk, UK) (Tab. 6.2). Cells were incubated in SD-N media for a minimum of two hours and a maximum of five hours before plunge freezing. Where indicated cells were dyed (section 6.2.3) and/or autophagy was induced by rapamycin treatment instead of nitrogen starvation. In those cases, cultures were supplemented with 250 nM rapamycin (solved in DMSO, Sigma Aldrich, Burlington, MA, USA) without intermediate washing steps. The incubation time with rapamycin ranged from 30 minutes to three hours. Subsequently cells were vitrified as described below.

6.2.3 Yeast cell staining

For staining of internal membranes, particularly the vacuolar membrane, FM4-64 dye (N-(3-Triethylammoniumpropyl)-4-(6-(4-(Diethylamino) Phenyl) Hexatrienyl) Pyridinium Dibromide, Invitrogen,Thermo Fisher Scientific, Waltham, MA, US) was used. The dye has excitation/emission maxima of 515/640 nm and was supplied lyophilised. In order to use the dye, 100 µg of the dye powder were resuspended in 20 µl deionised water. This suspension was further diluted 1:10 in cell growth media (either YPD or SD-X, see Tab. 6.2 depending on which media the cells were grown in). Of the latter suspension, 2 µl were added to 100 µl of the cell suspension that was to be stained. This means the cells were stained with a final concentration of 10 ng/µl of dye. The cells were incubated with FM4-64 for 30 to 45 minutes at 30°C and agitated with 700 rpm. Subsequently, the cells

were washed with fresh media three times, by sedimenting the cells using centrifugation at 3000 x g for five minutes and resuspending the pellet in fresh media each time. A further incubation in fresh media for 45 to 50 minutes at 30°C and agitated with 700 rpm allows for the dye to be transported from various membranes in the cell to the vacuole. After this, the cells could be treated with rapamycin or be subjected to nitrogen starvation as described in section 6.2.2.

TABLE 6.2: **Media used for cultering *S. cerevisiae* in this work.**

Media	**Composition**
Yeast extract-peptone-dextrose growth medium (YPD)	2% (w/v) bactopeptone 1% (w/v) yeast extract 2% (w/v) glucose
Syntheitc drop-out medium -Leucine (SD -Leu)	1.9 g/l synthetic complete mixture drop out: -Leu 6.7 g/l yeast nitrogen base without amino acids 2 % (w/v) glucose
Syntheitc drop-out medium -Uracil (SD -Ura)	1.9 g/l synthetic complete mixture drop out: -Ura 6.7 g/l yeast nitrogen base without amino acids 2 % (w/v) glucose
Syntheitc drop-out medium -Uracil -Leucine (SD -Ura -Leu)	1.9 g/l synthetic complete mixture drop out: -Ura -Leu 6.7 g/l yeast nitrogen base without amino acids 2 % (w/v) glucose
Nitrogen starvation medium (SD-N)	0.17 % (w/v) yeast nitrogen base without amino acids or ammonium sulfate 2 % (w/v) glucose

6.3 Cryogenic microscopy

6.3.1 Grid preparation

S. cerevisiae cells were treated with rapamycin or starvation media as described in section 6.2.2 and subsequently applied to Quantifoil (Großlöbichau, Germany) grids (Cu 200 mesh, R2/1, either Carbon or SiO_2 film). All cells used for tomography were treated with starvation media and in some cases carboxylate-modified microspheres (1 µm diameter crimson or 1 µm diameter blue, Invitrogen,Thermo Fisher Scientific, Waltham, MA, US) were added to the cell suspension prior to plunging. Cells were vitrified using a liquid ethane/propane mixture or liquid ethane at liquid nitrogen temperature and a Vitrobot Mark IV (Thermo Fisher Scientific, Waltham, MA, USA). Back-side blotting was done by covering the paddle of the device on the side of the grid film with a Teflon disc (Teflon disc was a generous donation from Dr. Julia Mahamid). The paddle at the back side of the grid was covered with filter paper (Whatman 597, Maidstone, UK) as customary. After some optimisation, 7 µl of cell suspension were applied to a grid and after one second wait time excess liquid was blotted away. The blot time would vary from 10 to 13 seconds. Blot force was kept consistently at -10, chamber humidity at 80% and chamber temperature at 30 °C.

After plunge-freezing the grids they were usually clipped into Autogrids (Thermo Fisher Scientifc, Waltham, MA, USA) for further electron microscopy applications or used unclipped for cryo-confocal microscopy.

6.3.2 Focussed ion beam milling

For this work the Aquilos 2 dual-beam FIB microscope (Thermo Fisher Scientific, Waltham, MA, USA) was used. Grids were kept at approximately -195 °C during the entire milling procedure. Milling procedures were carried out as for instance described in (Schaffer et al.,

2017) with some modifications. Lamella were milled using the gallium beam at 30 kV (0.5 nA to 30 pA) with a typical milling angle of 10 ° (i.e. stage angle of 17 °). After setting eucentric height at the sites of interest, the grids would be sputter-coated with platinum (30 mA, 0.1 mbar) for 15 seconds, then coated with an organometallic Platinum layer using the gas injection system (GIS) for 90 to 105 seconds. Subsequently, another sputter-coating layer was applied (30 mA, 0.1 mbar) for 15 seconds. Most of the milling sessions were carried out using the automated milling software AutoTEM (Thermo Fisher Sicentific, Waltham, MA, USA), often times followed by manual polishing. In both manual and automated milling situations the beam current would progressively be decreased from 0.1 nA to 10 pA, the closer one got to the region of interest i.e. the thinner the lamella became. Once the lamellae were at their final thickness, in some cases a final sputter coat would be applied (30 mA, 0.1 mbar) for three seconds as suggested in (Khavnekar et al., 2022).

TABLE 6.3: **Focussed ion beam currents used for thinning yeast cells.**

Manual milling		**Automated milling**	
Ion beam current	**Resulting thickness**	**Ion beam current**	**Resulting thickness**
0.5 nA	4-3 µm	0.5 nA	2.22 µm
0.3 nA	2 µm	0.3 nA	1.52 µm
0.1 nA	1 µm	0.1 nA	820 nm
50 pA	500 nm	50 pA	520 nm
30 pA	300-200 nm	30 pA	420-200 nm

6.3.3 Cryo-fluorescence microscopy

Fluorescent characterisation of the different yeast strains and tags were carried out using the LMS 800 (Zeiss, Oberkochen, Germany) confocal microscope equipped with an Airyscan detector and with a CMS196 cryostage (Linkam Scientific Instruments, Salfords, UK). Images were mostly collected as stacks with focal planes of 0.25 µm to 0.56 µm using 100x 0.75 NA (Zeiss EC Epiplan-Neofluar, WD 4 mm). Image stacks were processed with proprietary Zeiss software to reconstruct the tiled image from the Airyscan detector and carry out a deconvolution. Lamellae were imaged on above mentioned cryo-fluorescence microscope or the retro-fitted Meteor (Delmic BV, Delft, NL) bright-field cryo-fluorescence microscope with 50x 0.5 NA (Olympus LMPLFLN WD 10.6 mm) objective. Aside from one tomogram (Fig. 3.27F) all tomographic data was collected based on FM-TEM correlation from images collected on the Meteor.

6.3.4 Electron cryomicroscopy

After preparation and fluorescent imaging of the lamellae, grids containing the lamellae were transferred to the TEM microscope. To reduce ice contamination on lamellae, the storage time of the grids in the storage tank and the loading time was reduced to a minimum. Transmission electron microscopy was carried out on a Talos Arctica (200keV, Thermo Fisher Scientific, Waltham, MA, USA) microscope together with a K3 direct electron detector with Quantum GIF filter (Gatan Inc., Pleasanton, CA, USA) or Titan Krios (300 keV, Thermo Fisher Scientific, Waltham, MA, USA) equipped with a Falcon 4 direct electron detector (Thermo Fisher Scientific, Waltham, MA, USA). In both cases cameras were operated in movie mode with 10 to 15 frames per movie. For data collection and correlation of TEM overview images with Fluorescence data on the Talos Arctica, the software package SerialEM (Mastronarde, 2003) was used. For acquisition of lamella overview images and correlation with fluorescence data on the Titan Krios the proprietary software Maps

(Thermo Fisher Sicentific, Waltham, MA, USA) was utilised. For automated acquisition of tilt series on the Titan Krios the proprietary software Tomography (Thermo Fisher Scientific, Waltham, MA, USA) was used. Tilt series were acquired using the dose-symmetric acquisition scheme (Hagen et al., 2017) implemented in both SerialEM and Tomography over an angular range of -60° to +60° with a 2° increments. The set defocus was -5 µm and cumulative dose was kept below 130 e-/Å. The pixel size ranged from 1.74 to 2.78 Å depending on the camera and camera operation mode.

6.3.5 Data processing, segmentation and analysis

The tomographic data processing and analysis workflow is depicted in Figure 6.1. Tilt frames were preprocessed using WARP (Tegunov and Cramer, 2019). Patch-tracking guided tilt series alignment and tomogram reconstruction based on weighted back projection was done with IMOD (Mastronarde, 1997; Kremer et al., 1996) or AreTomo (Zheng et al., 2022). Denoising and missing wedge correction were carried out with the help of IsoNet (Liu et al., 2022). Segmentation was done with MemBrain v2 (Lamm et al., 2024) (an updated version from MemBrain (Lamm et al., 2022)) using its pretrained model (Version b from 10th Aug 2023) on the non-denoised data. Segmentations were subsequently manually corrected and completed using Dragonfly software, Version 2022.2 (Comet Technologies Canada Inc.). All evaluation of the presented tomograms was carried out in 2D.

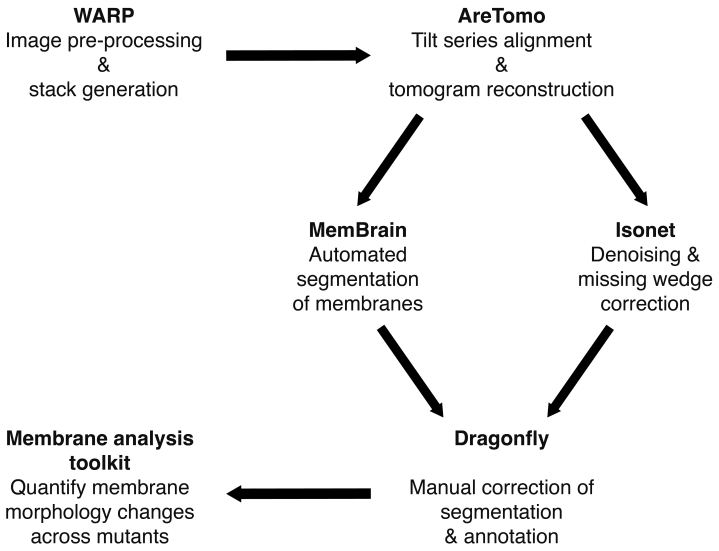

Figure 6.1: Schematic representation of the tomographical data processing workflow.

Evaluation of the segmented data was done with the help of Philipp Schönnenbeck and his Membrane analysis toolkit (unpublished). Segmentations of regions of interest were manually separated, saved to individual .tif files (see Fig. 3.32) and input into the toolkit. The running of the toolkit was carried out by Philipp Schönnenbeck. Prior to curvature measurements, a Gaussian filter (window size of 9 and sigma of 4) was applied in order to avoid curvature inaccuracies stemming from small errors in the segmentation. Subsequently a single pixel-wide skeleton of the membrane was generated. For each pixel of this skeleton the curvature was determined by selecting the neighbouring pixels in each direction along the skeleton up to 500 Å away from the pixel of interest. Next, a circle with the best possible fit through these pixels would be generated. The inverse of this circle's radius is defined as the curvature of the pixel of interest (illustrated in Fig. 6.2).

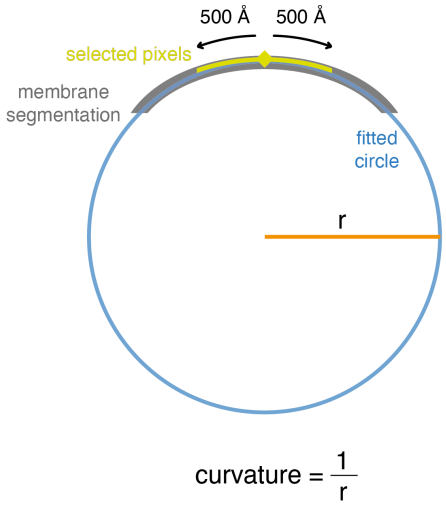

Figure 6.2: Illustration of the curvature estimation as implemented in Membrane analysis toolkit (unpublished. Philipp Schönnenbeck).

For distance measurements, the single pixel skeleton was also used. A support vector machine was used to determine a line separating the two sides of the segmented rims. The length of perpendicular lines (relative to the separation line) connecting individual pixels of each side of the rim were then determined and defined as the distance between the given two pixels. Circularity is defined here as $\frac{4\times\pi\times area}{circumference^2}$. Circularity of vesicles could only be determined for vesicles where the segmentation was complete and had no gaps, since the area was otherwise not correctly defined. Analysis and plotting on the data was carried out in Origin(Pro) 2023 (Version 10.0.0.154, OriginLab Corporation, Northampton, MA, USA).

Some of the structural biology software used in this work, such as IMOD, AreTomo, IsoNet, and PyMOL was compiled and configured by SBGrid (Morin et al., 2013).

6.3.6 Illustrations and Figures

Depictions of fluorescence data derived from the LSM800 cryo-confocal microscope were generated using FIJI (Schindelin et al., 2012). Fluorescence images from the Meteor bright-

field cryo-fluorescence microscope were generated using the proprietary software Odemis (Delmic BV, Delft, NL). Figures of tomograms were made using IMOD (Mastronarde, 1997; Kremer et al., 1996) and Dragonfly software, Version 2022.2 (Comet Technologies Canada Inc.). Depictions of atomic models of proteins were produced with the help of PyMOL Molecular Graphics System, version 2.5.5 (Schrödinger, LLC). EM map depictions were generated with Chimera (Pettersen et al., 2004). Illustrations and schematic representations were prepared with the vector graphics editor Adobe Illustrator (Adobe Inc.). This thesis was written using LaTeX.

7 Bibliography

Agard, D., Cheng, Y., Glaeser, R. M., and Subramaniam, S., 2014. Chapter Two - Single-Particle Cryo-Electron Microscopy (Cryo-EM): Progress, Challenges, and Perspectives for Further Improvement. In Hawkes, P. W., editor, *Advances in Imaging and Electron Physics*, volume 185, pages 113–137. Elsevier. ISBN: 978-0-12-800144-8.

Arnold, J., Mahamid, J., Lucic, V., de Marco, A., Fernandez, J.-J., Laugks, T., Mayer, T., Hyman, A. A., Baumeister, W., and Plitzko, J. M., *et al.*, 2016. Site-Specific Cryo-focused Ion Beam Sample Preparation Guided by 3D Correlative Microscopy. *Biophysical Journal*, **110**(4):860–869. doi: 10.1016/j.bpj.2015.10.053.

Backues, S. K., Orban, D. P., Bernard, A., Singh, K., Cao, Y., and Klionsky, D. J., 2015. Atg23 and Atg27 act at the early stages of Atg9 trafficking in S. cerevisiae. *Traffic (Copenhagen, Denmark)*, **16**(2):172–190. doi: 10.1111/tra.12240.

Baker, L. A. and Rubinstein, J. L., 2010. Chapter Fifteen - Radiation Damage in Electron Cryomicroscopy. In Jensen, G. J., editor, *Methods in Enzymology*, volume 481 of *Cryo-EM Part A Sample Preparation and Data Collection*, pages 371–388. Academic Press. ISBN: 978-0-12-374906-2.

Bas, L., Papinski, D., Licheva, M., Torggler, R., Rohringer, S., Schuschnig, M., and Kraft, C., 2018. Reconstitution reveals Ykt6 as the autophagosomal SNARE in autophagosome–vacuole fusion. *Journal of Cell Biology*, **217**(10):3656–3669. doi: 10.1083/jcb.201804028.

Baumann, V., Achleitner, S., Tulli, S., Schuschnig, M., Klune, L., and Martens, S., 2024. Faa1 membrane binding drives positive feedback in autophagosome biogenesis via fatty acid activation. *Journal of Cell Biology*, **223**(7):e202309057. doi: 10.1083/jcb.202309057.

Berkamp, S., Daviran, D., Smeets, M., Caignard, A., Jani, R., Sundermeyer, P., Jonker, C., Gerlach, S., Hoffmann, B., Lau, K., *et al.*, 2023. Correlative Light and Electron Cryo-Microscopy Workflow Combining Micropatterning, Ice Shield, and an In-Chamber Fluorescence Light Microscope. *BIO-PROTOCOL*, **13**(24). doi: 10.21769/BioProtoc.4901.

Bharat, T. A. M., Kureisaite-Ciziene, D., Hardy, G. G., Yu, E. W., Devant, J. M., Hagen, W. J. H., Brun, Y. V., Briggs, J. A. G., and Löwe, J., 2017. Structure of the hexagonal surface layer on Caulobacter crescentus cells. *Nature Microbiology*, **2**(7):17059. doi: 10.1038/nmicrobiol.2017.59.

Bieber, A., Capitanio, C., Erdmann, P. S., Fiedler, F., Beck, F., Lee, C.-W., Li, D., Hummer, G., Schulman, B. A., Baumeister, W., *et al.*, 2022. In situ structural analysis reveals membrane shape transitions during autophagosome formation. *Proceedings of the National Academy of Sciences*, **119**(39):e2209823119. doi: 10.1073/pnas.2209823119.

Bindels, D. S., Haarbosch, L., Van Weeren, L., Postma, M., Wiese, K. E., Mastop, M., Aumonier, S., Gotthard, G., Royant, A., Hink, M. A., *et al.*, 2017. mScarlet: A bright monomeric red fluorescent protein for cellular imaging. *Nature Methods*, **14**(1):53–56. doi: 10.1038/nmeth.4074.

Böhning, J. and Bharat, T. A., 2021. Towards high-throughput in situ structural biology using electron cryotomography. *Progress in Biophysics and Molecular Biology*, **160**:97–103. doi: 10.1016/j.pbiomolbio.2020.05.010.

Braschi, B., Bruford, E. A., Cavanagh, A. T., Neuman, S. D., and Bashirullah, A., 2022. The bridge-like lipid transfer protein (BLTP) gene group: Introducing new nomenclature based on structural homology indicating shared function. *Human Genomics*, **16**(1):66. doi: 10.1186/s40246-022-00439-3.

Brilot, A. F., Chen, J. Z., Cheng, A., Pan, J., Harrison, S. C., Potter, C. S., Carragher, B.,

Henderson, R., and Grigorieff, N., 2012. Beam-Induced Motion of Vitrified Specimen on Holey Carbon Film. *Journal of Structural Biology*, **177**(3):630–637. doi: 10.1016/j.jsb.2012.02.003.

Bursch, W., 2001. The autophagosomal–lysosomal compartment in programmed cell death. *Cell Death & Differentiation*, **8**(6):569–581. doi: 10.1038/sj.cdd.4400852.

Bykov, Y. S., Schaffer, M., Dodonova, S. O., Albert, S., Plitzko, J. M., Baumeister, W., Engel, B. D., and Briggs, J. A., 2017. The structure of the COPI coat determined within the cell. *eLife*, **6**:e32493. doi: 10.7554/eLife.32493.

Carter, S. D., Mageswaran, S. K., Farino, Z. J., Mamede, J. I., Oikonomou, C. M., Hope, T. J., Freyberg, Z., and Jensen, G. J., 2018. Distinguishing signal from autofluorescence in cryogenic correlated light and electron microscopy of mammalian cells. *Journal of Structural Biology*, **201**(1):15–25. doi: 10.1016/j.jsb.2017.10.009.

Chang, Y.-W., Chen, S., Tocheva, E. I., Treuner-Lange, A., Löbach, S., Søgaard-Andersen, L., and Jensen, G. J., 2014. Correlated cryogenic photoactivated localization microscopy and cryo-electron tomography. *Nature Methods*, **11**(7):737–739. doi: 10.1038/nmeth.2961.

Chen, Y., Zhou, F., Zou, S., Yu, S., Li, S., Li, D., Song, J., Li, H., He, Z., Hu, B., *et al.*, 2014. A Vps21 endocytic module regulates autophagy. *Molecular Biology of the Cell*, **25**(20):3166–3177. doi: 10.1091/mbc.E14-04-0917.

Cheng, J., Fujita, A., Yamamoto, H., Tatematsu, T., Kakuta, S., Obara, K., Ohsumi, Y., and Fujimoto, T., 2014. Yeast and mammalian autophagosomes exhibit distinct phosphatidylinositol 3-phosphate asymmetries. *Nature Communications*, **5**(1):3207. doi: 10.1038/ncomms4207.

Cheng, J., Li, B., Si, L., and Zhang, X., 2021. Determining structures in a native environment using single-particle cryoelectron microscopy images. *The Innovation*, **2**(4):100166. doi: 10.1016/j.xinn.2021.100166.

Cheng, Y., 2015. Single-Particle Cryo-EM at Crystallographic Resolution. *Cell*, **161**(3):450–457. doi: 10.1016/j.cell.2015.03.049.

Cheng, Y., Boll, W., Kirchhausen, T., Harrison, S. C., and Walz, T., 2007. Cryo-electron Tomography of Clathrin-coated Vesicles: Structural Implications for Coat Assembly. *Journal of Molecular Biology*, **365**(3):892–899. doi: 10.1016/j.jmb.2006.10.036.

Chowdhury, S., Otomo, C., Leitner, A., Ohashi, K., Aebersold, R., Lander, G. C., and Otomo, T., 2018. Insights into autophagosome biogenesis from structural and biochemical analyses of the ATG2A-WIPI4 complex. *Proceedings of the National Academy of Sciences*, **115**(42):E9792–E9801. doi: 10.1073/pnas.1811874115.

Cormack, B. P., Valdivia, R. H., and Falkow, S., 1996. FACS-optimized mutants of the green fluorescent protein (GFP). *Gene*, **173**(1):33–38. doi: 10.1016/0378-1119(95)00685-0.

Crowther, R. A., DeRosier, D. J., and Klug, A., 1970. The reconstruction of a three-dimensional structure from projections and its application to electron microscopy. *Proceedings of the Royal Society of London A*, **317**(1530):319–340. doi: 10.1098/rspa.1970.0119.

Dabrowski, R., Tulli, S., and Graef, M., 2023. Parallel phospholipid transfer by Vps13 and Atg2 determines autophagosome biogenesis dynamics. *Journal of Cell Biology*, **222**(7):e202211039. doi: 10.1083/jcb.202211039.

Dahlberg, P. D. and Moerner, W. E., 2021. Cryogenic Super-Resolution Fluorescence and Electron Microscopy Correlated at the Nanoscale. *Annual Review of Physical Chemistry*, **72**:253–278. doi: 10.1146/annurev-physchem-090319-051546.

Darsow, T., Rieder, S. E., and Emr, S. D., 1997. A Multispecificity Syntaxin Homologue, Vam3p, Essential for Autophagic and Biosynthetic Protein Transport to the Vacuole. *Journal of Cell Biology*, **138**(3):517–529. doi: 10.1083/jcb.138.3.517.

De, M., Oleskie, A. N., Ayyash, M., Dutta, S., Mancour, L., Abazeed, M. E., Brace, E. J., Skiniotis, G., and Fuller, R. S., 2017. The Vps13p–Cdc31p complex is directly required for TGN late endosome transport and TGN homotypic fusion. *Journal of Cell Biology*, **216**(2):425–439. doi: 10.1083/jcb.201606078.

Dickerson, J. L., Lu, P.-H., Hristov, D., Dunin-Borkowski, R. E., and Russo, C. J., 2022. Imaging biological macromolecules in thick specimens: The role of inelastic scattering in cryoEM. *Ultramicroscopy*, **237**:113510. doi: 10.1016/j.ultramic.2022.113510.

Dobro, M. J., Melanson, L. A., Jensen, G. J., and McDowall, A. W., 2010. Plunge Freezing for Electron Cryomicroscopy. In *Methods in Enzymology*, volume 481, pages 63–82. Elsevier. ISBN: 978-0-12-374906-2.

Downing, K. H. and Glaeser, R. M., 2008. Restoration of weak phase-contrast images recorded with a high degree of defocus: The "twin image" problem associated with CTF correction. *Ultramicroscopy*, **108**(9):921–928. doi: 10.1016/j.ultramic.2008.03.004.

Dubochet, J., Adrian, M., Chang, J.-J., Homo, J.-C., Lepault, J., McDowall, A. W., and Schultz, P., 1988. Cryo-electron microscopy of vitrified specimens. *Quarterly Reviews of Biophysics*, **21**(2):129–228. doi: 10.1017/S0033583500004297.

Dupont, N., Chauhan, S., Arko-Mensah, J., Castillo, E. F., Masedunskas, A., Weigert, R., Robenek, H., Proikas-Cezanne, T., and Deretic, V., 2014. Neutral Lipid Stores and Lipase PNPLA5 Contribute to Autophagosome Biogenesis. *Current Biology*, **24**(6):609–620. doi: 10.1016/j.cub.2014.02.008.

Dykstra, M. J., 1992. *Biological Electron Microscopy: Theory, Techniques, and Troubleshooting*. Springer US, Boston, MA. ISBN: 978-1-4684-0012-0 978-1-4684-0010-6.

Faro, A. R., Adam, V., Carpentier, P., Darnault, C., Bourgeois, D., and De Rosny, E., 2010. Low-temperature switching by photoinduced protonation in photochromic fluorescent proteins. *Photochemical & Photobiological Sciences*, **9**(2):254–262. doi: 10.1039/b9pp00121b.

Frangakis, A. S. and Hegerl, R., 2006. Segmentation of Three-dimensional Electron Tomographic Images. In Frank, J., editor, *Electron Tomography*, pages 353–370. Springer New York, New York, NY. ISBN: 978-0-387-31234-7 978-0-387-69008-7.

Frank, J., 1996. *Three-Dimensional Electron Microscopy of Macromolecular Assemblies*. Academic Press, San Diego. ISBN: 978-0-12-265040-6.

Fromm, S. A., Bharat, T. A., Jakobi, A. J., Hagen, W. J., and Sachse, C., 2015. Seeing tobacco mosaic virus through direct electron detectors. *Journal of Structural Biology*, **189**(2):87–97. doi: 10.1016/j.jsb.2014.12.002.

Fujioka, Y., Alam, J. M., Noshiro, D., Mouri, K., Ando, T., Okada, Y., May, A. I., Knorr, R. L., Suzuki, K., Ohsumi, Y., *et al.*, 2020. Phase separation organizes the site of autophagosome formation. *Nature*, **578**(7794):301–305. doi: 10.1038/s41586-020-1977-6.

Gao, J., Langemeyer, L., Kümmel, D., Reggiori, F., and Ungermann, C., 2018. Molecular mechanism to target the endosomal Mon1-Ccz1 GEF complex to the pre-autophagosomal structure. *eLife*, **7**:e31145. doi: 10.7554/eLife.31145.

Ghanbarpour, A., Valverde, D. P., Melia, T. J., and Reinisch, K. M., 2021. A model for a partnership of lipid transfer proteins and scramblases in membrane expansion and organelle biogenesis. *Proceedings of the National Academy of Sciences*, **118**(16). doi: 10.1073/pnas.2101562118.

Gibson, D. G., Young, L., Chuang, R.-Y., Venter, J. C., Iii, C. A. H., and Smith, H. O., 2009. Enzymatic assembly of DNA molecules up to several hundred kilobases. *Nature Methods*, **6**(5):343–345. doi: 10.1038/nmeth.1318.

Gietz, R. D., 2014. Yeast Transformation by the LiAc/SS Carrier DNA/PEG Method. In Smith, J. S. and Burke, D. J., editors, *Yeast Genetics*, volume 1205, pages 1–12. Springer New York, New York, NY. ISBN: 978-1-4939-1362-6 978-1-4939-1363-3.

Gómez-Sánchez, R., Rose, J., Guimarães, R., Mari, M., Papinski, D., Rieter, E., Geerts, W. J., Hardenberg, R., Kraft, C., Ungermann, C., *et al.*, 2018. Atg9 establishes Atg2-dependent contact sites between the endoplasmic reticulum and phagophores. *The Journal of Cell Biology*, **217**(8):2743–2763. doi: 10.1083/jcb.201710116.

Gong, F. C., Giddings, T. H., Meehl, J. B., Staehelin, L. A., and Galbraith, D. W., 1996. Z-membranes: Artificial organelles for overexpressing recombinant integral membrane proteins. *Proceedings of the National Academy of Sciences*, **93**(5):2219–2223. doi: 10.1073/pnas.93.5.2219.

González-Polo, R. A., Pizarro-Estrella, E., Yakhine-Diop, S. M. S., Rodríguez-Arribas, M., Gómez-Sánchez, R., Casado-Naranjo, I., Bravo-San Pedro, J. M., and Fuentes, J. M., 2016. The Basics of Autophagy. In Maiuri, M. C. and De Stefano, D., editors, *Autophagy Networks in Inflammation*, pages 3–20. Springer International Publishing, Cham. ISBN: 978-3-319-30079-5.

Graef, M., 2018. Lipid droplet-mediated lipid and protein homeostasis in budding yeast. *FEBS Letters*, **592**(8):1291–1303. doi: 10.1002/1873-3468.12996.

Graef, M., Friedman, J. R., Graham, C., Babu, M., and Nunnari, J., 2013. ER exit sites are physical and functional core autophagosome biogenesis components. *Molecular Biology of the Cell*, **24**(18):2918–2931. doi: 10.1091/mbc.e13-07-0381.

Grubb, D. T., 1974. Radiation damage and electron microscopy of organic polymers. *Journal of Materials Science*, **9**(10):1715–1736. doi: 10.1007/BF00540772.

Guardia, C. M., Tan, X.-F., Lian, T., Rana, M. S., Zhou, W., Christenson, E. T., Lowry, A. J., Faraldo-Gómez, J. D., Bonifacino, J. S., Jiang, J., *et al.*, 2020. Structure of Human ATG9A, the Only Transmembrane Protein of the Core Autophagy Machinery. *Cell Reports*, **31**(13):107837. doi: 10.1016/j.celrep.2020.107837.

Hagen, W. J. H., Wan, W., and Briggs, J. A. G., 2017. Implementation of a cryo-electron tomography tilt-scheme optimized for high resolution subtomogram averaging. *Journal of Structural Biology*, **197**(2):191–198. doi: 10.1016/j.jsb.2016.06.007.

He, C., Baba, M., Cao, Y., and Klionsky, D. J., 2008. Self-Interaction Is Critical for Atg9 Transport and Function at the Phagophore Assembly Site during Autophagy. *Molecular Biology of the Cell*, **19**(12):5506–5516. doi: 10.1091/mbc.e08-05-0544.

He, C., Song, H., Yorimitsu, T., Monastyrska, I., Yen, W.-L., Legakis, J. E., and Klionsky, D. J., 2006. Recruitment of Atg9 to the preautophagosomal structure by Atg11 is essential for selective autophagy in budding yeast. *The Journal of Cell Biology*, **175**(6):925–935. doi: 10.1083/jcb.200606084.

Henderson, R., 2015. Overview and future of single particle electron cryomicroscopy. *Archives of Biochemistry and Biophysics*, **581**:19–24. doi: 10.1016/j.abb.2015.02.036.

Hirata, E., Ohya, Y., and Suzuki, K., 2017. Atg4 plays an important role in efficient expansion of autophagic isolation membranes by cleaving lipidated Atg8 in Saccharomyces cerevisiae. *PLOS ONE*, **12**(7):e0181047. doi: 10.1371/journal.pone.0181047.

Hodgson, L., Nam, D., Mantell, J., Achim, A., and Verkade, P., 2014. Retracing in Correlative Light Electron Microscopy. In *Correlative Light and Electron Microscopy II*, volume 124 of *Methods in Cell Biology*, pages 1–21. Elsevier, 1 edition. ISBN: 978-0-12-801075-4.

Hollenstein, D. M., Gómez-Sánchez, R., Ciftci, A., Kriegenburg, F., Mari, M., Torggler, R., Licheva, M., Reggiori, F., and Kraft, C., 2019. Vac8 spatially confines autophagosome formation at the vacuole in S. cerevisiae. *Journal of Cell Science*, **132**(22):jcs235002. doi: 10.1242/jcs.235002.

Hollenstein, D. M. and Kraft, C., 2020. Autophagosomes are formed at a distinct cellular structure. *Current Opinion in Cell Biology*, **65**:50–57. doi: 10.1016/j.ceb.2020.02.012.

Imai, K., Hao, F., Fujita, N., Tsuji, Y., Oe, Y., Araki, Y., Hamasaki, M., Noda, T., and Yoshimori, T., 2016. Atg9A trafficking through the recycling endosomes is required for autophagosome formation. *Journal of Cell Science*, **129**(20):3781–3791. doi: 10.1242/jcs.196196.

Isensee, F., Jaeger, P. F., Kohl, S. A. A., Petersen, J., and Maier-Hein, K. H., 2021. nnU-Net: A self-configuring method for deep learning-based biomedical image segmentation. *Nature Methods*, **18**(2):203–211. doi: 10.1038/s41592-020-01008-z.

Kamada, Y., Funakoshi, T., Shintani, T., Nagano, K., Ohsumi, M., and Ohsumi, Y., 2000. Tor-Mediated Induction of Autophagy via an Apg1 Protein Kinase Complex. *Journal of Cell Biology*, **150**(6):1507–1513. doi: 10.1083/jcb.150.6.1507.

Kaufmann, R., Hagen, C., and Grünewald, K., 2014. Fluorescence cryo-microscopy: Current challenges and prospects. *Current Opinion in Chemical Biology*, **20**:86–91. doi: 10.1016/j.cbpa.2014.05.007.

Khavnekar, S., Vrbovská, V., Zaoralová, M., Kelley, R., Beck, F., Klumpe, S., Kotecha, A., Plitzko, J., and Erdmann, P. S., 2022. Optimizing Cryo-FIB Lamellas for sub-5Å in situ Structural Biology. *Preprint*, **BioRxiv**. doi: 10.1101/2022.06.16.496417.

Kirisako, T., Baba, M., Ishihara, N., Miyazawa, K., Ohsumi, M., Yoshimori, T., Noda, T., and Ohsumi, Y., 1999. Formation Process of Autophagosome Is Traced with Apg8/Aut7p in Yeast. *Journal of Cell Biology*, **147**(2):435–446. doi: 10.1083/jcb.147.2.435.

Klionsky, D. J., Cuervo, A. M., Dunn, Jr., W. A., Levine, B., van der Klei, I. J., and Seglen, P. O., 2007. How Shall I Eat Thee? *Autophagy*, **3**(5):413–416. doi: 10.4161/auto.4377.

Kobayashi, T., Suzuki, K., and Ohsumi, Y., 2012. Autophagosome formation can be achieved in the absence of Atg18 by expressing engineered PAS-targeted Atg2. *FEBS Letters*, **586**(16):2473–2478. doi: 10.1016/j.febslet.2012.06.008.

König, K., Uchugonova, A., and Breunig, H. G., 2014. High-resolution multiphoton cryomicroscopy. *Methods*, **66**(2):230–236. doi: 10.1016/j.ymeth.2013.07.006.

Koning, A. J., Roberts, C. J., and Wright, R. L., 1996. Different subcellular localization of Saccharomyces cerevisiae HMG-CoA reductase isozymes at elevated levels corresponds to distinct endoplasmic reticulum membrane proliferations. *Molecular Biology of the Cell*, **7**(5):769–789. doi: 10.1091/mbc.7.5.769.

Koning, R. I., Koster, A. J., and Sharp, T. H., 2018. Advances in cryo-electron tomography for biology and medicine. *Annals of Anatomy - Anatomischer Anzeiger*, **217**:82–96. doi: 10.1016/j.aanat.2018.02.004.

Kotani, T., Kirisako, H., Koizumi, M., Ohsumi, Y., and Nakatogawa, H., 2018. The Atg2-Atg18 complex tethers pre-autophagosomal membranes to the endoplasmic reticulum for autophagosome formation. *Proceedings of the National Academy of Sciences*, **115**(41):10363–10368. doi: 10.1073/pnas.1806727115.

Kremer, J. R., Mastronarde, D. N., and McIntosh, J., 1996. Computer Visualization of Three-Dimensional Image Data Using IMOD. *Journal of Structural Biology*, **116**(1):71–76. doi: 10.1006/jsbi.1996.0013.

Kriegenburg, F., Bas, L., Gao, J., Ungermann, C., and Kraft, C., 2019. The multi-functional SNARE protein Ykt6 in autophagosomal fusion processes. *Cell Cycle*, **18**(6-7):639–651. doi: 10.1080/15384101.2019.1580488.

Kudryashev, M., Castaño-Díez, D., and Stahlberg, H., 2012. LIMITING FACTORS IN SINGLE PARTICLE CRYO ELECTRON TOMOGRAPHY. *Computational and Structural Biotechnology Journal*, **1**(2):e201207002. doi: 10.5936/csbj.201207002.

Lai, L. T. F., Yu, C., Wong, J. S. K., Lo, H. S., Benlekbir, S., Jiang, L., and Lau, W. C. Y., 2019. Subnanometer resolution cryo-EM structure of Arabidopsis thaliana ATG9. *Autophagy*, :1–9. doi: 10.1080/15548627.2019.1639300.

Lambert, T. J., 2019. FPbase: A community-editable fluorescent protein database. *Nature Methods*, **16**(4):277–278. doi: 10.1038/s41592-019-0352-8.

Lamm, L., Righetto, R. D., Wietrzynski, W., Pöge, M., Martinez-Sanchez, A., Peng, T., and Engel, B. D., 2022. MemBrain: A deep learning-aided pipeline for detection of membrane proteins in Cryo-electron tomograms. *Computer Methods and Programs in Biomedicine*, **224**:106990. doi: 10.1016/j.cmpb.2022.106990.

Lamm, L., Zufferey, S., Righetto, R. D., Wietrzynski, W., Yamauchi, K. A., Burt, A., Liu, Y., Zhang, H., Martinez-Sanchez, A., Ziegler, S., *et al.*, 2024. MemBrain v2: An end-to-end tool for the analysis of membranes in cryo-electron tomography. *Preprint*, **BioRxiv**. doi: 10.1101/2024.01.05.574336.

Lang, T., Reiche, S., Straub, M., Bredschneider, M., and Thumm, M., 2000. Autophagy and the cvt Pathway Both Depend on *AUT9*. *Journal of Bacteriology*, **182**(8):2125–2133. doi: 10.1128/JB.182.8.2125-2133.2000.

Last, M. G. F., Tuijtel, M. W., Voortman, L. M., and Sharp, T. H., 2023. Selecting optimal support grids for super-resolution cryogenic correlated light and electron microscopy. *Scientific Reports*, **13**(1):8270. doi: 10.1038/s41598-023-35590-x.

Lazić, I., Wirix, M., Leidl, M. L., De Haas, F., Mann, D., Beckers, M., Pechnikova, E. V., Müller-Caspary, K., Egoavil, R., Bosch, E. G. T., *et al.*, 2022. Single-particle cryo-EM structures

from iDPC–STEM at near-atomic resolution. *Nature Methods*, **19**(9):1126–1136. doi: 10.1038/s41592-022-01586-0.

Levine, B. and Deretic, V., 2007. Unveiling the roles of autophagy in innate and adaptive immunity. *Nature Reviews. Immunology*, **7**(10):767–777. doi: 10.1038/nri2161.

Li, P., Lees, J. A., Lusk, C. P., and Reinisch, K. M., 2020a. Cryo-EM reconstruction of a VPS13 fragment reveals a long groove to channel lipids between membranes. *Journal of Cell Biology*, **219**(5):e202001161. doi: 10.1083/jcb.202001161.

Li, X., He, S., and Ma, B., 2020b. Autophagy and autophagy-related proteins in cancer. *Molecular Cancer*, **19**(1):12. doi: 10.1186/s12943-020-1138-4.

Li, Y. E., Wang, Y., Du, X., Zhang, T., Mak, H. Y., Hancock, S. E., McEwen, H., Pandzic, E., Whan, R. M., Aw, Y. C., *et al.*, 2021. TMEM41B and VMP1 are scramblases and regulate the distribution of cholesterol and phosphatidylserine. *Journal of Cell Biology*, **220**(6):e202103105. doi: 10.1083/jcb.202103105.

Liu, Y.-T., Zhang, H., Wang, H., Tao, C.-L., Bi, G.-Q., and Zhou, Z. H., 2022. Isotropic reconstruction for electron tomography with deep learning. *Nature Communications*, **13**(1):6482. doi: 10.1038/s41467-022-33957-8.

Lucas, B. A., Himes, B. A., Xue, L., Grant, T., Mahamid, J., and Grigorieff, N., 2021. Locating macromolecular assemblies in cells by 2D template matching with cisTEM. *eLife*, **10**:e68946. doi: 10.7554/eLife.68946.

Lučić, V., Rigort, A., and Baumeister, W., 2013. Cryo-electron tomography: The challenge of doing structural biology in situ. *The Journal of Cell Biology*, **202**(3):407–419. doi: 10.1083/jcb.201304193.

Maeda, S., Otomo, C., and Otomo, T., 2019. The autophagic membrane tether ATG2A transfers lipids between membranes. *eLife*, **8**:e45777. doi: 10.7554/eLife.45777.

Maeda, S., Yamamoto, H., Kinch, L. N., Garza, C. M., Takahashi, S., Otomo, C., Grishin, N. V., Forli, S., Mizushima, N., and Otomo, T., *et al.*, 2020. Structure, lipid scrambling activity and role in autophagosome formation of ATG9A. *Nature Structural & Molecular Biology*, :1–8. doi: 10.1038/s41594-020-00520-2.

Mahamid, J., Schampers, R., Persoon, H., Hyman, A. A., Baumeister, W., and Plitzko, J. M., 2015. A focused ion beam milling and lift-out approach for site-specific preparation of frozen-hydrated lamellas from multicellular organisms. *Journal of Structural Biology*, **192**(2):262–269. doi: 10.1016/j.jsb.2015.07.012.

Maki-Yonekura, S., Kawakami, K., Takaba, K., Hamaguchi, T., and Yonekura, K., 2023. Measurement of charges and chemical bonding in a cryo-EM structure. *Communications Chemistry*, **6**(1):98. doi: 10.1038/s42004-023-00900-x.

Mari, M., Griffith, J., Rieter, E., Krishnappa, L., Klionsky, D. J., and Reggiori, F., 2010. An Atg9-containing compartment that functions in the early steps of autophagosome biogenesis. *Journal of Cell Biology*, **190**(6):1005–1022. doi: 10.1083/jcb.200912089.

Maruyama, T., Alam, J. M., Fukuda, T., Kageyama, S., Kirisako, H., Ishii, Y., Shimada, I., Ohsumi, Y., Komatsu, M., Kanki, T., *et al.*, 2021. Membrane perturbation by lipidated Atg8 underlies autophagosome biogenesis. *Nature Structural & Molecular Biology*, **28**(7):583–593. doi: 10.1038/s41594-021-00614-5.

Massey, A. C., Zhang, C., and Cuervo, A. M., 2006. Chaperone-Mediated Autophagy in Aging and Disease. In *Current Topics in Developmental Biology*, volume 73, pages 205–235. Elsevier. ISBN: 978-0-12-153173-7.

Mastronarde, D. N., 1997. Dual-Axis Tomography: An Approach with Alignment Methods That Preserve Resolution. *Journal of Structural Biology*, **120**(3):343–352. doi: 10.1006/jsbi.1997.3919.

Mastronarde, D. N., 2003. SerialEM: A Program for Automated Tilt Series Acquisition on Tecnai Microscopes Using Prediction of Specimen Position. *Microscopy and Microanalysis*, **9**(S02):1182–1183. doi: 10.1017/S1431927603445911.

Matoba, K., Kotani, T., Tsutsumi, A., Tsuji, T., Mori, T., Noshiro, D., Sugita, Y., Nomura, N., Iwata, S., Ohsumi, Y., *et al.*, 2020. Atg9 is a lipid scramblase that mediates autophagosomal membrane expansion. *Nature Structural & Molecular Biology*, :1–9. doi: 10.1038/s41594-020-00518-w.

McDonald, K. L., Morphew, M., Verkade, P., and Müller-Reichert, T., 2007. Recent Advances in High-Pressure Freezing. In Walker, J. M. and Kuo, J., editors, *Electron Microscopy*, volume 369, pages 143–173. Humana Press, Totowa, NJ. ISBN: 978-1-58829-573-6 978-1-59745-294-6.

McMullan, G., Faruqi, A., Clare, D., and Henderson, R., 2014. Comparison of optimal performance at 300keV of three direct electron detectors for use in low dose electron microscopy. *Ultramicroscopy*, **147**:156–163. doi: 10.1016/j.ultramic.2014.08.002.

Melia, T. J., 2023. Growing thin — How bulk lipid transport drives expansion of the autophagosome membrane but not of its lumen. *Current Opinion in Cell Biology*, **83**:102190. doi: 10.1016/j.ceb.2023.102190.

Metskas, L. A. and Briggs, J. A. G., 2019. Fluorescence-Based Detection of Membrane Fusion State on a Cryo-EM Grid using Correlated Cryo-Fluorescence and Cryo-Electron Microscopy. *Microscopy and Microanalysis*, **25**(4):942–949. doi: 10.1017/S1431927619000606.

Mindell, J. A. and Grigorieff, N., 2003. Accurate determination of local defocus and specimen tilt in electron microscopy. *Journal of Structural Biology*, **142**(3):334–347. doi: 10.1016/S1047-8477(03)00069-8.

Mizushima, N., Noda, T., Yoshimori, T., Tanaka, Y., Ishii, T., George, M. D., Klionsky, D. J., Ohsumi, M., and Ohsumi, Y., 1998. A protein conjugation system essential for autophagy. *Nature*, **395**(6700):395–398. doi: 10.1038/26506.

Mizushima, N., Yoshimori, T., and Ohsumi, Y., 2011. The Role of Atg Proteins in Autophagosome Formation. *Annual Review of Cell and Developmental Biology*, **27**(1):107–132. doi: 10.1146/annurev-cellbio-092910-154005.

Moerner, W. E. and Orrit, M., 1999. Illuminating Single Molecules in Condensed Matter. *Science*, **283**(5408):1670–1676. doi: 10.1126/science.283.5408.1670.

Morin, A., Eisenbraun, B., Key, J., Sanschagrin, P. C., Timony, M. A., Ottaviano, M., and Sliz, P., 2013. Collaboration gets the most out of software. *eLife*, **2**:e01456. doi: 10.7554/eLife.01456.

Morita, K., Hama, Y., Izume, T., Tamura, N., Ueno, T., Yamashita, Y., Sakamaki, Y., Mimura, K., Morishita, H., Shihoya, W., *et al.*, 2018. Genome-wide CRISPR screen identifies *TMEM41B* as a gene required for autophagosome formation. *Journal of Cell Biology*, **217**(11):3817–3828. doi: 10.1083/jcb.201804132.

Naydenova, K., Kamegawa, A., Peet, M. J., Henderson, R., Fujiyoshi, Y., and Russo, C. J., 2022. On the reduction in the effects of radiation damage to two-dimensional crystals of organic and biological molecules at liquid-helium temperature. *Ultramicroscopy*, **237**:113512. doi: 10.1016/j.ultramic.2022.113512.

Neuman, S. D., Levine, T. P., and Bashirullah, A., 2022. A novel superfamily of

bridge-like lipid transfer proteins. *Trends in Cell Biology*, **32**(11):962–974. doi: 10.1016/j.tcb.2022.03.011.

Nickell, S., Förster, F., Linaroudis, A., Net, W. D., Beck, F., Hegerl, R., Baumeister, W., and Plitzko, J. M., 2005. TOM software toolbox: Acquisition and analysis for electron tomography. *Journal of Structural Biology*, **149**(3):227–234. doi: 10.1016/j.jsb.2004.10.006.

Noble, A. J. and Stagg, S. M., 2015. Automated batch fiducial-less tilt-series alignment in Appion using Protomo. *Journal of Structural Biology*, **192**(2):270–278. doi: 10.1016/j.jsb.2015.10.003.

Noda, N. N., 2023. Structural view on autophagosome formation. *FEBS Letters*, :1873–3468.14742. doi: 10.1002/1873-3468.14742.

Noda, T., Kim, J., Huang, W.-P., Baba, M., Tokunaga, C., Ohsumi, Y., and Klionsky, D. J., 2000. Apg9p/Cvt7p Is an Integral Membrane Protein Required for Transport Vesicle Formation in the Cvt and Autophagy Pathways. *Journal of Cell Biology*, **148**(3):465–480. doi: 10.1083/jcb.148.3.465.

Nogales, E. and Scheres, S. H., 2015. Cryo-EM: A Unique Tool for the Visualization of Macromolecular Complexity. *Molecular Cell*, **58**(4):677–689. doi: 10.1016/j.molcel.2015.02.019.

Obara, K., Sekito, T., Niimi, K., and Ohsumi, Y., 2008. The Atg18-Atg2 Complex Is Recruited to Autophagic Membranes via Phosphatidylinositol 3-Phosphate and Exerts an Essential Function. *Journal of Biological Chemistry*, **283**(35):23972–23980. doi: 10.1074/jbc.M803180200.

Ohsumi, Y., 2014. Historical landmarks of autophagy research. *Cell Research*, **24**(1):9–23. doi: 10.1038/cr.2013.169.

Omrane, M., Ben M'Barek, K., Santinho, A., Nguyen, N., Nag, S., Melia, T. J., and Thiam, A. R., 2023. LC3B is lipidated to large lipid droplets during prolonged starvation for noncanonical autophagy. *Developmental Cell*, **58**(14):1266–1281.e7. doi: 10.1016/j.devcel.2023.05.009.

Ormö, M., Cubitt, A. B., Kallio, K., Gross, L. A., Tsien, R. Y., and Remington, S. J., 1996. Crystal Structure of the Aequorea victoria Green Fluorescent Protein. *Science*, **273**(5280):1392–1395. doi: 10.1126/science.273.5280.1392.

Osawa, T., Ishii, Y., and Noda, N. N., 2020. Human ATG2B possesses a lipid transfer activity which is accelerated by negatively charged lipids and WIPI4. *Genes to Cells*, **25**(1):65–70. doi: 10.1111/gtc.12733.

Osawa, T., Kotani, T., Kawaoka, T., Hirata, E., Suzuki, K., Nakatogawa, H., Ohsumi, Y., and Noda, N. N., 2019. Atg2 mediates direct lipid transfer between membranes for autophagosome formation. *Nature Structural & Molecular Biology*, **26**(4):281–288. doi: 10.1038/s41594-019-0203-4.

Osawa, T., Matoba, K., and Noda, N. N., 2022. Lipid Transport from Endoplasmic Reticulum to Autophagic Membranes. *Cold Spring Harbor Perspectives in Biology*, . doi: 10.1101/cshperspect.a041254.

Papinski, D., Schuschnig, M., Reiter, W., Wilhelm, L., Barnes, C. A., Maiolica, A., Hansmann, I., Pfaffenwimmer, T., Kijanska, M., Stoffel, I., *et al.*, 2014. Early Steps in Autophagy Depend on Direct Phosphorylation of Atg9 by the Atg1 Kinase. *Molecular Cell*, **53**(3):471–483. doi: 10.1016/j.molcel.2013.12.011.

Peck, A., Carter, S. D., Mai, H., Chen, S., Burt, A., and Jensen, G. J., 2022. Montage electron tomography of vitrified specimens. *Journal of Structural Biology*, **214**(2):107860. doi: 10.1016/j.jsb.2022.107860.

Pettersen, E. F., Goddard, T. D., Huang, C. C., Couch, G. S., Greenblatt, D. M., Meng, E. C., and Ferrin, T. E., 2004. UCSF Chimera–a visualization system for exploratory research and analysis. *Journal of Computational Chemistry*, **25**(13):1605–1612. doi: 10.1002/jcc.20084.

Pfisterer, S. G., Bakula, D., Frickey, T., Cezanne, A., Brigger, D., Tschan, M. P., Robenek, H., and Proikas-Cezanne, T., 2014. Lipid droplet and early autophagosomal membrane targeting of Atg2A and Atg14L in human tumor cells. *Journal of Lipid Research*, **55**(7):1267–1278. doi: 10.1194/jlr.M046359.

Pletnev, S., Shcherbakova, D. M., Subach, O. M., Pletneva, N. V., Malashkevich, V. N., Almo, S. C., Dauter, Z., and Verkhusha, V. V., 2014. Orange Fluorescent Proteins: Structural Studies of LSSmOrange, PSmOrange and PSmOrange2. *PLoS ONE*, **9**(6):e99136. doi: 10.1371/journal.pone.0099136.

Pyle, E. and Zanetti, G., 2021. Current data processing strategies for cryo-electron tomography and subtomogram averaging. *Biochemical Journal*, **478**(10):1827–1845. doi: 10.1042/BCJ20200715.

Radermacher, M., 1988. Three-Dimensional reconstruction of single particles from random and nonrandom tilt series. *Journal of Electron Microscopy Technique*, **9**(4):359–394. doi: 10.1002/jemt.1060090405.

Radermacher, M., 1992. Weighted Back-Projection Methods. In Frank, J., editor, *Electron Tomography*, pages 91–115. Springer US, Boston, MA. ISBN: 978-1-4757-2165-2 978-1-4757-2163-8.

Raimondi, V. and Grinzato, A., 2021. A basic introduction to single particles cryo-electron microscopy. *AIMS Biophysics*, **9**(1):5–20. doi: 10.3934/biophy.2022002.

Reggiori, F. and Klionsky, D. J., 2006. Atg9 sorting from mitochondria is impaired in early secretion and VFT-complex mutants in Saccharomyces cerevisiae. *Journal of Cell Science*, **119**(14):2903–2911. doi: 10.1242/jcs.03047.

Reggiori, F., Shintani, T., Chong, H., Nair, U., and Klionsky, D. J., 2005. Atg9 Cycles Between Mitochondria and the Pre-Autophagosomal Structure in Yeasts. *Autophagy*, **1**(2):101–109. doi: 10.4161/auto.1.2.1840.

Reggiori, F., Tucker, K. A., Stromhaug, P. E., and Klionsky, D. J., 2004. The Atg1-Atg13 Complex Regulates Atg9 and Atg23 Retrieval Transport from the Pre-Autophagosomal Structure. *Developmental Cell*, **6**(1):79–90. doi: 10.1016/S1534-5807(03)00402-7.

Reimer, L. and Hawkes, P. W., 2013. *Transmission Electron Microscopy: Physics of Image Formation and Microanalysis*. Springer, Berlin, Heidelberg, 2nd ed edition. ISBN: 978-3-662-21579-1.

Rez, P., Larsen, T., and Elbaum, M., 2016. Exploring the theoretical basis and limitations of cryo-STEM tomography for thick biological specimens. *Journal of Structural Biology*, **196**(3):466–478. doi: 10.1016/j.jsb.2016.09.014.

Rieter, E., Vinke, F., Bakula, D., Cebollero, E., Ungermann, C., Proikas-Cezanne, T., and Reggiori, F., 2013. Atg18 function in autophagy is regulated by specific sites within its -propeller. *Journal of Cell Science*, **126**(2):593–604. doi: 10.1242/jcs.115725.

Rigort, A. and Plitzko, J. M., 2015. Cryo-focused-ion-beam applications in structural biology. *Archives of Biochemistry and Biophysics*, **581**:122–130. doi: 10.1016/j.abb.2015.02.009.

Sambrook, J. and Russell, D. W., 2001. *Molecular Cloning: A Laboratory Manual*. Cold Spring Harbor Laboratory Press, Cold Spring Harbor, N.Y, 3rd ed edition. ISBN: 978-0-87969-577-4 978-0-87969-576-7.

Sartori, A., Gatz, R., Beck, F., Rigort, A., Baumeister, W., and Plitzko, J. M., 2007. Correlative microscopy: Bridging the gap between fluorescence light microscopy and cryo-electron tomography. *Journal of Structural Biology*, **160**(2):135–145. doi: 10.1016/j.jsb.2007.07.011.

Sato, T. K., Rehling, P., Peterson, M. R., and Emr, S. D., 2000. Class C Vps Protein Complex Regulates Vacuolar SNARE Pairing and Is Required for Vesicle Docking/Fusion. *Molecular Cell*, **6**(3):661–671. doi: 10.1016/S1097-2765(00)00064-2.

Sawa-Makarska, J., Baumann, V., Coudevylle, N., von Bülow, S., Nogellova, V., Abert, C., Schuschnig, M., Graef, M., Hummer, G., and Martens, S., *et al.*, 2020. Reconstitution of autophagosome nucleation defines Atg9 vesicles as seeds for membrane formation. *Science*, **369**(6508). doi: 10.1126/science.aaz7714.

Schäfer, J. A., Schessner, J. P., Bircham, P. W., Tsuji, T., Funaya, C., Pajonk, O., Schaeff, K., Ruffini, G., Papagiannidis, D., Knop, M., *et al.*, 2020. ESCRT machinery mediates selective microautophagy of endoplasmic reticulum in yeast. *The EMBO Journal*, **39**(2):e102586. doi: 10.15252/embj.2019102586.

Schaffer, M., Mahamid, J., Engel, B. D., Laugks, T., Baumeister, W., and Plitzko, J. M., 2017. Optimized cryo-focused ion beam sample preparation aimed at in situ structural studies of membrane proteins. *Journal of Structural Biology*, **197**(2):73–82. doi: 10.1016/j.jsb.2016.07.010.

Schepers, J. and Behl, C., 2021. Lipid droplets and autophagy—links and regulations from yeast to humans. *Journal of Cellular Biochemistry*, **122**(6):602–611. doi: 10.1002/jcb.29889.

Schindelin, J., Arganda-Carreras, I., Frise, E., Kaynig, V., Longair, M., Pietzsch, T., Preibisch,

S., Rueden, C., Saalfeld, S., Schmid, B., *et al.*, 2012. Fiji: An open-source platform for biological-image analysis. *Nature Methods*, **9**(7):676–682. doi: 10.1038/nmeth.2019.

Schiøtz, O. H., Kaiser, C. J. O., Klumpe, S., Morado, D. R., Poege, M., Schneider, J., Beck, F., Klebl, D. P., Thompson, C., and Plitzko, J. M., *et al.*, 2023. Serial Lift-Out: Sampling the molecular anatomy of whole organisms. *Nature Methods*, . doi: 10.1038/s41592-023-02113-5.

Schorb, M. and Briggs, J. A. G., 2014. Correlated cryo-fluorescence and cryo-electron microscopy with high spatial precision and improved sensitivity. *Ultramicroscopy*, **143**:24–32. doi: 10.1016/j.ultramic.2013.10.015.

Schuck, S., Gallagher, C. M., and Walter, P., 2014. ER-phagy mediates selective degradation of endoplasmic reticulum independently of the core autophagy machinery. *Journal of Cell Science*, :jcs.154716. doi: 10.1242/jcs.154716.

Schütter, M., Giavalisco, P., Brodesser, S., and Graef, M., 2020. Local Fatty Acid Channeling into Phospholipid Synthesis Drives Phagophore Expansion during Autophagy. *Cell*, **180**(1):135–149.e14. doi: 10.1016/j.cell.2019.12.005.

Schwartz, C. L., Sarbash, V. I., Ataullakhanov, F. I., Mcintosh, J. R., and Nicastro, D., 2007. Cryo-fluorescence microscopy facilitates correlations between light and cryo-electron microscopy and reduces the rate of photobleaching. *Journal of Microscopy*, **227**(2):98–109. doi: 10.1111/j.1365-2818.2007.01794.x.

Sekito, T., Kawamata, T., Ichikawa, R., Suzuki, K., and Ohsumi, Y., 2009. Atg17 recruits Atg9 to organize the pre-autophagosomal structure. *Genes to Cells*, **14**(5):525–538. doi: 10.1111/j.1365-2443.2009.01299.x.

Shaner, N. C., Lambert, G. G., Chammas, A., Ni, Y., Cranfill, P. J., Baird, M. A., Sell, B. R., Allen, J. R., Day, R. N., Israelsson, M., *et al.*, 2013. A bright monomeric green fluorescent

protein derived from Branchiostoma lanceolatum. *Nature Methods*, **10**(5):407–409. doi: 10.1038/nmeth.2413.

Shatz, O., Fraiberg, M., Isola, D., Das, S., Gogoi, O., Polyansky, A., Shimoni, E., Dadosh, T., Dezorella, N., Wolf, S. G., *et al.*, 2024. Rim aperture of yeast autophagic membranes balances cargo inclusion with vesicle maturation. *Developmental Cell*, :S153458072400073X. doi: 10.1016/j.devcel.2024.02.002.

Shibutani, S. T. and Yoshimori, T., 2014. A current perspective of autophagosome biogenesis. *Cell Research*, **24**(1):58–68. doi: 10.1038/cr.2013.159.

Shima, T., Kirisako, H., and Nakatogawa, H., 2019. COPII vesicles contribute to autophagosomal membranes. *Journal of Cell Biology*, **218**(5):1503–1510. doi: 10.1083/jcb.201809032.

Shpilka, T., Welter, E., Borovsky, N., Amar, N., Mari, M., Reggiori, F., and Elazar, Z., 2015. Lipid droplets and their component triglycerides and steryl esters regulate autophagosome biogenesis. *The EMBO Journal*, **34**(16):2117–2131. doi: 10.15252/embj.201490315.

Sigworth, F. J., 2016. Principles of cryo-EM single-particle image processing. *Microscopy*, **65**(1):57–67. doi: 10.1093/jmicro/dfv370.

Singh, S. S., Vats, S., Chia, A. Y.-Q., Tan, T. Z., Deng, S., Ong, M. S., Arfuso, F., Yap, C. T., Goh, B. C., Sethi, G., *et al.*, 2018. Dual role of autophagy in hallmarks of cancer. *Oncogene*, **37**(9):1142–1158. doi: 10.1038/s41388-017-0046-6.

Stark, H., Zemlin, F., and Boettcher, C., 1996. Electron radiation damage to protein crystals of bacteriorhodopsin at different temperatures. *Ultramicroscopy*, **63**(2):75–79. doi: 10.1016/0304-3991(96)00045-9.

Subach, O. M., Cranfill, P. J., Davidson, M. W., and Verkhusha, V. V., 2011a. An Enhanced Monomeric Blue Fluorescent Protein with the High Chemical Stability of the Chromophore. *PLoS ONE*, **6**(12):e28674. doi: 10.1371/journal.pone.0028674.

Subach, O. M., Patterson, G. H., Ting, L.-M., Wang, Y., Condeelis, J. S., and Verkhusha, V. V., 2011b. A photoswitchable orange-to-far-red fluorescent protein, PSmOrange. *Nature Methods*, **8**(9):771–777. doi: 10.1038/nmeth.1664.

Suzuki, K., Akioka, M., Kondo-Kakuta, C., Yamamoto, H., and Ohsumi, Y., 2013. Fine mapping of autophagy-related proteins during autophagosome formation in Saccharomyces cerevisiae. *Journal of Cell Science*, **126**(11):2534–2544. doi: 10.1242/jcs.122960.

Suzuki, K., Kirisako, T., Kamada, Y., Mizushima, N., Noda, T., and Ohsumi, Y., 2001. The pre-autophagosomal structure organized by concerted functions of APG genes is essential for autophagosome formation. *The EMBO Journal*, **20**(21):5971–5981. doi: 10.1093/emboj/20.21.5971.

Suzuki, K., Kubota, Y., Sekito, T., and Ohsumi, Y., 2007. Hierarchy of Atg proteins in pre-autophagosomal structure organization. *Genes to Cells*, **12**(2):209–218. doi: 10.1111/j.1365-2443.2007.01050.x.

Suzuki, K. and Ohsumi, Y., 2010. Current knowledge of the pre-autophagosomal structure (PAS). *FEBS Letters*, **584**(7):1280–1286. doi: 10.1016/j.febslet.2010.02.001.

Suzuki, S. W., Yamamoto, H., Oikawa, Y., Kondo-Kakuta, C., Kimura, Y., Hirano, H., and Ohsumi, Y., 2015. Atg13 HORMA domain recruits Atg9 vesicles during autophagosome formation. *Proceedings of the National Academy of Sciences*, **112**(11):3350–3355. doi: 10.1073/pnas.1421092112.

Takeshige, K., Baba, M., Tsuboi, S., Noda, T., and Ohsumi, Y., 1992. Autophagy in yeast

demonstrated with proteinase-deficient mutants and conditions for its induction. *Journal of Cell Biology*, **119**(2):301–311. doi: 10.1083/jcb.119.2.301.

Tegunov, D. and Cramer, P., 2019. Real-time cryo-electron microscopy data preprocessing with Warp. *Nature Methods*, **16**(11):1146–1152. doi: 10.1038/s41592-019-0580-y.

The wwPDB Consortium, Turner, J., Abbott, S., Fonseca, N., Pye, R., Carrijo, L., Duraisamy, A. K., Salih, O., Wang, Z., Kleywegt, G. J., *et al.*, 2024. EMDB—the Electron Microscopy Data Bank. *Nucleic Acids Research*, **52**(D1):D456–D465. doi: 10.1093/nar/gkad1019.

Tooze, S. A. and Dikic, I., 2016. Autophagy Captures the Nobel Prize. *Cell*, **167**(6):1433–1435. doi: 10.1016/j.cell.2016.11.023.

Torggler, R., Papinski, D., and Kraft, C., 2017. Assays to Monitor Autophagy in Saccharomyces cerevisiae. *Cells*, **6**(3):23. doi: 10.3390/cells6030023.

Toulmay, A., Whittle, F. B., Yang, J., Bai, X., Diarra, J., Banerjee, S., Levine, T. P., Golden, A., and Prinz, W. A., 2022. Vps13-like proteins provide phosphatidylethanolamine for GPI anchor synthesis in the ER. *Journal of Cell Biology*, **221**(3):e202111095. doi: 10.1083/jcb.202111095.

Tsukada, M. and Ohsumi, Y., 1993. Isolation and characterization of autophagy-defective mutants of Saccharomyces cerevisiae. *FEBS Letters*, **333**(1-2):169–174. doi: 10.1016/0014-5793(93)80398-E.

Tuijtel, M. W., Mulder, A. A., Posthuma, C. C., van der Hoeven, B., Koster, A. J., Bárcena, M., Faas, F. G. A., and Sharp, T. H., 2017. Inducing fluorescence of uranyl acetate as a dual-purpose contrast agent for correlative light-electron microscopy with nanometre precision. *Scientific Reports*, **7**(1):10442. doi: 10.1038/s41598-017-10905-x.

Turk, M. and Baumeister, W., 2020. The promise and the challenges of cryo-electron tomography. *FEBS Letters*, **594**(20):3243–3261. doi: 10.1002/1873-3468.13948.

Ungermann, C. and Reggiori, F., 2018. Atg9 proteins, not so different after all. *Autophagy*, **14**(8):1456–1459. doi: 10.1080/15548627.2018.1477382.

Valverde, D. P., Yu, S., Boggavarapu, V., Kumar, N., Lees, J. A., Walz, T., Reinisch, K. M., and Melia, T. J., 2019. ATG2 transports lipids to promote autophagosome biogenesis. *Journal of Cell Biology*, **218**(6):1787–1798. doi: 10.1083/jcb.201811139.

Van Driel, L. F., Valentijn, J. A., Valentijn, K. M., Koning, R. I., and Koster, A. J., 2009. Tools for correlative cryo-fluorescence microscopy and cryo-electron tomography applied to whole mitochondria in human endothelial cells. *European Journal of Cell Biology*, **88**(11):669–684. doi: 10.1016/j.ejcb.2009.07.002.

van Vliet, A. R., Chiduza, G. N., Maslen, S. L., Pye, V. E., Joshi, D., De Tito, S., Jefferies, H. B., Christodoulou, E., Roustan, C., Punch, E., *et al.*, 2022. ATG9A and ATG2A form a heteromeric complex essential for autophagosome formation. *Molecular Cell*, **82**(22):S1097276522010176. doi: 10.1016/j.molcel.2022.10.017.

Van Vliet, A. R., Jefferies, H. B. J., Faull, P. A., Chadwick, J., Ibrahim, F., Skehel, M. J., and Tooze, S. A., 2024. Exploring the ATG9A interactome uncovers interaction with VPS13A. *Journal of Cell Science*, **137**(4):jcs.261081. doi: 10.1242/jcs.261081.

Velázquez, A. P., Tatsuta, T., Ghillebert, R., Drescher, I., and Graef, M., 2016. Lipid droplet–mediated ER homeostasis regulates autophagy and cell survival during starvation. *Journal of Cell Biology*, **212**(6):621–631. doi: 10.1083/jcb.201508102.

Velikkakath, A. K. G., Nishimura, T., Oita, E., Ishihara, N., and Mizushima, N., 2012. Mammalian Atg2 proteins are essential for autophagosome formation and important for reg-

ulation of size and distribution of lipid droplets. *Molecular Biology of the Cell*, **23**(5):896–909. doi: 10.1091/mbc.e11-09-0785.

Wagner, F. R., Watanabe, R., Schampers, R., Singh, D., Persoon, H., Schaffer, M., Fruhstorfer, P., Plitzko, J., and Villa, E., 2020. Preparing samples from whole cells using focused-ion-beam milling for cryo-electron tomography. *Nature Protocols*, **15**(6):2041–2070. doi: 10.1038/s41596-020-0320-x.

Wan, W. and Briggs, J., 2016. Cryo-Electron Tomography and Subtomogram Averaging. In *Methods in Enzymology*, volume 579, pages 329–367. Elsevier. ISBN: 978-0-12-805382-9.

Wang, Y., Dahmane, S., Ti, R., Mai, X., Zhu, L., Carlson, L.-A., and Stjepanovic, G., 2023. Structural basis for lipid transfer by the ATG2A-ATG9A complex. *Preprint*, **BioRxiv**. doi: 10.1101/2023.07.08.548186.

Webber, J. L. and Tooze, S. A., 2010. New insights into the function of Atg9. *FEBS Letters*, **584**(7):1319–1326. doi: 10.1016/j.febslet.2010.01.020.

Weisenburger, S., Jing, B., Hänni, D., Reymond, L., Schuler, B., Renn, A., and Sandoghdar, V., 2014. Cryogenic Colocalization Microscopy for Nanometer-Distance Measurements. *ChemPhysChem*, **15**(4):763–770. doi: 10.1002/cphc.201301080.

Wen, X. and Klionsky, D. J., 2016. An overview of macroautophagy in yeast. *Journal of Molecular Biology*, **428**(9):1681–1699. doi: 10.1016/j.jmb.2016.02.021.

Wolf, S. G., Houben, L., and Elbaum, M., 2014. Cryo-scanning transmission electron tomography of vitrified cells. *Nature Methods*, **11**(4):423–428. doi: 10.1038/nmeth.2842.

Wright, R., Basson, M., D'Ari, L., and Rine, J., 1988. Increased amounts of HMG-CoA

reductase induce "karmellae": A proliferation of stacked membrane pairs surrounding the yeast nucleus. *Journal of Cell Biology*, **107**(1):101–114. doi: 10.1083/jcb.107.1.101.

Xie, Z. and Klionsky, D. J., 2007. Autophagosome formation: Core machinery and adaptations. *Nature Cell Biology*, **9**(10):1102–1109. doi: 10.1038/ncb1007-1102.

Yamamoto, H., Kakuta, S., Watanabe, T. M., Kitamura, A., Sekito, T., Kondo-Kakuta, C., Ichikawa, R., Kinjo, M., and Ohsumi, Y., 2012. Atg9 vesicles are an important membrane source during early steps of autophagosome formation. *Journal of Cell Biology*, **198**(2):219–233. doi: 10.1083/jcb.201202061.

Yamasaki, A., Alam, J. M., Noshiro, D., Hirata, E., Fujioka, Y., Suzuki, K., Ohsumi, Y., and Noda, N. N., 2020. Liquidity Is a Critical Determinant for Selective Autophagy of Protein Condensates. *Molecular Cell*, **77**(6):1163–1175.e9. doi: 10.1016/j.molcel.2019.12.026.

Yang, J. E., Larson, M. R., Sibert, B. S., Kim, J. Y., Parrell, D., Sanchez, J. C., Pappas, V., Kumar, A., Cai, K., Thompson, K., *et al.*, 2023. Correlative montage parallel array cryotomography for in situ structural cell biology. *Nature Methods*, **20**(10):1537–1543. doi: 10.1038/s41592-023-01999-5.

Yang, J. E., Larson, M. R., Sibert, B. S., Shrum, S., and Wright, E. R., 2021. CorRelator: Interactive software for real-time high precision cryo-correlative light and electron microscopy. *Journal of Structural Biology*, **213**(2):107709. doi: 10.1016/j.jsb.2021.107709.

Yen, W.-L., Legakis, J. E., Nair, U., and Klionsky, D. J., 2007. Atg27 Is Required for Autophagy-dependent Cycling of Atg9. *Molecular Biology of the Cell*, **18**(2):581–593. doi: 10.1091/mbc.e06-07-0612.

Yip, K. M., Fischer, N., Paknia, E., Chari, A., and Stark, H., 2020. Atomic-resolution

protein structure determination by cryo-EM. *Nature*, **587**(7832):157–161. doi: 10.1038/s41586-020-2833-4.

You, X., Zhang, X., Cheng, J., Xiao, Y., Ma, J., Sun, S., Zhang, X., Wang, H.-W., and Sui, S.-F., 2023. In situ structure of the red algal phycobilisome–PSII–PSI–LHC megacomplex. *Nature*, **616**(7955):199–206. doi: 10.1038/s41586-023-05831-0.

Young, A. R. J., Chan, E. Y. W., Hu, X. W., Köchl, R., Crawshaw, S. G., High, S., Hailey, D. W., Lippincott-Schwartz, J., and Tooze, S. A., 2006. Starvation and ULK1-dependent cycling of mammalian Atg9 between the TGN and endosomes. *Journal of Cell Science*, **119**(18):3888–3900. doi: 10.1242/jcs.03172.

Zanetti, G., Prinz, S., Daum, S., Meister, A., Schekman, R., Bacia, K., and Briggs, J. A., 2013. The structure of the COPII transport-vesicle coat assembled on membranes. *eLife*, **2**:e00951. doi: 10.7554/eLife.00951.

Zheng, J.-X., Li, Y., Ding, Y.-H., Liu, J.-J., Zhang, M.-J., Dong, M.-Q., Wang, H.-W., and Yu, L., 2017. Architecture of the ATG2B-WDR45 complex and an aromatic Y/HF motif crucial for complex formation. *Autophagy*, **13**(11):1870–1883. doi: 10.1080/15548627.2017.1359381.

Zheng, S., Wolff, G., Greenan, G., Chen, Z., Faas, F. G., Bárcena, M., Koster, A. J., Cheng, Y., and Agard, D. A., 2022. AreTomo: An integrated software package for automated marker-free, motion-corrected cryo-electron tomographic alignment and reconstruction. *Journal of Structural Biology: X*, **6**:100068. doi: 10.1016/j.yjsbx.2022.100068.

Zhou, F., Wu, Z., Zhao, M., Murtazina, R., Cai, J., Zhang, A., Li, R., Sun, D., Li, W., Zhao, L., *et al.*, 2019. Rab5-dependent autophagosome closure by ESCRT. *Journal of Cell Biology*, **218**(6):1908–1927. doi: 10.1083/jcb.201811173.

Zhou, F., Zou, S., Chen, Y., Lipatova, Z., Sun, D., Zhu, X., Li, R., Wu, Z., You, W., Cong, X., *et al.*, 2017. A Rab5 GTPase module is important for autophagosome closure. *PLoS genetics*, **13**(9):e1007020. doi: 10.1371/journal.pgen.1007020.

Zhu, Y., Sun, D., Schertel, A., Ning, J., Fu, X., Gwo, P. P., Watson, A. M., Zanetti-Domingues, L. C., Martin-Fernandez, M. L., Freyberg, Z., *et al.*, 2021. Serial cryoFIB/SEM Reveals Cytoarchitectural Disruptions in Leigh Syndrome Patient Cells. *Structure*, **29**(1):82–87.e3. doi: 10.1016/j.str.2020.10.003.

A Appendix

TABLE A.1: ***S. cerevisiae* strains used in this work.**

Name	Genotype	Source
yCK566	BY474x hi3Δ1 leu2Δ0 met15Δ ura3Δ0	C. Kraft
yCK414	BY474x hi3Δ1 leu2Δ0 met15Δ ura3Δ0 atg9::Kan	C. Kraft
yTB87	BY474x hi3Δ1 leu2Δ0 met15Δ ura3Δ0 ATG9-3xmGFP:NAT	C. Kraft
ySB4	BY474x hi3Δ1 leu2Δ0 met15Δ ura3Δ0 ATG9-3xmGFP:NAT atg1::NAT	C. Kraft
yDP707	BY474x hi3Δ1 leu2Δ0 met15Δ ura3Δ0 ATG9-3xEGFP:NAT vam3::KAN	C. Kraft
yCK811	BY474x hi3Δ1 leu2Δ0 met15Δ ura3Δ0 ypt7::KAN	C. Kraft
yML17	BY474x hi3Δ1 leu2Δ0 met15Δ ura3Δ0 vps21::KAN	C. Kraft
yCK761	BY474x hi3Δ1 leu2Δ0 met15Δ ura3Δ0 atg2::NAT	C. Kraft
yDP13	BY474x hi3Δ1 leu2Δ0 met15Δ ura3Δ0 atg9::NAT atg2::KAN	C. Kraft
yML61	BY474x hi3Δ1 leu2Δ0 met15Δ ura3Δ0 ATG9-3xmEGFP:NAT ypt7::KAN	C. Kraft
yML63	BY474x hi3Δ1 leu2Δ0 met15Δ ura3Δ0 ATG9-3xmEGFP:NAT vps21::KAN	C. Kraft
yML65	BY474x hi3Δ1 leu2Δ0 met15Δ ura3Δ0 ATG9-3xmEGFP:NAT snf7::KAN	C. Kraft
yML123	BY474x hi3Δ1 leu2Δ0 met15Δ ura3Δ0 atg9::KAN atg2::NAT snf7::KAN	C. Kraft

TABLE A.2: **Plasmids used in this work.**

Plasmid	Features	Backbone	Promotor	Organism of interest	Source
pCK785	scAtg9-3xGFP	pRS415	scAtg9	*S. cerevisiae*	C. Kraft
pDP70	scAtg2-3xmCherry	pRS315	scAtg2	*S. cerevisiae*	C. Kraft
pCO101	scAtg9-Neon	pRS415	scAtg9	*S. cerevisiae*	This work
pCO110	scAtg9-3xPSmOrange	pRS415	scAtg9	*S. cerevisiae*	This work
pCO111	scAtg9-3xmScarlet	pRS415	scAtg9	*S. cerevisiae*	This work
pCO112	scAtg9-3xmTagBFP2	pRS415	scAtg9	*S. cerevisiae*	This work
pCO113	scAtg2-3xPSmOrange	pRS315	scAtg2	*S. cerevisiae*	This work
pCO114	scAtg2-3xmScarlet	pRS315	scAtg2	*S. cerevisiae*	This work
pCO118	scAtg9-3xmTagBFP2, URA3 resistance	pRS415	scAtg9	*S. cerevisiae*	This work
pCO119	scAtg2PM4-3xmScarlet	pRS315	scAtg2	*S. cerevisiae*	This work
pCO120	scAtg9basic-3xmTagBFP2, URA3 resistance	pRS415	scAtg9	*S. cerevisiae*	This work

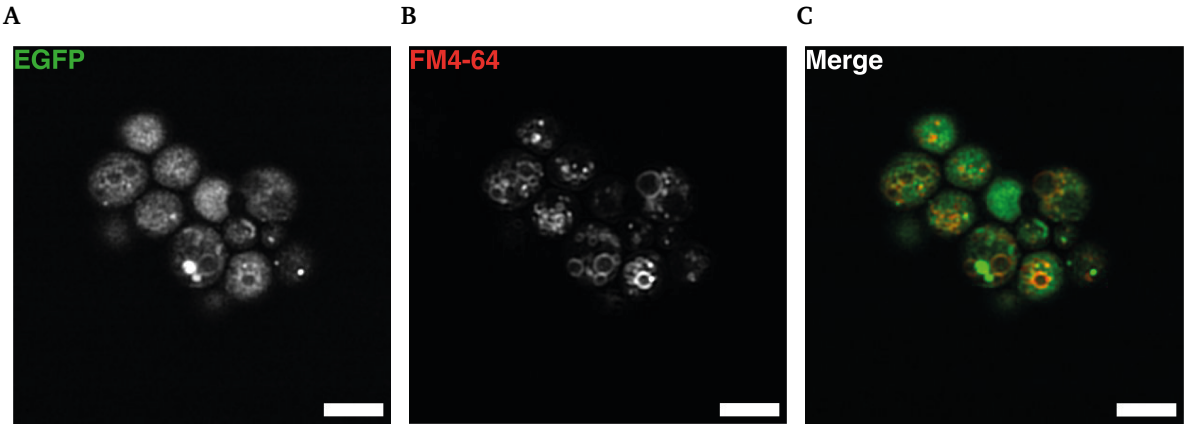

Figure A.1: Confocal microscopy images of yML17 transformed with pCK785 (Atg9-3xEGFP on plasmid Δvps21) in **A**) the EGFP channel, **B**) the FM4-64 channel, and **C**) a merge of the two channels, EGFP in green and FM4-64 in red. All images originate from a slice of a z-stack (focal depth 220 nm). Scale bars 5 μm.

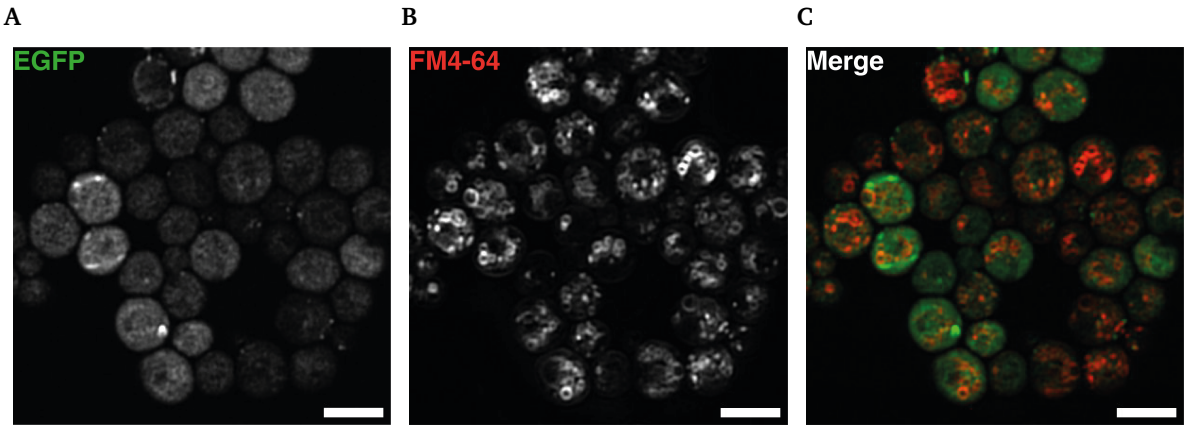

Figure A.2: Confocal microscopy images of yCK811 pCK785 (Atg9-3xEGFP on plasmid in Δypt7) in **A**) the EGFP channel, **B**) the FM4-64 channel, and **C**) a merge of the two channels, EGFP in green and FM4-64 in red. All images originate from a slice of a z-stack (focal depth 220 nm). Scale bars 5 μm.

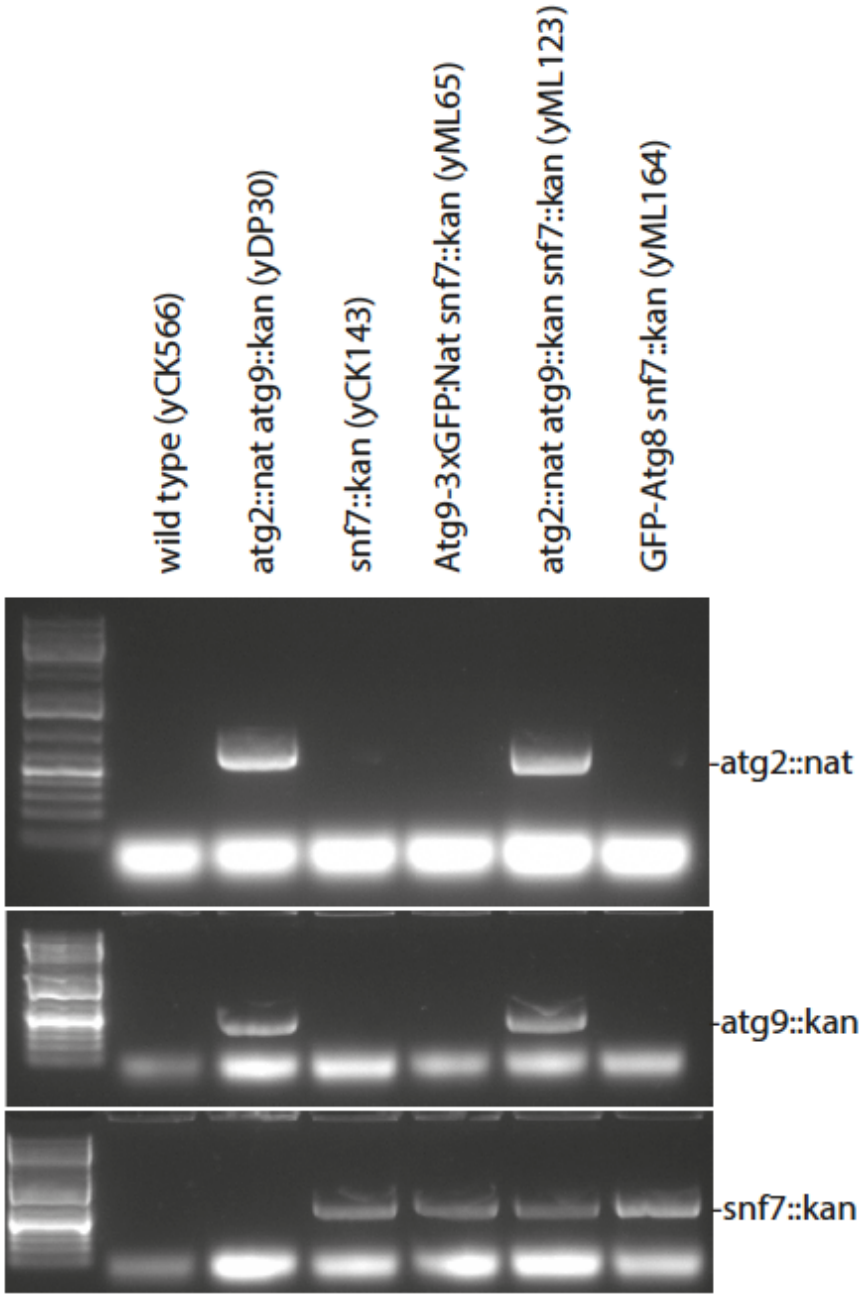

Figure A.3: Verification of the genotype of *S. cerevisiae* strains used for tomography. Strains were tested with colony PCR using a forward primer binding in the specific promoter region of the gene of interest and the reverse primer binding in the resistance cassette. This experiment was carried out by Mariya Licheva (Kraft group, University of Freiburg, Germany). WT, yDP13 and yCK143 were used as controls.